# Advanced Acoustic Emission (AE) Monitoring Techniques for Aerospace Structures

PhD Thesis

September 2015

John McCrory (MEng)

Cardiff School of Engineering
Cardiff University
Cardiff
UK

**Summary:**

This thesis contains the development of advanced Acoustic Emission (AE) monitoring techniques for aerospace structures. The techniques developed in this work explore AE's ability to detect, locate and characterise signals. Experimental studies were conducted on a range of structures made from typical aerospace materials, including carbon fibre composite, GLARE and high grade steel; and the data collected from these studies was processed using the newly developed AE techniques, in order to determine their effectiveness. The work was divided into three main areas of research:

**1. AE Source Location**

A location test was conducted on a GLARE fuselage panel specimen with complex geometric features in order to test the effect that altering the training grid resolution has on the accuracy of the *delta-T mapping* location technique. *Delta-T mapping* yielded more accurate results than the conventional *Time of Arrival* (TOA) method and the development of this technique formed the basis from which AE signals could be confidently located.

**2. Damage Identification**

A fatigue test was conducted on a pre-notched, 300M grade steel, cantilevered beam which was monitored using both AE and *Digital Image Correlation* (DIC) during loading. The work considered the detection and tracking of fatigue crack growth. A novel form of data acquisition and analysis called an *Additive Hits Analysis* (AHA) was proposed and developed. The AHA provided a similar result to a conventional wavestreaming approach which was also used, though it did so in a much more streamlined manner. Specific *delta-T mapping* located signals were used to determine the frequency bands of interest for the cracking process to be tracked. DIC was noted as being a useful tool for validation of AE testing.

**3. Characterisation on Large Scale Specimen**

A buckling test was conducted on a large-scale carbon fibre composite specimen which was monitored using AE and DIC. The work focused on the detection, location and characterisation of signals occurring in the specimen due to the applied loading. An ultrasonic C-scanner was used to quantify the damage which occurred in the specimen and this was found to be a useful tool for validation. A novel form of the modal analysis technique *Measured Amplitude Ratio* (MAR) called *Automated Corrected MAR* was developed. The new method was found to be able to successfully distinguish between in and out-of-plane signals arising in the specimen during the test whilst also providing time saving benefits over conventional methods. The combination of *delta-T mapping* with the *Automated Corrected MAR* results proved useful to the analysis.

Key words: Structural Health Monitoring, Acoustic Emission, damage detection, source characterisation, GLARE, carbon fibre, composite materials

## Acknowledgments

First and foremost I would like to thank Dr Rhys Pullin and Professor Karen Holford for their guidance and continued encouragement throughout this project. They have the ability to inject energy and enthusiasm into their work, and it has been a pleasure to research under their supervision.

I must also thank my colleagues Dr Matthew Pearson, Dr Mark Eaton and Dr Hayley Wyatt for their advice and assistance during this project, and also for making day-to-day office life more entertaining.

I am grateful to Ian King and the rest of the technical staff for their assistance running the testing equipment, and also to the friendly and helpful administration staff up in the Research Office.

I would like to thank all of my friends in Team DH for boardgames, cheese and wine; all my training partners at Nam Pai Chaun for holding the pads; and finally my family for supporting me every step of the way. You're all the best.

Finally, I would like to thank the Engineering & Physical Sciences Research Council (EPSRC) and Cardiff University School of Engineering for the sponsorship which allowed me to conduct this research, and embark on this rather life changing journey.

Table of Contents

# Glossary

The following terms relate to acoustic emission (AE), many of which can be found in ASTM E610 (ASTM 1982) and ASTM E1316 (ASTM 1991);

**Acoustic emission (AE):** the class of phenomena whereby transient elastic waves are generated by the rapid release of energy from localized sources within a material, or the transient waves so generated. Acoustic emission is the recommended term for general use. Other terms that have been used in AE literature include: (1) stress wave emission; (2) microseismic activity; and (3) emission or acoustic emission with other qualifying modifiers.

**Hit:** A hit is the term used to indicate that a given AE channel has detected and processed an acoustic emission transient.

**Event:** An event is the group of AE hits that were received from a single source.

**Source:** A mechanical mechanism that produces AE signals.

**Acoustic emission signal:** The electrical signal obtained through the detection of acoustic emission.

**Transducer:** Device that converts the physical parameters of the wave into an electrical signal.

**Couplant:** Substance providing an acoustic coupling between the propagation medium and the transducer.

**Threshold:** A preset voltage level, which has to be exceeded before an AE signal is recorded, and processed. The following terms are made with reference to the threshold (Figure i).

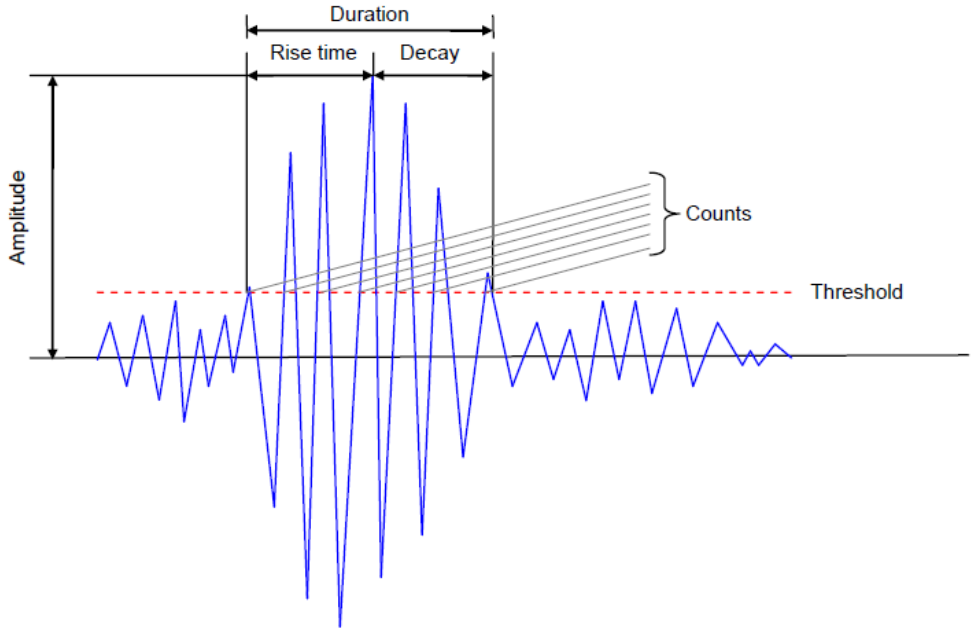


Figure i: AE Waveform Features, figure reproduced from Pearson (2013)

**AE Features:** This refers to the features of an AE waveform such as amplitude, duration, rise time, decay and counts, Figure i, which are frequently used during the analysis of AE data.

**Duration:** The interval between the first and last time the threshold was exceeded by the signal (Figure i).

**Peak Amplitude:** Maximum signal amplitude within the duration of the signal (Figure i).

**Counts:** Number of times the signal amplitude exceeds the threshold (Figure i).

**Rise Time:** The interval between the first threshold crossing and the maximum amplitude of the signal (Figure i).

**Initiation Frequency:** The average frequency of the waveform from the initial threshold crossing to the peak of the AE waveform.

**Energy (Absolute):** The integral of the squared voltage signal divided by the reference resistance (10kΩ) over the duration of the AE waveform packet.

**Dispersion:** The phenomenon whereby wave velocity varies with frequency.

**Group wave velocity:** The perceived velocity at which a packet of energy (or wave packet) travels.

**Phase wave velocity:** Velocity of individual waves within a packet of energy (or wave packet), each wave may travel at a different velocity (see dispersion). Phase velocity does not have to equal group velocity.

**Attenuation:** The rate at which signal amplitude reduces with distance of propagation.

**$S_0$ mode:** Symmetrical fundamental Lamb wave mode that propagates in plate like materials. (Also known as the extensional mode).

**$A_0$ mode:** Asymmetric fundamental Lamb wave mode that propagates in plate like materials. (Also known as the flexural mode).

**Hsu-Nielson (H-N) Source:** An artificial source of AE generated by breaking a mechanical pencil lead on the surface of a structure.

**Time of Arrival (TOA):** This is the conventional AE source location algorithm used to locate AE sources in a structure. It uses the difference in arrival times between transducers and a defined wave velocity to estimate the location of an AE event.

**Delta-T mapping:** An advanced AE location technique which was developed in Cardiff University (Baxter 2007). The technique owes its name to the fact that it involves creating maps of the difference in time of arrival between each pair of sensors (Δt maps), for an AE source originating from any position in the inspected area. These maps are created by generating an artificial AE source at numerous positions within the inspected area and measuring the times of arrival of the signals generated by those artificial sources at each sensor. The difference in the times of arrival between each pair of sensors, of hits recorded from real AE events can be compared to the Δt maps in order for the location of the AE event to be calculated; full description given in Section 2.2.5.3.

**AIC delta-T mapping:** This is an advanced AE location technique which improves on the delta-t mapping approach developed by Baxter (2007), by using the Akiakie Information Criteria (AIC) (Maeda 1985) to determine more accurate first arrival times of recorded AE waves.

**Wavestream:** Raw AE activity recorded for a set time period irrespective of the threshold used.

**Wavelet Transform:** Signal processing technique which decomposes a transient signal in order to release a time-frequency representation of a wave.

**Acousto-ultrasonics:** An active monitoring technique which utilises guided Lamb waves (GLW) to detect damage in a structure. An actuation signal is used to generate GLW in a structure by using surface mounted or embedded piezoelectric transducers. The resulting waves are recorded at receivers, where changes in the signal are observed due to scattering and mode conversion due to the presence of damage in the structure.

**Cross Correlation:** A signal processing technique which can be utilised in AU and AE applications to determine whether damage is present in a structure. It uses the integral of the product of two signals to determine the similarity of the shape of two signals with respect to each other.

**Ultrasonic C-scanner:** An ultrasonic technique which is used to detect, measure and characterise a range of manufacturing and in-service defects in composites materials. The term ‘C-scan’ refers to the manner in which the ultrasonic scanning probe is passed back-and-forth over the surface of the specimen under investigation.

**Digital Image Correlation:** An optical technique that allows for the full field measurement of contour deformation, vibration and strain by tracking the movement of a black and white speckle pattern applied to the specimen.

**Piezoelectric effect:** This refers to the ability of certain crystals to become polarised when they are subjected to a mechanical strain which results in the creation of an electric

potential. The magnitude of the polarisation and resulting electrical potential is proportional to the mechanical strain.

**Coupling factor:** A measure of the effectiveness with which mechanical energy is converted to electrical energy, and vice versa, between the contact of a piezoelectric element and a solid surface.

**Polarisation:** The process of making a ceramic piezoelectric in a given direction by applying a strong electric field at a temperature slightly below the Curie point.

**Smart structure:** A structure which has sensing devices embedded within the structure which are used for SHM techniques.

**Impedance (acoustic):** a mathematical quantity used in computation of reflection characteristics at boundaries; product of wave velocity and material density.

**Lamb wave:** a specific mode of propagation in which the two parallel boundary surfaces of the material under examination (such as a plate or the wall of a tube) establish the mode of propagation. The Lamb wave can be generated only at particular values of frequency, angle of incidence, and material thickness. The velocity of the wave is dependent on the mode of propagation and the product of the material thickness and the examination frequency.

**Mode:** the type of ultrasonic wave propagating in a material as characterized by the particle motion (for example, longitudinal, transverse, etc.).

**Mode conversion:** phenomenon by which an ultrasonic wave that is propagating in one mode can form ultrasonic wave(s) of other modes; typically due to the interaction of the original wave with an interface.

**Noise:** any undesired signal (electrical or acoustic) that tends to interfere with the reception, interpretation, or processing of the desired signal.

# Nomenclature

### Fracture Mechanics

| | | |
|---|---|---|
| $K$ | stress intensity factor | $Pa.m^{-1/2}$ |
| $Y$ | flaw shape factor | |
| σ | stress | Pa |
| $a$ | half of the crack length | m |
| $\Delta K$ | stress intensity range | $Pa.m^{-1/2}$ |
| $da$ | change in half crack length | m |
| $dN$ | number of cycles which caused the change in half crack length | |
| $C$ | material constant for Paris Law | |
| $m$ | material constant for Paris Law | |

### Time of Arrival Location

| | | |
|---|---|---|
| $t_i$ | time of arrival of wave at recording sensor i | s |
| Δt | difference in time of arrival | s |
| $d_i$ | distance from sensor i to source | m |
| $D_1$ | distance of sensor 2 to sensor 1 | m |
| $D_2$ | distance of sensor 3 to sensor 1 | m |
| $c$ | wave speed | m/s |

### Propagation Path Determination

| | | |
|---|---|---|
| d | propagation distance | m |
| θ | propagation angle | Deg |
| $A_o velocity$ | velocity of $A_o$ lamb wave mode | m/s |
| $S_o velocity$ | velocity of $S_o$ lamb wave mode | m/s |

### Dispersion

| | | |
|---|---|---|
| C | velocity of wave | m/s |
| $C_p$ | phase velocity | m/s |
| $f$ | frequency | Hz |
| $\lambda$ | wavelength | m |

# 1 Introduction

## 1.1 Novelty Statement

This study investigated a number of advanced acoustic emission (AE) techniques that could be applied in the field of structural health monitoring (SHM), with a particular emphasis on the use of these techniques on aerospace materials such as carbon fibre reinforced plastic (CFRP), glass laminate aluminium reinforced epoxy (GLARE) and high strength steel. The research contained in this thesis incorporates studies into the ability of AE to detect, locate and characterise damage arising in aerospace structures and contributes the novelty outlined below;

- A comprehensive study on the optimisation of *delta-T mapping*, an advanced location AE location technique, in a complex GLARE structure was undertaken.

- A novel form of damage progression monitoring was developed called an *Additive Hits Analysis* (AHA). The technique, which draws on the benefits of conventional AE wavestreaming approaches but improves upon a number of drawbacks associated with the technique, was tested in a fatigue test on a high strength steel bar.

- A novel means of performing the modal AE characterisation technique, *Measured Amplitude Ratio* (MAR) was developed. The improved technique, *Automated Corrected MAR*, was implemented in a buckling test on a carbon fibre composite panel and proved to be capable of distinguishing between in and out-of-plane signals arising during the test.

The work contained in this thesis has formed the basis of two journal papers and contributed to four conference papers;

J. McCrory, S. Kh. Al-Jumaili, D. Crivelli, M. R. Pearson, M. J. Eaton, C. A. Featherston, M. Guagliano, K. M. Holford and R Pullin. (2015) ‘Damage classification in carbon fibre

composites using acoustic emission: A comparison of three techniques'. Journal of Composites: Part B. Vol 68, pp 424–430.

S. Kh. Al-Jumaili, K. M. Holford, M. J. Eaton, J. McCrory, M. R. Pearson and R Pullin. (2014) 'Classification of acoustic emission data from buckling test of carbon fibre panel using unsupervised clustering techniques'. Structural Health Monitoring Vol 14 (3), pp. 241-251.

J. McCrory, S. Kh. Al-Jumaili, M. R. Pearson, M. J. Eaton, K. M. Holford and R Pullin. (2014) 'Automated Corrected MAR Calculation for Characterisation of AE Signals'. 31st European Conference on Acoustic Emission Testing, Dresden, Germany, 09/2014.

S. Kh. Al-Jumaili, M. J. Eaton, K. M. Holford, J. McCrory and R Pullin. (2014) 'Damage characterisation in composite materials under buckling test using acoustic emission waveform clustering technique', 53rd Annual Conference of The British Institute of Non-Destructive Testing, Manchester, UK; 09/2014.

D. Crivelli, M Guagliano, J. McCrory, S. Kh. Al-Jumaili, M. J. Eaton, M. R. Pearson, K. M. Holford and R Pullin. (2013) 'Classification of Acoustic Emission Data from Buckling Test of Carbon Fiber Panel using Neural Networks', 3rd European Aeronautics Science Network Workshop on Aerostructures, Politechnico di Milano; 10/2013.

J. McCrory, R. Pullin, M. R. Pearson, M. J. Eaton, C. A. Featherston and K. M. Holford. (2012) 'Effect of Delta-T Grid Resolution on Acoustic Emission Source Location in GLARE', 30th European Conference on Acoustic Emission Testing & 7th International Conference on Acoustic Emission, University of Granada, Spain; 09/2012.

Furthermore, during the period of study in which this PhD was conducted, the author applied a number of the techniques contained within this thesis to additional projects and consequentially contributed to one additional journal paper and one additional conference paper which are not directly derived from the experimental chapters detailed in this thesis;

E. Z. Loizidou, N. A. Williams, D. A. Barrow, M. J. Eaton, J. McCrory, S. L. Evans and C. J. Allender. 'Structural characterisation and transdermal delivery studies on sugar microneedles: Experimental and finite element modelling analyses'. European Journal of Pharmaceutics and Biopharmaceutics. Vol 89, pp 224-231.

J. P. McCrory, D. Crivelli, M. J. Eaton, K. M. Holford, M. R. Pearson and R. Pullin. 'Damage Characterisation using Artificial-Wavestream Acoustic Emission Data'. 9th International Conference on Advances in Experimental Mechanics, Cardiff University; 09/2013.

## 1.2 Background

It is well reported that greenhouse gas (GHG) emissions are continuing to rise to never before seen levels, to the point where the scale of their impact on the climate is becoming increasingly difficult to predict (IPCC 2014). Recent estimates from the Intergovernmental Panel on Climate Change (IPCC) state that there is a high risk of irreversible global climate changes occurring unless additional measures are adopted (IPCC 2015), and in light of this potential tipping point there is a need for action in every contributing area, no matter how small. Realistically though, and as is often seen to be the case, it is the economic consequences rather than any genuine concerns for the environment that are proving to be the most effective incentives for a global response to this challenge. As a result of numerous studies predicting that the cost of immediate mitigation would be monumentally lower that the cost of damage repairs and action to combat climate change in the future (The U.S. Council of Economic Advisers 2014; IPCC 2007), the subject of mitigating climate change has been pushed near the top of many agendas.

Aviation is responsible for 2% of global $CO_2$ emissions (ICAO 2013; ICAO 2010) and hence, since the Kyoto Protocol meeting in 1998 countries have been working under the guidance of the International Civil Aviation Organisation (ICAO) to reduce GHG emissions from aircraft. Despite predicting air traffic demands to grow at a rate of 4.9% per annum, recent ICAO documentation has called on the aviation sector to improve its fuel efficiency by 2% per annum until 2020 and thereafter maintain net $CO_2$ emission levels (ICAO 2013). The largest airline trade association in the world, the International Air Transport Association (IATA), and its members have gone one step further than this by pledging to reduce $CO_2$ emissions to 50% of 2005 levels by the year 2050 (IATA 2015) and thus the aviation sector appears to be embracing the climate change battle head on.

Current strategies suggested to achieve these new targets recognise that such ambitious reductions in emissions cannot come from one source of change alone and so

incorporate a range of measures. The IATA are promoting a four pillar approach which includes; improving airframe and engine technology (including the introduction of sustainable biofuels), improving flight operation efficiency, improving airspace and airport infrastructure and introducing positive economic instruments (IATA 2013b). It should also be highlighted that environmental concerns are not the only drivers for change in the aviation sector and that even before the increasingly stringent regulations surrounding GHG emissions were introduced, aircraft manufacturers were improving aircraft technologies in a bid to increase aircraft fuel efficiency and gain a commercial advantage. In fact, the commercial incentive for airlines to invest in fuel efficient aircraft has never been higher with the cost of jet fuel reaching 33% of total operating costs in 2013 (IATA 2013a; Cranfield University Air Transport Department 2010).

One means by which aircraft manufacturers have been improving aircraft frames to consume less fuel is via the introduction of lighter structural materials. Taking centre stage in this evolution of aircraft frame technology are composite materials. Offering significant weight savings and fatigue and corrosion resistance when compared with conventionally used aluminium, composites have seen a dramatic increase in use on civil aircraft in the last decade (AeroStrategy 2007). However, it is imperative that any changes introduced in the pursuit to reduce weight do not compromise the structural integrity of the aircraft, since any failures could produce disastrous consequences. In fact, aircraft safety is of such paramount importance that aircraft structures are periodically subject to non-destructive testing (NDT) in order to ensure that they still comply with airworthiness regulations (Schmidt et al. 1998). These periodic NDT inspections provide continued confidence in the aircraft's structural integrity and form the basis of current structural health monitoring (SHM) protocol for aircraft. Since all aircraft structures must be subjected to NDT in this fashion, methods of reliably inspecting the new composite material structures have been developed. Composites provide additional challenges for NDT due to their complex, multi-layered composition. They can be subject to numerous damage mechanisms, many of which occur sub-surface which means they

are more difficult to effectively visibly inspect and also renders some traditional NDT techniques such as liquid dye penetrant testing unusable. Of all the conventional NDT methods available, ultrasonic and audible sonic testing have proved to be the most effective for monitoring composites since they utilise vibrational waves which travel through the entire thickness of the component so that even sub-surface defects can be detected (Federal Aviation Administration 2012). However, these NDT techniques are most suitable for small inspection areas and the quality of the results are subject to operator skill (Kapadia 2007) and so new and improved methods are still required.

Despite its merits, periodically performing NDT on aircraft also has a number of negative consequences. Inspections can be time consuming since many components need to be removed from the aircraft in order for testing to take place, and refitted thereafter. Since the aircraft cannot be used during these times, NDT inspection periods equate to down-time for the aircraft and hence a source of lost revenue for the airline. Furthermore, NDT is particularly difficult for structures with complex geometry or areas that are difficult to reach by hand and also cannot be performed whilst the aircraft is in use. Thus a revision of the conventional SHM protocol for aircraft is desired, with a move away from time consuming, periodic NDT inspection and maintenance, and a move toward continuous, in service structural health monitoring. One form of NDT which lends itself well to such a system is acoustic emission (AE). Like ultrasonic testing, AE also detects vibrational waves traveling in a structure and so would be suitable for use on composite structures. However, unlike other conventional NDT, AE is a passive monitoring technique, meaning that the signals it detects originate from within the structure under investigation itself. Since it is not necessary to actively input a signal, AE lends itself to autonomous, continuous monitoring. It is a sensitive technique with the ability to perform global monitoring of large scale structures. Furthermore, through the use of an array of sensors, AE provides the ability not only to detect but also to locate signals originating from damage, and subsequent studies have even investigated using the detected signals to characterise the source mechanism, meaning that AE could also provide information

about the nature of structural defects present. Thus, developing and implementing an autonomous SHM system which utilises AE is an endeavour of significant importance, and one which would revolutionise the manner in which the aviation sector ensured the airworthiness of its aircraft.

## 1.3 Acoustic Emission (AE) Monitoring of Aerospace Structures

The most extensive uses of AE in practice are currently the monitoring of pressure vessels and welded joints, and ASTM standards exists for each of these (ASTM 2011; ASTM 2012c; ASTM 2012a; ASTM 2012b). Whilst AE has seen much use on aerospace materials and structures in laboratory/research studies, examples of its industrial application to real aerospace structures are scarcer. One reason for this is that it is only recently that technological advances have improved the capability of AE systems to the level where they can accurately record and store the vast number of waveforms released during testing. As the accessibility of this technology increased so too did its use and subsequently, advances in the understanding of AE signal propagation were made (Holford et al. 2009). However, despite the increase in AE's popularity brought about by these advances, the stringent regulations surrounding aircraft safety demand rigorous research and trials of a new technology before it can be implemented and so AE's use in this field is still limited. One aerospace application of AE which is gaining momentum is the Acoustic Emission-Helicopter Health and Usage Monitoring System (AE-HUMS), a system for detecting damage in helicopter drivetrains. Via a method of attaching AE sensors to drivetrain components, the AE-HUMS has been found to be capable of detecting a variety of damage processes, including cracking, and can even estimate relative damage severity (Finlayson et al. 2001). AE-HUMSs have yet to receive certification from aviation authorities such as the Federal Aviation Administration (USA) and the Civil Aviation Authority (UK) due to the newness of the technology and the lack of data to verify them however, a number of HUM systems are currently being utilised in-flight in the North Sea area to collect this data (de Silva 2007). Another notable aerospace application of AE is its use on board the International Space Station (ISS)

where AE transducers have been mounted on the inside walls of the ISS to monitor background levels of ultrasonic noise in order to detect and locate the presence of leaks (Prosser & Madaras 2011).

Through examples such as these, the potential use of SHM in the aviation sector has gained the attention of key institutions and when interviewed for an article in High Performance Composites Dr D. Roach of Sandia National Laboratories stated that "*the aviation industry has recognized the need for more sophisticated structural health monitoring systems*" (Roach 2007). AE could provide a means of detecting, locating and characterising damage in such an SHM system, however, more robust and advanced analysis techniques must be developed in order to derive the most comprehensive and useful information from the data collected.

## 1.4 Aims and Objectives

Whilst the design of a fully autonomous SHM system is the long term goal for many researchers in this field, the magnitude of such a task is beyond the scope of this study and the work contained in this thesis aims instead to improve the monitoring techniques and analysis methods required for the implementation of AE in an SHM system in the future. Particular emphasis is given to the monitoring of the materials and structures typical of civil aircraft. The key objectives of this study were:-

- To increased understanding of the advanced AE damage location technique, *delta-T mapping*, and optimise this technique for use on composite specimens with complex geometries
- The development and experimental investigation of more efficient methods of collecting AE data for long term monitoring applications
- To develop and demonstrate a method of determining the orientation of AE sources, in order to assist in the characterisation of AE signals arising from different damage mechanisms in composite materials

- The advancement of the ability of AE to detect, locate and characterise damage in large-scale composite structures

## 1.5 Thesis Organisation

This chapter provides an overview of the motivations for the development of civil aircraft and the resulting need for an improved SHM system for use on those aircraft. AE was identified as a potential asset for SHM and the objectives of this research were declared.

Chapter Two discusses the background theory relevant to this thesis, with a focus on the principles of AE source mechanisms, wave propagation, source location and signal characterisation. The relevant structural materials commonly found in aircraft are also described in detail.

Chapter Three explains the instrumentation, procedures and experimental techniques commonly used throughout this work.

Chapter Four gives the details of an investigation into the effect of the *delta-T mapping* technique's training grid resolution on the accuracy of the results obtained when it is used to locate artificial sources in a complex composite specimen.

Chapter Five discusses the development of a more computationally streamlined means of recording AE data and demonstrates its effectiveness during a fatigue test on a high-strength steel specimen in which AE was used to detect, locate and track the progression of a fatigue crack.

Chapter Six includes the explanation of an improved AE characterisation technique specifically for use in flat panel composites. The technique's effectiveness was demonstrated in a buckling test on a large-scale carbon fibre composite specimen where AE is used in this case to detect, locate and characterise different sources of damage arising in the specimen.

Chapter Seven summarises the conclusions from this thesis and discusses potential directions for future work.

# 2 Background Theory

## 2.1 Aerospace Materials

Since their conception aircraft designs have undergone constant modifications from one release to the next, from minor iterations to complete overhauls, and this is a process that continues today. There have been design changes borne out of the necessity for structural integrity; design changes borne out of the desire to produce a higher performance aircraft; design changes driven by market needs and customer demands; and, more recently, design changes driven by the desire to reduce the impact of aircraft on the environment (Boyne et al. 2015; Gudmundsson 2014). Throughout any design process material selection is of paramount importance, and this is no less true for aircraft design. Over the years, advances in materials and manufacturing methods have increased the scope and versatility of materials available for use in aircraft, and a comparison between the wood and fabric airplanes of the early 20$^{th}$ Century with the metal and advanced composite material airplanes of the early 21$^{st}$ Century shows clearly how far the design of airplanes has come due in part to the introduction of new materials, as shown in Figure 2.1. In fact material advancements can be seen to have played a vital role in the success of the Wright brothers' famous first flight in 1903. It was their new aluminium engine which allowed the provision of sufficient power at a low enough weight to make powered flight feasible for the first time (Hitchens 2015).

One of the most notable changes in the evolution of aircraft is their increasing size, another achievement made possible by material advancements. For instance, the use of metals, which are stronger and stiffer than wood, enabled the pioneer Prof. Junkers to initiate the industry shift away from the biplane, towards a wider spanned monoplane (Hirschel et al. 2004). The concept took a few years to catch on, and even after the introduction of Junker's all-metal airplane in 1915, wood and wire assemblies still competed for market share on an equal footing right up through to the mid 1930's. However, by the turn of the decade aluminium aircraft, with their semi-monocoque

construction, had surpassed their wooden counterparts (Brooks 1967). Once pioneers had gained experience working with metal for aircraft, they began to build bigger wings. Bigger wings generate more lift, allowing aircraft to gradually become larger and larger as engineers surpassed the limits of what was previously deemed achievable.


*Figure 2.1: Aircraft from the early stages of the 20th and 21st Centuries. Top: World War I Bristol Scout predominantly made from wood and fabric with wire bracing, figure reproduced from Jakab* (1999)*; bottom: Airbus A350 XWB predominantly made from aluminium and advanced composites, figure reproduced from Avioners* (2014)

Since the surge in aircraft design development which occurred between 1945 and 1960, which birthed the concept of jet aircraft and subsequently the Boeing 707, the overall appearance and configuration of civil jetliners has remained relatively consistent (Torenbeek 2013). The majority of jetliners have their wings positioned below a cylindrical fuselage, with jet engines supported in nacelles on the leading edge of the wings. One of the stand out reasons for the limited variation is the conservative culture

inherent in the civil aviation industry, which dissuaded airplane manufacturers from deviating greatly from this accepted configuration out of concern for losing the interest or trust of their customers who typically err on the side of caution, preferring reliability and safety first and foremost. However, whilst the visual aesthetic of aircraft remains relatively unchanged, the same cannot be said of the materials. There has been a relentless drive towards the use of lighter materials which appears to have crescendoed in the last ten years, during which time Boeing and Airbus have begun manufacturing airplanes with over three times the amount of advanced composite materials than any of their predecessors (AirBus 2015; Hale 2008). However, there is still no 'perfect material' which is ideal for all design scenarios. Instead, all of the materials available possess their own advantages and disadvantages. The following section looks to take the reader through a number of the materials most commonly used as structural members in modern day aircraft, namely the ones experimented on in this thesis.

### 2.1.1 Aerospace Metals

The first successful introduction of metals into the design of aircraft can attributed to the Wright Brothers for their aluminium engine, though it is the German engineer, Prof. Hugo Junker, who is known for developing the first all-metal aeroplane (Hirschel et al. 2004). Junkers' early design incorporated an aluminium-copper alloy called duralumin for use as the skin material. Years later, aluminium alloys remain the most commonly used metals for aircraft structures. Alongside aluminium, titanium and steel alloys also see significant use in aircraft structures.

Boeing and Airbus are the two largest aircraft manufacturers in the world and their latest flagship civil aircraft, the 787 and the A350 XWB respectively, incorporate aluminium, titanium and steel in the quantities shown in Table 2.1.

Since its development, aluminium has been the structural material of choice in aircraft construction, owing to its superior strength-to-weight ratio in comparison to steel, and to its natural corrosion resistance. A four digit numbering system is used to describe the

composition of aluminium alloys, with common alloying elements including copper, manganese, magnesium silicon, chromium, zinc, and more recently, lithium. The most common aluminium alloy currently used for aerospace purposes is 7075 which incorporates between 5.6-6.1% zinc, 2.1-2.5% magnesium and 1.2-1.6% copper (Mraz 2014). 7075 aluminium's widespread use is likely due to the fact that it is one of the strongest aluminium alloys available, with strengths comparable to that of steel.

*Table 2.1: Metal composition of Boeing 787 and Airbus A350 XWB* (Hale 2008; Airbus 2015)

| Metal | Boeing 787 | Airbus A350 XWB |
|---|---|---|
| **Aluminium** | 20% | 20% |
| **Titanium** | 15% | 14% |
| **Steel** | 10% | 7% |

The use of copper and zinc in an aluminium alloy give it the added potential to be heat treated; either softened or hardened depending on the process used. The tempered state of an aluminium alloy is indicated in the coding system, by a letter and number combination that follows the four digit alloy number code. The most common temper designations used in aerospace structures are T3 and T6; where T3 signifies that the alloy have been solution heat-treated and cold-worked by the flattening process and T6 signifies that the alloy has been solution heat-treated and artificially aged (Experimental Aircraft Info 2015).

Titanium has a density approximately 60 percent greater than that of aluminum and 50 percent less than that of stainless steel. It boasts one of the best strength-to-weight ratios and natural corrosion resistance of all metals (Federal Aviation Administration 2008), and is also capable of operating at up to 600°C. Because of this titanium finds use in a wide variety of ways on aircraft, from fuselage skin and landing gear to engine housing and propeller blades. Despite its generally superior properties, over the years, steel alloys have typically been selected for use over titanium due to the high material costs

associated with titanium (Industrial Talks 2012). Titanium is also notoriously difficult to machine on account of its high hardness, and this has likewise limited its use.

Steel, an alloy of iron and carbon, is the most popular construction metal in the world and is available in three main divisions, which are determined by the amount of carbon present;

- Low carbon steel containing 0.05 to 0.2% carbon
- Medium carbon steel containing 0.2 to 0.8% carbon
- High carbon steel containing 0.8 to 1.5% carbon

Above 1.5% carbon content the alloy is often referred to as cast iron. Low carbon steels are ductile and often used for secondary structural components; medium carbon steels are especially adaptable for machining or forging and are often used for applications where high surface hardness is desirable; and high carbon steels are very hard and wear resistant, and are commonly used to make flat or coiled springs (Federal Aviation Administration 2008).

A host of alloying elements - namely manganese, nickel and chromium - can be added to steel to improve the properties of steel, such as its strength, toughness, wear resistance, corrosion resistance and hardenability. Hence, due to the diversity of forms in which it exists, steel can be adapted for a large variety of applications. Summarised by the Federal Aviation Administration (2008), the most common steels found in use on aerospace structures are given in Table 2.2.

*Table 2.2: Common Aerospace Grade Steels*

| Steel Type | Properties | Application |
|---|---|---|
| **Nickel steels** | Increased hardness, tensile strength, and elastic limit compared with plain carbon steel, without a large difference in the ductility. Intensifies the hardening effect of heat treatment. | Bolts, terminals, keys, clevises, and pins |
| **Chromium steel** | High in hardness, strength, and corrosion resistant properties. Particularly adaptable for heat-treated forgings which require greater toughness and strength than may be obtained in plain carbon steel. | Balls and rollers of antifriction bearings |
| **Chrome-nickel Steel (Stainless steel)** | Combination of the properties of Nickel and Chromium steels. Highly anticorrosive. Its strength may be increased by cold working. | Exhaust collectors, stacks and manifolds, structural and machined parts, springs, castings, tie rods, and control cables |
| **Chrome-vanadium steels** | High strength, toughness, and resistance to wear and fatigue (after heat treating). Can be cold formed into complex shapes | Springs, ball and roller bearings |
| **Chrome-molybdenum steel** | Larger ultimate strength when compared with plain carbon steel, without detrimentally affecting the ductility or workability. Tough, wear resistant and harden throughout entire thickness when heat treated. Especially adaptable for welding. | Welded structural parts and assemblies. Fuselage tubing, engine mounts, landing gears, and other structural parts |

#### *2.1.1.1 Failure Mechanisms of Aerospace Metals*

Engineering components can fail due to a number of different mechanisms including corrosion, fatigue, brittle fracture, overloading, creep and wear/abrasion/erosion (Findlay & Harrison 2002). Since they are designed in a robust and conservative manner with an adequate safety factor for all of the predicted working loads, it is near unheard of for an aircraft component to fail due to yielding or brittle fracture during normal operation. Furthermore, the likelihood of corrosion and wear can be reduced through appropriate material selection and thus, the most dominant form of failure on aircraft components if fatigue cracking (Bhaumik et al. 2008). Fatigue cracking is defined as the failure of a structure under repeated loading at magnitudes which would not otherwise cause failure after a single application. Aircraft have long life cycles over which they see continuous

use and so it is understandable that they are prone to fatigue. It has also been observed that due to the increasing costs of replacement, many aircraft are being operated longer than their original designed life span (Findlay & Harrison 2002), which acts to increase the likelihood of fatigue failure.

Fatigue cracking is a complex and intricate process, though its description is often simplified to three main phases; crack initiation, crack propagation, and brittle fracture (NDT Resource Centre 2013). The most widely accepted explanation of crack initiation is that which was proposed by Wood (1958), who described how the movement of dislocations can lead to microcrack formation (Suresh 2003). Wood stipulated that, during cyclic loading, the repeatedly applied stresses cause dislocations to move along slip bands, a phenomena explained by Tilley (2004), which are often at 45° to the loading direction. The dislocation movement along slip bands accumulates at the surface of the material, which causes microscopic extrusions and intrusions, Figure 2.2 (a). It should be noted that intrusions, otherwise known as micronotches, are not exclusively caused by the movement of dislocations; for instance, it is possible for manufacturing processes to leave a material scared with micronotches. Micronotches act as stress risers, promoting even greater levels of slip and eventually the formation of a microcrack.

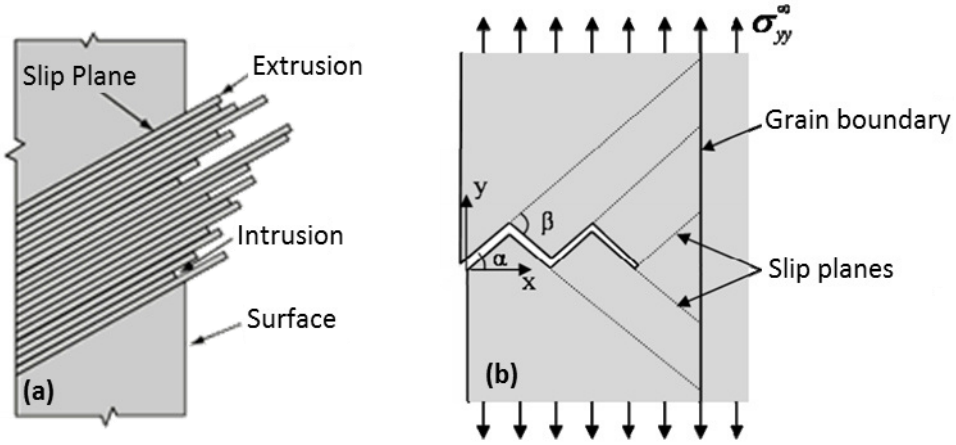


*Figure 2.2: (a) Schematic showing the gathering of dislocations to form a slip plane and the extrusions and intrusions which subsequently appear at the surface, reproduced from NDT Resource Centre* (NDT Resource Centre 2013) *(b) Geometry of microcrack, reproduced from Hansson and Melin* (2004)

Further research, reviewed by Man et al (2009), identified the precise mechanism by which microcracks initiate from intrusions in persistent slip bands (PSBs). PSBs are bands of concentrated cyclic strain; they are referred to as 'persistent' since, if all surface extrusion and intrusion features were removed via etching and polishing, continued cyclic loading would result in these surface features appearing again, in the same locations as they were before removal (Polák 2013). The movement and complex interaction of dislocations in a PSB leads to the continued growth of the intrusions. Eventually, an intrusion will grow so sharp that irreversible shear deformation occurs at its tip, producing a new surface, thus marking the initiation of a microcrack (Polák 2013).

Once a crack has initiated, crack propagation can begin. Fatigue crack propagation is said to consist of three stages; stage I, microcrack growth; stage II, long crack growth; and stage III, brittle fracture (Totten 2008). Note that the final stage of crack propagation listed here, brittle fracture, is also the final phase of the fatigue cracking process as defined above. During stage I, the growth of microcracks occurs by single shear along slip planes (Suresh 2003), Figure 2.2 (b). This is a slow process, which is highly dependent on the size and orientation of grains in the material (Hansson & Melin 2004). Thus cracks will exist in stage I, where their length is no more than several grain diameters in size, for the majority of their existence. After continual growth, the stress concentration at the tip of a microcrack will reach a magnitude which is sufficient enough to allow the development of slip in different planes, close to the crack tip; thus marking the initiation of stage II propagation. During stage II, localised yielding and work hardening occurs around the crack tip as a result of the stress concentration caused by the crack itself. The work hardened region surrounding the tip provides the growth medium by extruding forwards as the crack closes, with growth occurring in a direction perpendicular to the applied tensile stress (NDT Resource Centre 2013). Crack propagation continues in this manner until the remaining, uncracked section of the component can no longer support the load, and the material fails by brittle fracture. This

short lived, overloaded, brittle fracture growth is referred to both as stage III of crack propagation, and the third and final phase of the fatigue cracking process.

Whilst the explanation of fatigue cracking provided above consists of rigid, staged processes, in reality the transition from crack initiation to crack propagation is more of a subjective matter. Rolfe and Barsom (1977) go as far as to describe the question of "when does crack *initiation* become crack *propagation*?" as a somewhat philosophical one, with the answer ultimately depending on the level of observation. Suresh (2003) mirrors this statement by suggesting that the definition of crack initiation is subjective, and dependent on the context; for a materials scientist, the accumulation of dislocations along persistent slip bands is likely to be considered as the initiation of cracking; whereas a mechanical engineer might consider a crack to have initiated only once it has reached a length/size which is measureable by a specific detection method. Whichever the definition, fatigue cracking has been such a pervasive and consistent problem for structures of all sizes, and in all walks of engineering, that a number of methods for predicting fatigue crack growth have been developed.

The most direct approach to determining the fatigue life of a component involves manufacturing a batch of samples and cyclically loading them, in the manner in which they would be loaded when in service, until failure. The magnitude of the load should be incrementally increased from one specimen to the next and the maximum number of cycles to failure must be recorded. Once this have been completed for several specimens, a graph of stress against the number of cycles until failure (known as an S-N graph) can be produced and subsequently used to predict the fatigue life expectancy of a component, resembling the specimens, for a given loading level. However, this process involved manufacturing multiple components purely for the sake of damaging them and some loading scenarios are difficult to replicate, and so it can be costly, time consuming and impractical.

In 1957, George R Irwin developed the *stress intensity* approach which can be used to determine the stress required for a crack to grow. The technique relies on the principle that all of the stress components near the crack tip are proportional to the applied stress and the crack length (Irwin et al. 2000) via Equation 2-1.

$$K = Y\sigma\sqrt{\pi a}$$

*Equation 2-1*

Where *K* is the stress intensity, *Y* is a shape factor introduced to deal with different geometries, σ is the applied stress and *a* is half the crack length. If the stress intensity calculated is greater than the critical stress intensity for that specific geometry then it is predicted that the crack will grow. This is an accessible method for predicting fracture growth since the flaw shape factors for many geometries have already been calculated and can be obtained from handbooks for use in design, saving time and money.

However, whilst offering a convenient means of determining whether or not a crack will grow during a single loading, the stress intensity approach does not accommodate for cyclic loading and hence fatigue cracking. In a bid to solve this issue, after numerous trials, Paris et al (1961) discovered that a linear trend appeared when a plot of the stress intensity range (Δ*K*) against crack growth rate (*da/dN*) was plotted in a log-log graph, which lead to the development of the Paris Law, Equation 2-2, where *C* and *m* are material constants. The Paris Law states that the rate of crack growth is proportional to the stress intensity factor range; thus, since the stress intensity factor is proportional to the applied stress and crack length, for a constant cyclic stress range, the rate of crack growth is proportional to the crack length.

$$\frac{da}{dN} = C\Delta K^m$$

*Equation 2-2*

### 2.1.2 Carbon Fibre Reinforced Plastic

Carbon fibre reinforced plastic is a composite material, and is commonly referred to as 'CFRP', 'carbon fibre composite' or simply 'carbon fibre'. Composite materials consist of a combination of materials joined together, typically shards or fibres of a strong/stiff material embedded in a softer binding material. Within a composite, the individual constituent materials do not dissolve or merge, and can instead be physically identified from one another (Jones 1999). The bond between the constituent materials must be strong enough so that loads can be transferred from one to the other and they act together as one.

There are many naturally occurring composite materials which existed long before engineers developed the concept. Classic examples of these are wood, which is a composite of cellulose fibres in a lignin matrix, and bone, which is a composite of collagen fibres embedded in an hydroxyapatite mineral matrix (Cha 2013). Within composites the properties of the two constituent materials are combined to form a new material which has properties which are optimised for its purpose; this is the benefit of composites.

As one might expect, a carbon fibre reinforced polymer composite consists of carbon fibres embedded in an epoxy resin matrix. In this instance the property combination is thus; the carbon fibres are very stiff but also brittle and difficult to form, so are of little use on their own; the epoxy resin is tough but has poor load bearing properties; when combined the stiff fibres can withstand loading in both compression and tension, and the matrix can support the fibres against buckling as they carry these loads and helps them hold their form (Roeseler et al. 2007).

When referred to in relation the aerospace industry, the carbon fibre composites utilise long fibres, Figure 2.3, though short fibre composites also exist. Within these advanced aerospace composites, the orientation of the fibres are aligned which means that the resulting composite has highly orthotropic properties, tending to be very stiff in the direction of the fibre orientation. The fibres themselves are thin, so having just a single

layer results in an impractically thin structure, thus composite materials are typically built up in layers, or plies. The orientation of the fibres from one ply to the next can be varied in order to give the composite formed bidirectional material properties.

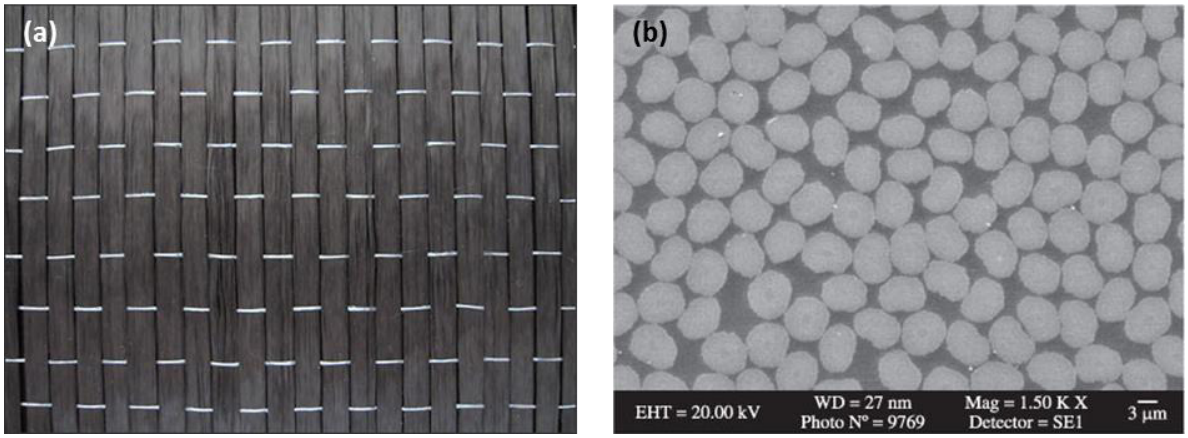


*Figure 2.3: (a) Top down view of unidirectional woven carbon fibres before being added to the matrix, reproduced from Carbon Fiber Australia* (2014) *and (b) a longitudinal view scanning electron microscope image of carbon fibres when embedded in a matrix, reproduced from Srinivasa et al* (2010)

When loaded in the fibre orientation, carbon fibre composite has a superior strength-to-weight ratio compared with conventionally used aerospace metals such as aluminium, titanium and steel (Roeseler et al. 2007) which makes them ideal for use in aircraft. Numerous sources state that weight savings of up to 20% are achievable through the use of composite materials over conventional metals. However, as mentioned, carbon fibre composite has highly orthotropic properties and so would not be appropriate for use in every scenario; metal components could not simply be exchanged, like-for-like, with a carbon fibre components without first seriously considering the loading scenario at hand. Nevertheless, during the Second World War the first composites appeared in aviation, to form aircraft cabins, propeller hubs, and insulation for electrical cabling (Brownlee et al. 2014).

Since their introduction, composite material usage in aircraft has seen a steady increase. Initially their use was limited due to people's unfamiliarity with them, and the limited manufacturing expertise and lifecycle information available. However, the more they were used, the more they proved their worth, and the industries understanding of their

behaviour grew. Combined with the advancements made to the manufacturing methods, these factors have brought about a boom in the use of composites on aircraft in recent years, Figure 2.4. Airbus and Boeing's most recent civil aeroplanes are now manufactured using 50% or more composite materials as a percentage of their mass, with the majority of that being carbon fibre composites.

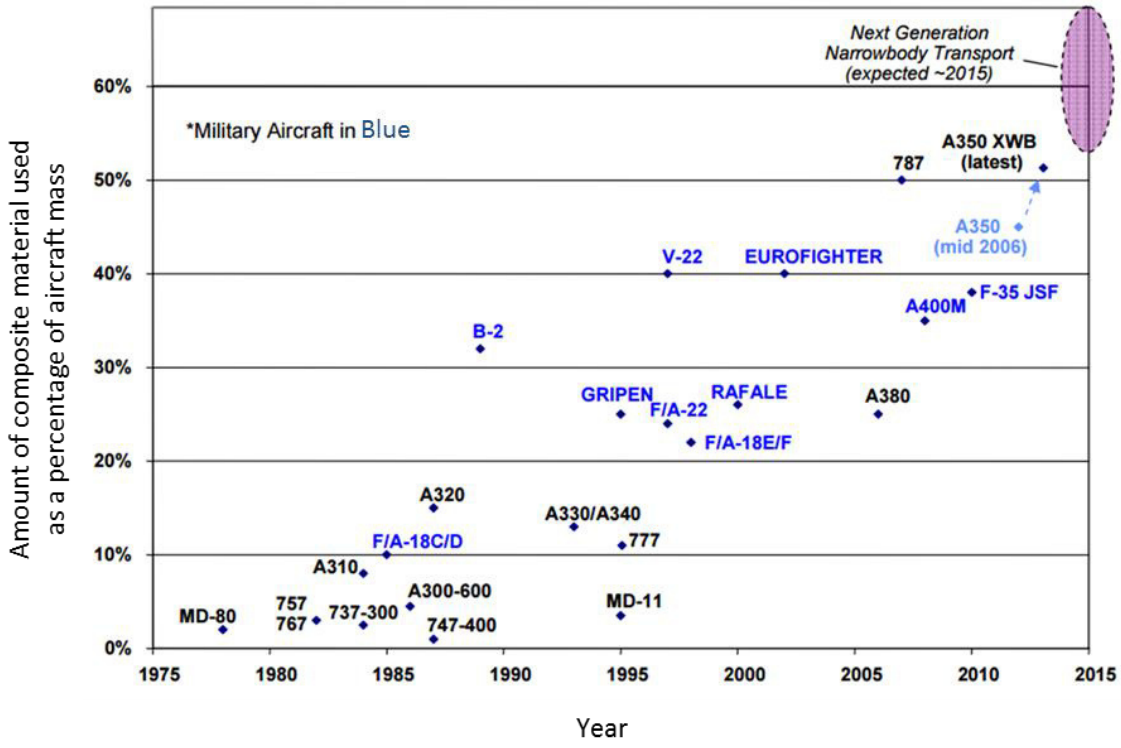


*Figure 2.4: Quantity of composites used on popular airplanes as a percentage of aircraft weight from 1975 to 2015, figure reproduced from Aboulafia* (2015)

With such large quantities of composites being used it is more important than ever before to develop effective non-destructive evaluation techniques for them.

### *2.1.2.1 Failure Mechanisms of Carbon Fibre Composite*

Due to their complex structure, carbon fibre composites exhibit a multitude of failure mechanisms. Firstly, each of the constituent materials can fail independently; matrix cracking and fibre fracture. Secondly, it can exhibit failure mechanisms related to the debonding of various elements of the composite. As mentioned previously, a strong adhesion between components in the composite is essential to allow the transfer of load from one part to the next, so disbonds are detrimental to their performance. Disbonding

occurs in two main ways; delamination between layers in the composite and debonding between the fibres and matrix.

Matrix cracking occurs in the polymer matrix part of the composite and, on account of it requiring such low levels of energy to induce, is one of the most common damage mechanisms in composite materials such as CFRP and generally the first to occur (Sadeghi et al. 2014). Matrix cracking occurs in a wide variety of ways, it can be internal, i.e. occur in one of the inner plies in the composite, or external, i.e. occur on one of the outer most layers. Matrix cracks can also be oriented in many different directions including longitudinally to the fibres, in the form of a 'split', or perpendicular to the orientation of the fibres. Matrix cracking can also occur in the plane of the composite, or out of the plane of the composite. The type of matrix cracks which develop are a function of the material layup, loading orientation and the quality of manufacture.

The effect of matrix cracking on the mechanical performance of the composite also varies, depending on the severity of the cracking and loading conditions. Under tension, it is generally agreed that small amounts of matrix cracking do not reduce the strength of the composite by any noticeable degree, however they can eventually cause issues as they nucleate other damage mechanisms (Nairn 2000). Alternatively, in compression the matrix bears more of the load and has a larger bearing on the properties of the composite, (Fleck 1997). Thus matrix cracking has been found to have a larger impact on the mechanical properties of composites under compression and produce a noticeable reduction in strength (Lee & Soutis 2007).

Fibre fracture is the failure of the fibres within a composite by fracture, typically either in a brittle manner of via fatigue, Figure 2.5. Fibre fracture is considered to be a more severe damage mechanism that matrix cracking as it is the fibres that bear the majority of the loads applied to the composite. Carbon fibre composite laminates with artificially fractured/cut fibres have been shown to have reduced tensile strength compared to undamaged specimens (Yashiro & Ogi 2009).

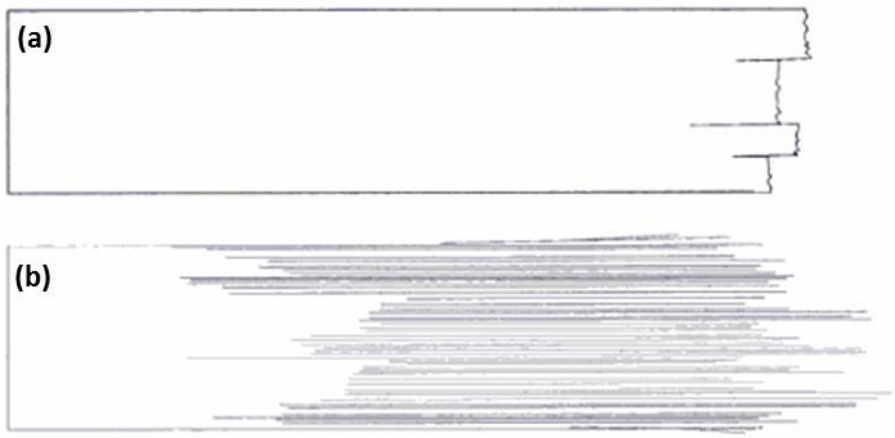


*Figure 2.5: Example of the appearance of carbon fibre coupon specimens which have failed as a result of (a) brittle fibre fracture under large single loading (b) fibre fracture by fatigue, figures reproduced from Harris* (2003)

Delamination is the term used to describe the disbonding of plies, or layers, in a composite. Delaminations are a sign of severe damage in a composite and are usually the damage mechanism that leads to catastrophic failure of the structure. Delaminations are of particular concern for compressive loading regimes where their presence has been reported to reduce compressive strength by up to 60% (de Moura et al. 2000).

Just as the constituent parts of composite materials are strongly interlinked, so are their damage mechanisms, and it is rare for a composite component to fail by just a single mechanism. Instead, failure in composites is a gradual sequence of escalating events which lead up to structural collapse (Hintona & Soden 1998). For instance, if the build-up of matrix cracking occurs in the region between layers of the composite then it can lead to delamination (Federal Aviation Administration 2012); the reduction in stiffness caused by the delamination could result in regions of the composite experiencing more strain and hence cause additional matrix cracking, as well as fibre fracture.

As well as an individual damage mechanism leading to the introduction of another, certain loading conditions can induce multiple damage mechanisms in a single instance. For instance, impact loading of composites poses a great danger as they are reported to frequently give rise to delamination, matrix cracking and fibre fracture, Figure 2.6.

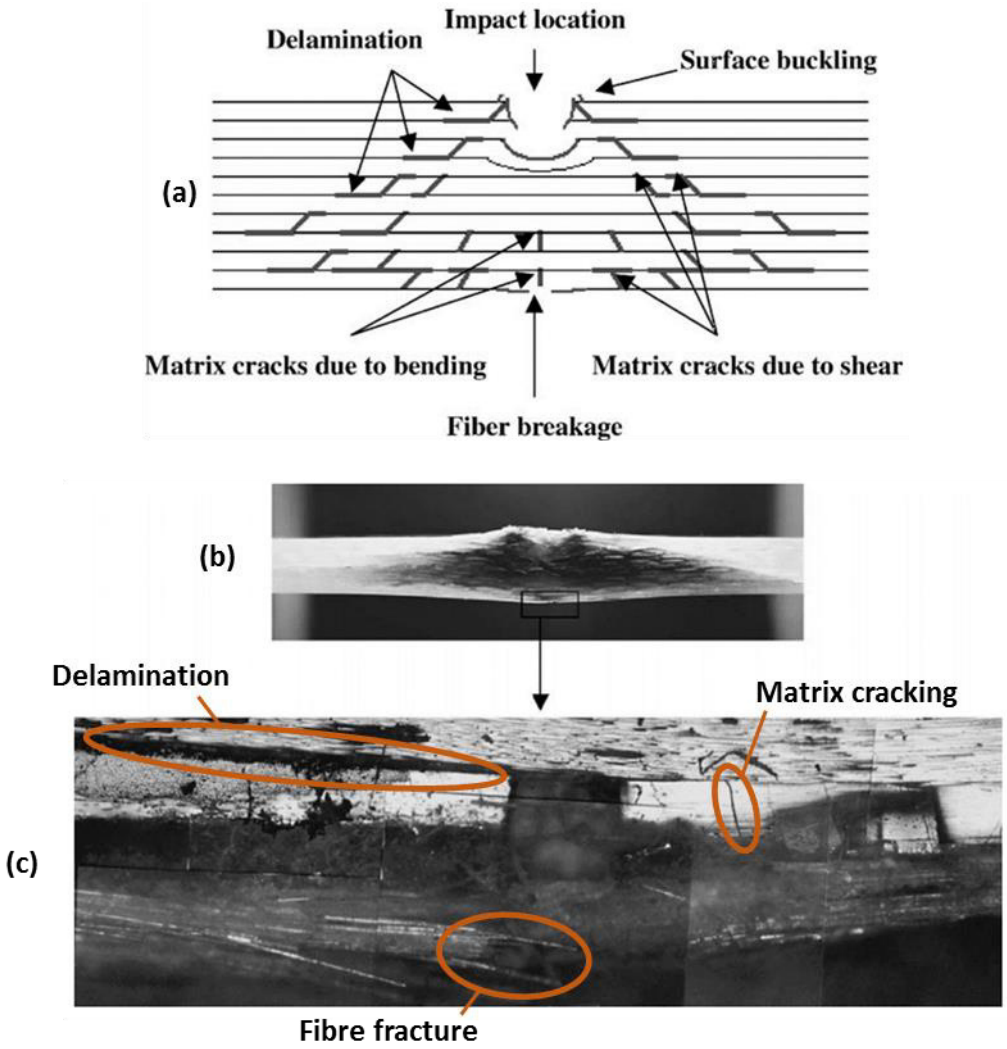


*Figure 2.6: (a) Schematic of damage mechanisms caused by impact (b) photograph of impacted section (c) metallographic photo of impacted area shows delamination, matrix cracking and fibre failure in practice, figures reproduced from Shyr & Pan* (2003)

Compressive loading is also of particular relevance to composites such as CFRP as these materials can have compressive strengths as much as 60% less than their tensile strength (Fleck 1997) owing to the fact that the load is distributed more evenly between the fibres and the matrix.

### 2.1.3 GLARE

GLARE, which stands for 'glass laminate aluminium reinforced epoxy', is a fibre metal laminate (FML) consisting of layers of aluminium and glassfibre composite material. It is typically formed from thin aluminium alloy sheets (Al-2024- T3 or Al-7475-T6) in the range of 0.3-0.5 mm thick, layered with glassfibre composite in the range of 0.25-0.5mm

thick (Sinke 2003). Each of the glassfibre composite layers within GLARE is comprised of two to four unidirectional prepreg plies, which can be oriented in either one direction, resulting in a unidirectional-laminate, or in two directions, resulting in a cross-ply laminate (Sinke 2009). Once the desired layup is decided the layers are assembled and bonded together, Figure 2.7.

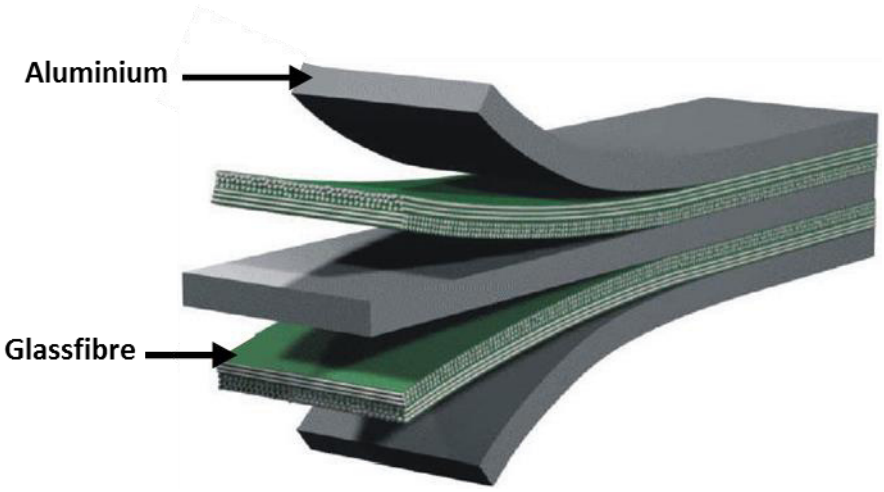


*Figure 2.7: Exploded conceptual image of GLARE demonstrating each of the layers, figure reproduced from Composite Materials* (2015)*. This particular layup incorporates glass-fibre plies in alternating directions.*

FMLs were developed in an attempt to provide a solution to the low impact resistance of composites and the low fatigue resistance of aluminium. Two main types of FML are available commercially, ARALL and GLARE, which were developed at Delft University in conjunction with Fokker (Sinmazçelik et al. 2011). After extensive testing and research was conducted on the new materials it transpired that the FMLs not only offered the improved fatigue and impact resistance intended, but also offered improved corrosion and fire resistance (Hagenbeek 2005), not to mention a 30% weight saving compared to monolithic aluminium.

Despite the benefits offered by GLARE, it is currently unviable to manufacture aluminium sheets of the desired thickness at the widths necessary to produce aircraft panels. However, a work-around to this problem was developed called splicing, in which the

aluminium sheets are staggered so that they can be overlaid to increase the size of the panels without having a complete break in the aluminium, Figure 2.8 (a).

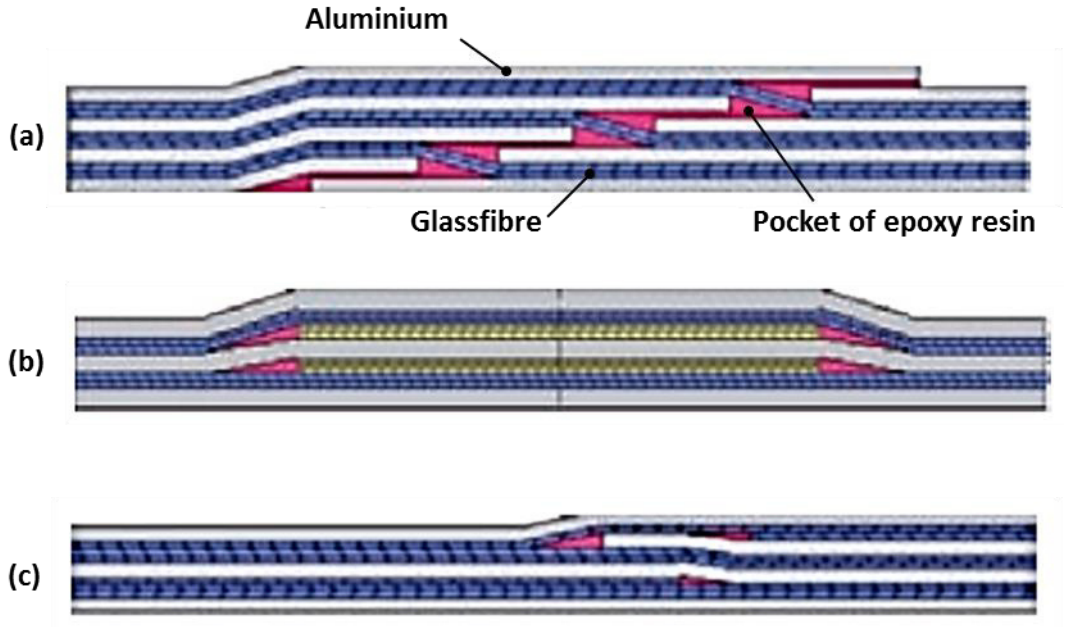


*Figure 2.8: Schematic of (a) splice in GLARE where one aluminium layer ends and another begins, (b) 'Doubler' feature, (c) transition from GLARE 3/2 to 4/3, figures reproduced from Fokker Aerostructures* (2015)

This modular approach of manufacturing GLARE allows other structural features to be included as required. For instance, in the fuselage panels manufactured for Airbus, Fokker include features called 'doublers' to reinforce regions of the fuselage that join to the frame, Figure 2.8 (b), and can easily transition from one thickness of GLARE to another if additional structural reinforcement is needed, Figure 2.8 (c).

## 2.2 Acoustic Emission (AE)

### 2.2.1 Background

Acoustic Emission is the transient elastic energy that is released by a material when it experiences a rapid change in its structure, such as plastic deformation or crack growth, and also the name given the technique of monitoring these transient elastic energy signals (Miller and Findlay 2005). In its present form, the AE technique has been used as a method of structural evaluation since the 1950s when it was brought into the public

eye by J. Kaiser (Hellier 2001). AE differs from other forms of non-destructive testing in that it detects the energy released by the structure under investigation, and no input signal is required from the operator; hence AE is defined as a passive monitoring technique. However, AE requires the structure under investigation to be carrying a load in order for detection to take place, since an unstressed defect will not emit AE.

AE refers to the detection of signals in the ultrasonic range (20kHz to 1MHz) through the use of piezoelectric transducers attached to the surface of the structure being monitored, though the AE detected is commonly within the range of 100kHz to 300kHz. As defined by Vallen (2002), and shown in Figure 2.9, the basic principles of AE testing are as follows;

1. Application of load: to produce mechanical tension.
2. Source mechanism: releases elastic energy
3. Wave Propagation: elastic energy travels as a wave from the source to the sensor
4. Sensor(s): convert the mechanical wave into an electrical AE signal
5. Acquisition of measurement data: The electrical signal is converted into an electronic data set
6. Display measurement data: The recorded data is plotted
7. Evaluation of the display: Operator makes a safety-relevant interpretation of the plots

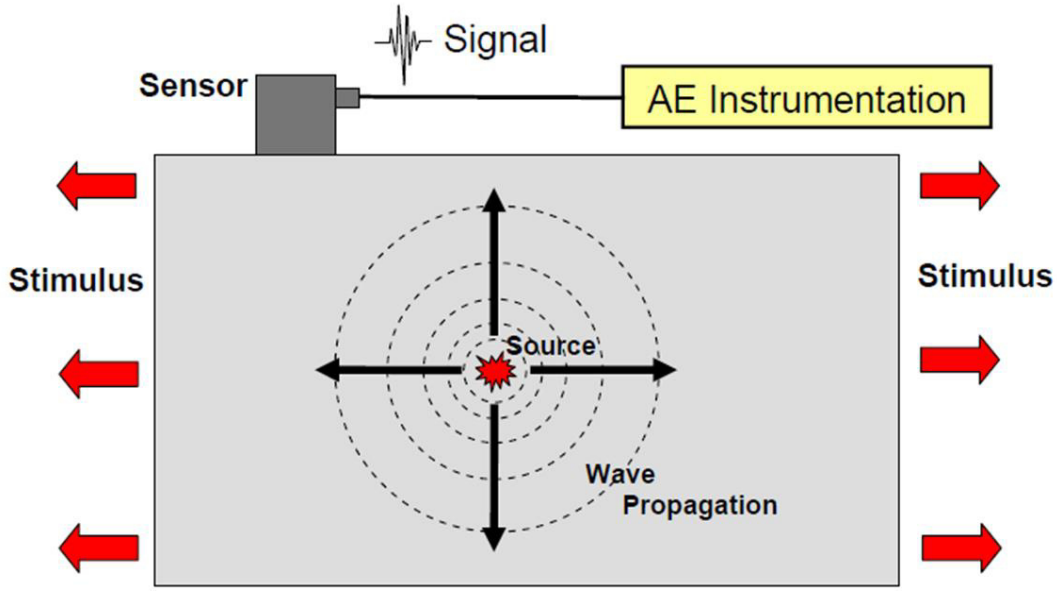


*Figure 2.9: Principles of AE monitoring, figure reproduced from ASTM* (1982)

### 2.2.2 AE Source Mechanisms

AE can originate from any mechanism which causes a rapid release of elastic energy. Sources of AE in metallic structures which have been identified in the past (Hellier 2001) are;

- plastic deformation
- microcrack formation and growth
- phase transformations
- fatigue crack growth
- corrosion
- crack-face rubbing
- cavitation

AE sources can also originate from external stimuli such as the impact of an external body on the structure under investigation or the rubbing of joints, bolts and frames.

Within the remit of AE testing, noise is considered to be any undesired signal (electrical or acoustic) that interferes with the reception, interpretation, or processing of desired signals (ASTM 1982). Generally speaking, the desired signals are those which are released directly from the damage mechanisms in a tested structure or those which contribute positively towards the detection of damage. Under this definition external

sources of AE are considered to be noise. Interestingly, despite it not being released directly from a damage mechanism, the release of AE from crack face rubbing can be useful to the detection of the crack and so is often considered desirable (Davies & Holford 1997).

Due to the fact that their material compositions are so different from one another, composite materials have AE sources which are not shared by metals, and vice versa. Plastic deformation and phase transformation are two sources of AE on the list above which do not occur in composites and the following list contains AE sources which are experienced by composited and not metals (Miller et al. 2005);

- Fibre failure
- Fibre pullout
- Fibre-matrix debonding
- Matrix cracking
- Delamination

### 2.2.3 Wave Propagation

In infinite solid media there are only two types of wave which propagate; transverse and longitudinal (Muravin 2009). The particle motion in a longitudinal wave is parallel to the wave propagation direction and their motion is driven by compressive and dilational forces. Alternatively, the particle motion of transverse waves is perpendicular to the wave propagation direction and their motion relies on the stiffness of the propagation medium to sustain itself, hence, in further contrast to longitudinal waves, transverse waves cannot propagate in a gas or liquid. Figure 2.10 gives an example of the motion of these two wave modes.

In semi-infinite media, i.e. if a surface is introduced, the interaction of the two wave modes waves interact with the bounded surface to form Rayleigh waves where particle motion is neither solely longitudinal or traverse, Figure 2.11.

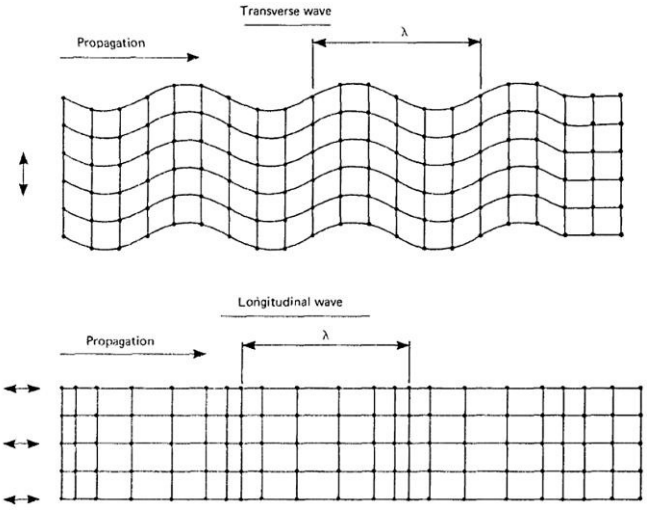


*Figure 2.10: The two basic wave modes which exist in a solid, figure reproduced from Rindorf* (1981)

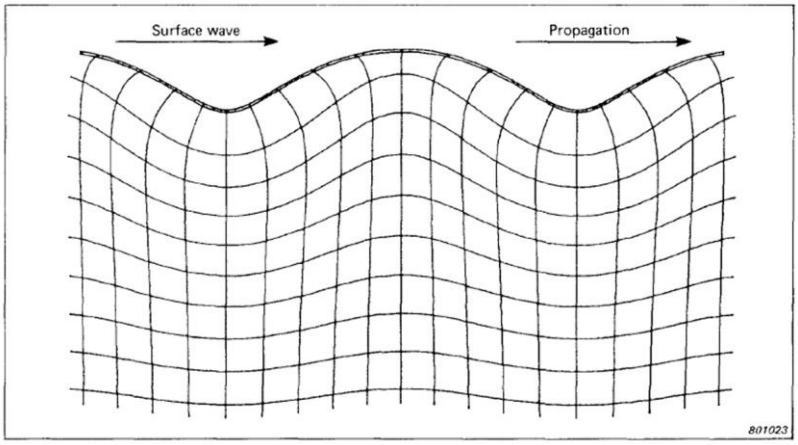


*Figure 2.11: Rayleigh surface wave, figure reproduced from Rindorf* (1981)

When a second surface is introduced and the waves become fully bound by two surfaces, as in a plate, the motion of the longitudinal and transverse waves couple to form two new waves modes known as the symmetrical, $S_o$, mode and the asymmetrical, $A_o$, mode. Together, these are known as Lamb waves, Figure 2.12. In plates with larger thicknesses it is possible for higher order extensional and flexural Lamb wave modes to develop, however they are of limited use to AE monitoring on account of their low amplitude. Due to the nature of their movement, the $S_o$ and $A_o$ modes are often referred to as the extensional and flexural Lamb wave modes respectively.

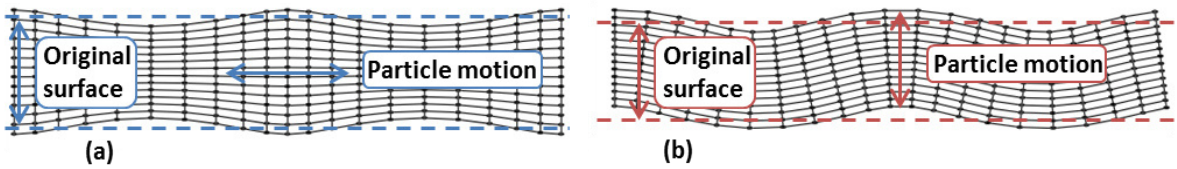


*Figure 2.12: (a) Symmetrical and (b) Asymmetrical Lamb wave modes*

Since much of an aircraft's skin is formed from thin panels, Lamb wave mode propagation is of particular relevance to the application of AE on aerospace structures and hence, of particular relevance to this thesis. Lamb wave propagation can be explained via dispersion curves. For context, consider the equation linking a wave's velocity to its frequency, Equation 2-3.

$$C = f\lambda$$

*Equation 2-3*

Where *C* is the wave velocity, *f* is the frequency of the wave and λ is the wavelength. In non-dispersive media the wave's velocity is fixed, and hence altering the frequency simply inversely effects the wavelength. However, in dispersive media this is not the case, and instead a waves velocity is dependent on its frequency (Russell 2011). This dispersive behaviour occurs when AE travels in flat plates as a result of the plate's boundaries acting as a waveguide. Under a dispersive regime each frequency has its own phase velocity;

$$C_p = f\lambda$$

*Equation 2-4*

Where $C_p$ is the phase velocity. Real AE events release a wave with a range of different, but similar, frequencies, dictated by the speed of the event, i.e. its impulse. Initially all these frequencies are superimposed on one another at the location of the event though as the wave propagates outward, the components of the wave which are higher in frequency travel slightly faster than the components of the wave at a lower frequency, and hence the energy in the wavefront is spread out, resulting in a lower peak amplitude, Figure 2.13.

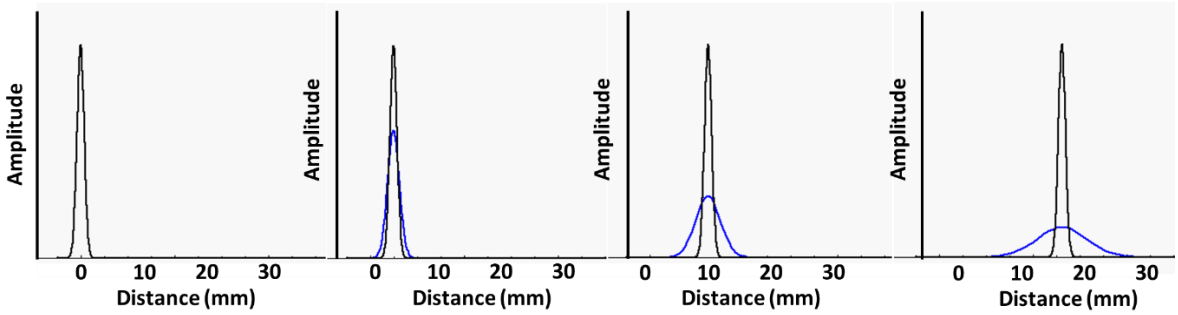


*Figure 2.13: Example of wave 'spreading' out as a result of dispersion. The black line represents the wave in a non-dispersive medium and the blue line shows the wave in a dispersive medium*

The individual frequency components, or phases, of the wave remain somewhat superimposed throughout the distance of propagation and form what is known as a wave envelope. Generally, when an AE wave's velocity is mentioned it is in reference to the group velocity. Due to the nature of their motion within the structure, the $S_o$ Lamb wave mode velocity is related to the in plane stiffness and the $A_o$ Lamb wave mode velocity is related to the out of plane stiffness. The relationship between frequency and velocity of the $S_o$ and $A_o$ Lamb wave modes can be described in a dispersion curve, an example of which can be seen in Figure 2.14.

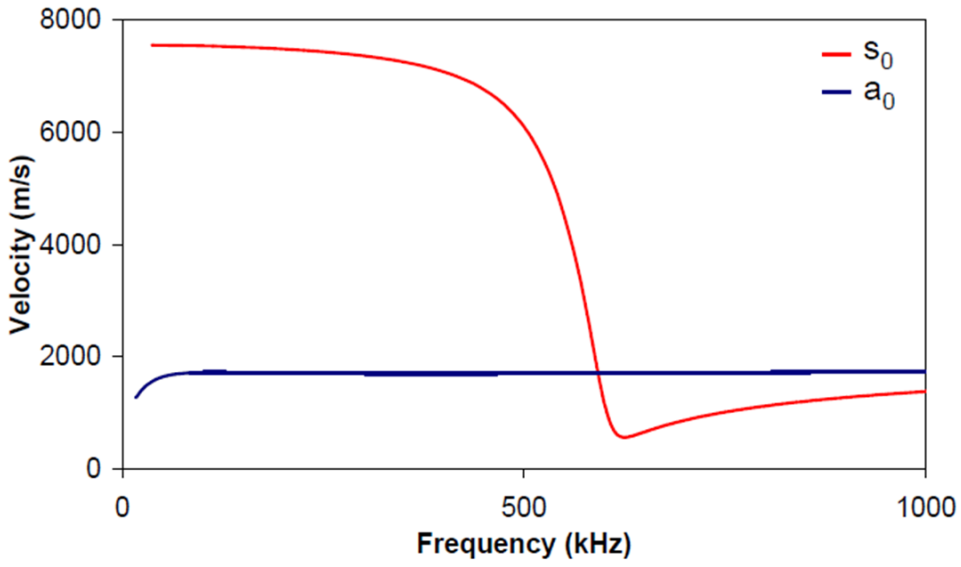


*Figure 2.14: Example of dispersion curve for the So and Ao Lamb wave modes in a composite material, reproduced from Eaton* (2007)

The occurrence of dispersion and its effect on AE waves is important to bear in mind when considering and understanding AE and the emissions perceived from a structure.

### 2.2.4 Attenuation

Attenuation is the name given to the phenomena by which the amplitude of waves traveling in a medium diminish. Rindorf (1981) and Pollock (1986) identify the following reasons for attenuation;

Geometric spreading: These effects are fundamental to wave propagation since the wave is always acting to spread throughout the medium in which it is traveling. The act of spreading itself out means that the energy in the wave front is spread more thinly and hence, the amplitude of the wave is reduced. Due to the principles of conversion of energy, geometric spreading causes the amplitude of an AE wave to decrease by 30% each time its distance from the source is doubled (Miller et al. 2005), thus the rate of signal attenuation is greatest in the initial period of wave propagation and diminishes over distance.

Absorption: The elastic and kinetic energy from the wave is lost to its propagating medium through absorption where it is converted into heat. Attenuation due to absorption is frequency dependant, with higher frequencies experiencing greater attenuation than lower frequencies.

Dissipation of energy into adjacent media: Wherever a wave meets a boundary or discontinuity some of the energy is reflected and some of the energy is lost to the adjacent media.

Wave dispersion: Wave dispersion, as described in Section 2.2.3 is the phenomena by which the energy in a wave will spread out, causing the wavefront to become longer and the peak amplitude to become smaller.

### 2.2.5 Source Location

The ability of AE to locate damage over a wide inspection area in real-time is one of its most inviting features as far as the aerospace industry is concerned. This is a stark contrast to conventional inspection methods such as ultrasonic and audible sonic testing which requires the user to manually inspect specific regions of a structure, which is time consuming and thus costly. The following section presents the most popular AE source location method in use today as well as a number of developing methods, including *delta-T mapping* which was used extensively throughout this thesis.

#### *2.2.5.1 Time of Arrival*

The conventional and most established source location technique used within the field of AE is Time of Arrival (TOA), which is explained in detail by Miller et al (2005) in the NDT Handbook. TOA is the default location technique built into commercially available AE software, and in layman's terms can be thought of as a form of location by triangulation. TOA works on the principle that if the arrival time of an AE wave is known at each of the recording sensors in an array, and the velocity of the AE wave is known, then the location of the event which produced that AE wave can be identified by comparing the differences in time of arrival of the AE wave between sensor pairs in the array, hence the name TOA. It is perhaps explained best through the use of a diagram and the supporting equations, as presented by Nivesrangsan et al (2007);

Consider the hypothetical two dimensional scenario pictured in Figure 2.15 where three recording sensors ($S_1$, $S_2$ and $S_3$) are attached to the surface of a plate in the positions ($x_1$, $y_1$), ($x_2$, $y_2$) and ($x_3$, $y_3$), respectively. $S_2$ and $S_3$ reside at a distance and angle of $D_1$, $\theta_1$ and $D_2$, $\theta_3$ relative to $S_1$ respectively. An AE source at the position ($x_s$, $y_s$) releases a wave which travels outward at a constant velocity, $c$, in all directions and arrives at $S_1$, $S_2$ and $S_3$ at the times $t_1$, $t_2$, and $t_3$, respectively.

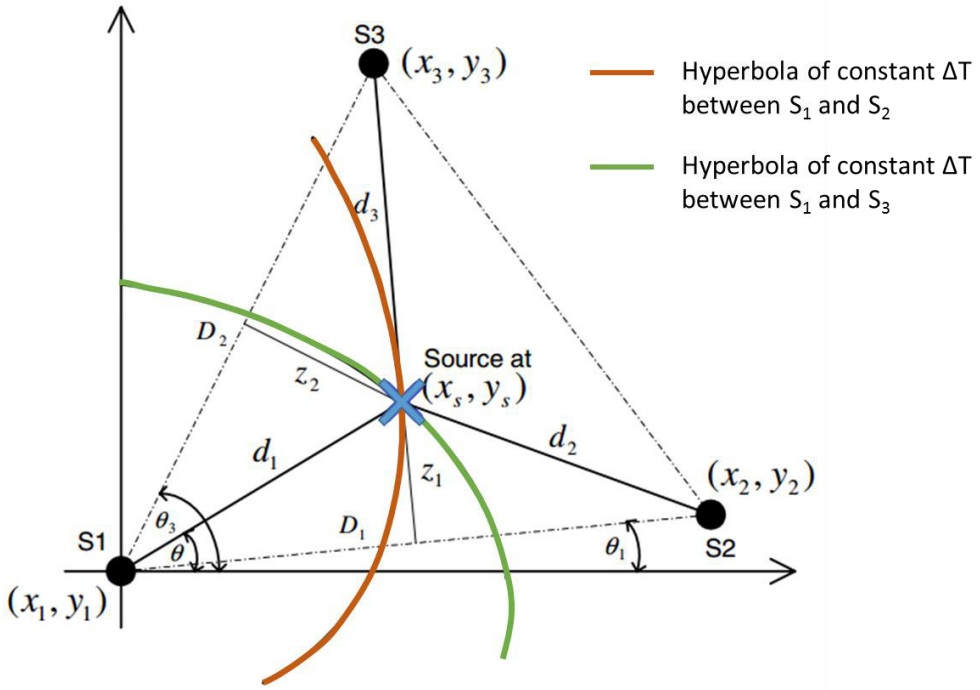


*Figure 2.15: Hypothetical 2D AE event to demonstrate the TOA calculation, figure adapted from Nivesrangsan et al.* (2007)

By taking the relative positions of two sensors from one another and the difference in time of arrival, $\Delta t_i$, between them, equations of motion can be used to calculate the equation of a hyperbola which describes all the possible positions in which the source could have been located to produce that specific Δt value for that specific sensor pair. Equation 2-5 is the equation of the hyperbola describing the source's potential positions using the data collected from $S_1$ and $S_2$, which corresponds to the orange line drawn in Figure 2.15. These hyperbolae are sometimes referred to as 'lines of constant Δt' on account of them describing a line along which any position gives the same value of Δt for a particular sensor pair.

$$d_1 = \frac{(D_1^2 - \delta_1^2)}{2(\delta_1 + D_1 \cos(\theta - \theta_1))}$$

*Equation 2-5*

Where:

$$\delta_1 = d_2 - d_1 = c(t_2 - t_1) = \Delta t_1 . c$$

*Equation 2-6*

However, Equation 2-5 does not provide one definitive position, only a range of potential positions, and information from a third sensor is needed in order to pinpoint the position

of the source in two dimensions. Thus, using the difference in time of arrival between $S_1$ and $S_3$, $\Delta t_2$, and their relative positions from one another, a second hyperbola can be defined, Equation 2-7, which gives another set of potential positions of the source. This hyperbola is represented in Figure 2.15 as a green line.

$$d_1 = \frac{(D_2^2 - \delta_2^2)}{2(\delta_2 + D_2 \cos(\theta_3 - \theta))}$$

*Equation 2-7*

Where:

$$\delta_2 = d_3 - d_1 = c(t_3 - t_1) = \Delta t_2 . c$$

*Equation 2-8*

The intersection of these two hyperbolae gives the position of the source, and theoretically, both equations could be solved simultaneously to give values for θ and $d_1$. However, in practice, due to imperfect wave propagation and slight errors in the acquisition of the wave, these equations will not necessarily be resolvable simultaneously. Instead, using the relative position of the source from $S_1$, two more equations are defined;

$$x_s = x_1 + d_1 \cos\theta$$

*Equation 2-9*

$$y_s = y_1 + d_1 \sin\theta$$

*Equation 2-10*

For a given set of input conditions; $\delta_1$, $\delta_2$ and θ, Equation 2-5 and Equation 2-7 can be used to give two values for $d_1$. Inputting these values into Equation 2-9 and Equation 2-10 will generate two set of coordinates for the location of the source ($x_s$, $y_s$) and the error, or distance, between these two sets of coordinates can be calculated. By varying the value of θ, this process can be used to iteratively determine the value of θ which results in the lowest error between the set of coordinates generated, and thus, the location of the source is obtained. By introducing more sensors, and thus hyperbolae, greater confidence can be obtained.

TOA location has been used extensively in the past to monitor many structures including wind turbine blades, bridges and piping, however it is not without its faults. A sensor begins recording an AE hit if the signal amplitude crosses the threshold. If the signal has travelled a considerable distance to reach the sensor then attenuation might reduce the signal's amplitude sufficiently that the beginning of the wave does not cross the threshold and trigger a recording. Triggering errors can lead to erroneous Δt values between sensor pairs and hence result in location errors. Triggering error such as this can also occur in AE applications with low signal-to-noise ratio, as during these applications the threshold must be sufficiently high to exclude the background noise from being recorded though this can also result in a number of *useful* AE hits going undetected or detected at the wrong moment in their arrival.

TOA also assumes uniform wavespeed in all directions which is not true for many of the materials used widely the aerospace industry, such as composites. In thin panel specimens, studies have shown the velocity of the faster moving $S_o$ Lamb wave mode, i.e. the wave mode which triggers the threshold crossing, to vary by up to a factor of three when traveling in composite materials depending on the direction of travel (Lopresto 2009). This means that the equation for the hyperbola describing the line of constant Δt between a sensor pair is no longer accurate and hence results in less accurate locations.

Finally, TOA assumes that there is a direct wavepath between the source and recording sensor which is not true for many real life structures. Geometric features such as stiffeners, holes, rivets, thickness changes and shape changes will impede the stress wave on its route from the source to the sensor and may lead to a later arrival time than would otherwise be expected. Similar to the error caused by irregular wavespeeds, this acts to invalidate the hyperbola describing the line of constant Δt between a sensor pair and hence results in location errors.

#### 2.2.5.2 Development of AE Location Techniques

The issue of triggering errors in AE was addressed by Kurz et al (2005) through the application of the Akaike Information Criterion (AIC). The AIC is an entropy based measure of the similarity between data sets which was originally developed for statistical model selection by H. Akaike in the early 1970's (Akaike 1974). Maeda (1985) saw the potential for the criterion to be used to determine the arrival time of seismic waves and developed a form of AIC calculation that could be applied directly to a recorded transient signal, Equation 2-11;

$$AIC(t) = t\log_{10}\big(var(x[1;t])\big) + (T - t - 1)\log_{10}\big(var(x[t;T])\big)$$

Equation 2-11

To utilise this function the signal is split into two parts, one from time '0' to time '*t*', and one from time '*t*' to time 'T' (the end of the data set). For a particular value of *t*, Equation 2-11 gives a measure of the similarity in entropy between the two parts of the segmented signal, and by using incrementally larger values of *t* the entire signal can be analysed. When the value of *t* is aligned with the first arrival point of the transient stress wave the AIC, i.e. the measure of similarity, will be at a minimum; this is because the region of noise recorded before the arrival of the stress wave has very little structure and thus high entropy, whereas the stress wave has a much higher structure and thus a lower entropy. Figure 2.16 provides an example of the use of the AIC on two AE waveforms, one with a high signal-to-noise ratio and another with a low signal-to-noise ratio, and demonstrates how it can be used to identify a more accurate first arrival time when compared with the conventional threshold crossing method.

However, for the AIC to correctly identify the arrival of the wave only a limited time window from within the data set should be used since, if the entire waveform is used, the arrival of secondary wave modes and/or reflections creates multiple troughs in the AIC which could lead to erroneous first arrival time determination. This lead researchers to go one step further and implement a two-step AIC picker; one which was used to define

a more precise window about the start of first arrival and a second to determine the actual first arrival time from that reduced window (Sedlak et al. 2008).

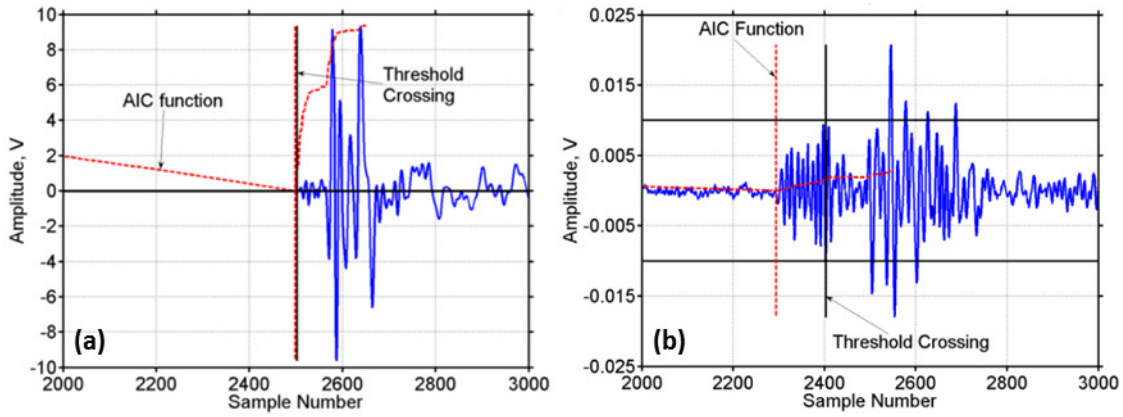


*Figure 2.16: Example application of the AIC on AE waveforms for (a) a high signal-to-noise ratio waveform and (b) a low signal-to-noise ratio waveform, figure reproduced from Pearson* (2013)*. The AIC value reaches a minimum at the intersect of the noise and the transient AE signal, hence identifying the first arrival time*

Other approaches to identify more accurate first arrival times were presented by Ziola and Gorman (1991), who highlighted individual frequencies from a recorded waveform and used a crosscorrelation technique to calculated more accurate times of arrival for that frequency, and Jeong (2001) who utilised a Gabor wavelet transform to the same effect.

Among the most promising of the non-TOA location methods are mapping techniques, one of which, the *best-matched point* method is described by Scholey et al. (2009). During the *best-matched point* method a computational model of the structure under inspection is created, complete with the relevant AE sensors. The geometry of the structure and the sensors in this model are constructed from points, which are defined in reference to a global coordinate system. Due to the nature of the coordinate system used, the propagation direction and propagation distance from any given point in the geometry to any of the sensors in the array can be determined using vector manipulation. Hence, with a known wave speed, the time of flight from and point in the geometry to any of the sensors in the array can be determined. Since the time of flight of a wave,

originating from geometric point, to each of the sensors is known, it is possible to calculate the difference in time of arrival, Δt, between every sensor pair combination for every geometric point in the model. These values are saved in an array and once live test data is recorded, the experimentally determined Δt values can be compared against those in the array to find the best match and thus location of the experimental source.

However, in order to simulate the times of flight, accurate wave propagation speeds must be determined for all propagation directions which can be time consuming. Furthermore, structures with very complex geometry can be more difficult to model; some structures can contain hidden features which will be left out of the model; and some structures might contain damage or manufacturing imperfections which it is very difficult to account for with a computational model.

#### *2.2.5.3 Delta-T Mapping Location*

*Delta-T mapping* is a novel source location technique developed by Baxter (2007) which is not overly dissimilar to the *best-matched point* method described in Section 2.2.5.2 other than in that the values of Δt between each of the sensor pairs for different points on the structure under investigation are obtained experimentally, from the specimen, as opposed to via a computational simulation. A detailed description of *delta-T mapping* is provided by Baxter (2007) though the main procedural steps are outlined below;

1. An area of interest on the structure under investigation should be defined. Whilst it is possible for *delta-T mapping* to provide source location over an entire structure, the technique requires the collection of data from the structure itself before testing takes place and so this can be unnecessarily time consuming if the entire area is considered. Instead, delta-T mapping should be thought of as a tool to improve location accuracy around pre-determined, damage susceptible areas.
2. A *training grid* is drawn on to the surface of the structure under investigation at the area(s) of interest defined. The spatial resolution of the training grid will have a bearing on the accuracy of the location calculation, however, note that in principle, it

should only be possible to locate to within one transducer diameter of the source. Since the training grid is used as the reference point during *delta-T mapping*, the AE sensors do not need to be placed within it and, in fact, other than to assist the user in understanding the data after testing, the positions of the AE sensors do not even need to be known at all.

3. The collection of data from the training grid can now take place, namely the determination of the arrival time of a wave, originating at any of the grid points, to each of the sensors in the array. This is done via the generation of artificial AE sources, in the form of Hsu-Nielson (H-N) pencil lead breaks, Section 3.1.4, at each of the training grid points. Several H-N sources are generated at each training grid point to remove erroneous data and provide an average value; generally five H-N sources is considered adequate for this purpose.
4. Using the time of arrival information, Δt values between each sensor pair combination can be obtained for every point in the training grid. For three sensors there will be three combinations, 1-2, 1-3 and 2-3; for four sensors there will be six combinations, 1-2, 1-3, 1-4, 2-3, 2-4, 3-4, and so on. The Δt values for each sensor pair, for every training grid point, are then saved in an array which acts as the Δt map for that sensor pair; one map is generated for each sensor pairing.
5. These Δt maps can then be used to locate real AE signals arising in the structure. The time of arrival of the AE signal at each of the sensors is used to calculate Δt values for each sensor pair. The Δt maps for each sensor pair can be used to identify a line of constant Δt on that map which corresponds to the Δt value obtained from the source, for that particular sensor pair. Theoretically, overlaying the lines of constant Δt from each of the Δt maps on to one another will show the convergence point and hence the location of the signal. However, due to slight errors at each stage of the process, it is not so clear cut in practice and often many convergence points are located instead. Thus a clustering technique is applied to the location of all the convergence points to determine the most likely location of the source.

The advantage of mapping the time of arrival data from the specimen itself is that any complex geometric features, unknown hidden features, and potential pre-existing regions of damage are accounted for. Research has shown that *delta-T mapping* can provide up to a 50% reduction in error (in terms of distance of located AE to location of known source) over conventional TOA location (Baxter 2007; Baxter et al. 2007; Eaton et al. 2012). Furthermore, the use of *delta-T mapping* does not require detailed velocity data of AE traveling in the specimen to be obtained. However, collecting the training grid data can be very time consuming for certain geometries and nature of manual execution of this task introduces the chances for human error; for instance, not generating the H-N source exactly on top of the grid point.

Pearson (2013) made an iterative improvement to *delta-T mapping* through the implementation of a two-stage AIC first arrival time *picker* at two steps of the process outlined above. Firstly during step 4, before calculating the values of Δt between sensor pairs, the AIC picker is used to determining more accurate first arrival times for the waveforms collected from the training grid. Secondly during step 5, before the values of Δt between sensor pairs are calculated from the waveforms captured from real AE data, the AIC picker is used to determine more accurate first arrival times for the real AE waveforms captured during the experimental testing/structural health monitoring. Pearson's amendment to the *delta-T mapping* technique was shown to provide improvements in accuracy when compared with its predecessor (Pearson 2013) and TOA location (Pearson 2013; Eaton et al. 2015), and is the form of *delta-T mapping* used within this thesis.

### 2.2.6 Characterisation

As well as detecting and locating signals arising in a structure, AE also has the potential to use information about a detected signal to determine the nature of the event which caused it; this is termed *characterisation*. An accurate and reliable characterisation method would be a welcome addition to an SHM system as it would allow the user to determine what kind of damage is developing in a structure and hence what kind of

maintenance or repairs are required. However, this goal has not yet been achieved and since its origin in 1971, with the work of Mehan and Mullin (1971) and Stephens and Pollock (1971), source characterisation has remained an active area of research.

As commented by Gutkin (2011), early and basic approaches have looked to classify signals based on a single AE feature. Both Valentin et al (1983) and Kotsikos et al (1999) have used the amplitude of recorded AE to distinguish between damage mechanisms; including matrix cracking, delamination and fibre fracture; occurring in fibre reinforced composites. However, as highlighted by Prosser et al (1995), due to signal attenuation, a single source may result in recorded signals with several different amplitudes, depending on the distance of the recording sensor from the source, and so signal amplitude can only provide limited information about the nature of an AE source.

To overcome the limited resolution inherent when attempting to characterise AE using a single feature, studies began to consider multiple AE features to see if a firmer correlation between source mechanism and the AE characteristics could be obtained. Ono et al (1989) used correlation plots of signal amplitude versus signal duration in an attempt to distinguish between damage mechanisms occurring in carbon fibre-peek composite, however many of the distributions overlapped and so clear discrimination between each mechanism was not achieved. Pattern recognition techniques, such as those developed by Sause et al (2012) and Crivelli et al (2014), go one step further by simultaneously analysing numerous AE features to identify clusters, or groups, of AE signals which share several similar AE feature values. The location and times of occurrence of the AE in each of the clusters can then be investigated to determine whether they correspond to the occurrence of damage in the specimen and hence certain damage mechanisms can be said to be characterised by AE with a certain range of features. Whilst pattern recognition techniques are far more robust then single feature characterisation, they still share a similar weakness; signal propagation effects. The amplitude of an AE signal is not the only feature affected by the attenuation and dispersion of that signal during its propagation from the source to the recording sensor; other features typically used in

pattern recognition techniques, such as duration, rise time and counts, also change. Thus a single AE source can result in recorded signals with differences in several features depending on the positons of the recording sensors. This effect is more severe in real-life structures which typically contain many complex geometric features to disrupt wave propagation; furthermore industrial applications of AE are more likely to adopt a larger sensor spacing to save on cost or weight, thus leading to larger propagation distances over which a signal can change more.

As the ability of AE acquisition systems to reliably capture waveforms at higher recording frequencies improved, researchers gained the ability to investigate the frequency content of the captured waves in more detail and subsequently frequency based characterisation approaches gained momentum. In flat plates, where AE wave are bounded by the surfaces and travel as Lamb waves, Gorman and Prosser (1991) noticed a connection between the orientation of the source and the amplitude of the two Lamb wave modes. They found that artificial signals produced at angles of 0 and 30 degrees with respect to the plane of an aluminium plate resulted in signals with larger amplitude $S_o$ Lamb wave mode whereas artificial signals produced at angles of 60 and 90 degrees with respect to the plane of the plate produced signals with larger $A_o$ Lamb wave mode. Since then, the relationship between source mechanism orientation and the relative amplitudes of the two Lamb wave modes has been explored, with Prosser (1996), Surgeon and Wevers (1999), Pullin et al (2005) and Eaton (2007; Eaton et al. 2011) all yielding successful source characterisation results. An analysis which utilises information about the AE wave modes traveling in a structure is reffered to as a *modal analysis*, and a modal analysis in which the relative amplitudes of the two Lamb wave modes are compared is referred to as *Measured Amplitude Ratio* (MAR).

Ultimately though, the feature altering issue of signal propagation is still present, even for frequency based modal techniques. Since the higher frequency $S_o$ Lamb wave mode has been shown to attenuate at a faster rate than the $A_o$ Lamb wave mode (Sause et al. 2012; Eaton 2007), a single source might be recorded as having one MAR value by a

sensor in one position and another MAR value by a sensor in another position. The matter of overcoming signal attenuation and other propagation effects is one of the largest challenges facing the development of reliable and robust AE characterisation techniques today.

# 3 Experimental Instrumentation and Techniques

## 3.1 Acoustic Emission

### 3.1.1 Data acquisition and timing parameters

The AE acquisition system used during this research was a PCI-2 system, which was manufactured by Physical Acoustics Ltd, a trademark of MISTRAS. The PCI-2 system is essentially a PC which incorporates four PCI-2 boards, each of which comprise of two low-noise AE channels, Figure 3.1, and so has a total of 8 useable AE channels. Each channel can perform 18bit A/D conversion at 40MHz and thus provide high resolution data collection. PCI-2 boards have a wide bandwidth, 1kHz to 3MHz, which means that it is possible for the boards to be used in conjunction with any of the currently available MISTRAS AE sensors. They allow waveform acquisition and feature extraction through the incorporation of a digital signal processing (DSP) system and incorporate programmable frequency filters (Physical Acoustics Corporation 2003). The PCI-2 system is also capable of continuous data recording which allows the user to continuously record waveforms directly to the hard drive at a combined maximum rate of 10MHz, e.g. 5MHz/channel on two channels, or 2.5MHz/channel on four channels, etc. Finally, the PCI-2 system can record up to eight parametric channels at up to 10KHz, thus during typical research testing conditions it is capable of logging the load and displacement from the actuator.

The acquisition set up, i.e., selecting which AE features to record, recording rates and thresholds etc, is controlled through Physical Acoustic's 'AEWin' software and all data selected for recording is saved to the PCs hard drive. An important consideration when deciding on the acquisition setup for a particular AE application is the selection of timing parameters; the Hit Definition Time (HDT), Hit Lockout Time (HLT) and Peak Definition Time (PDT).

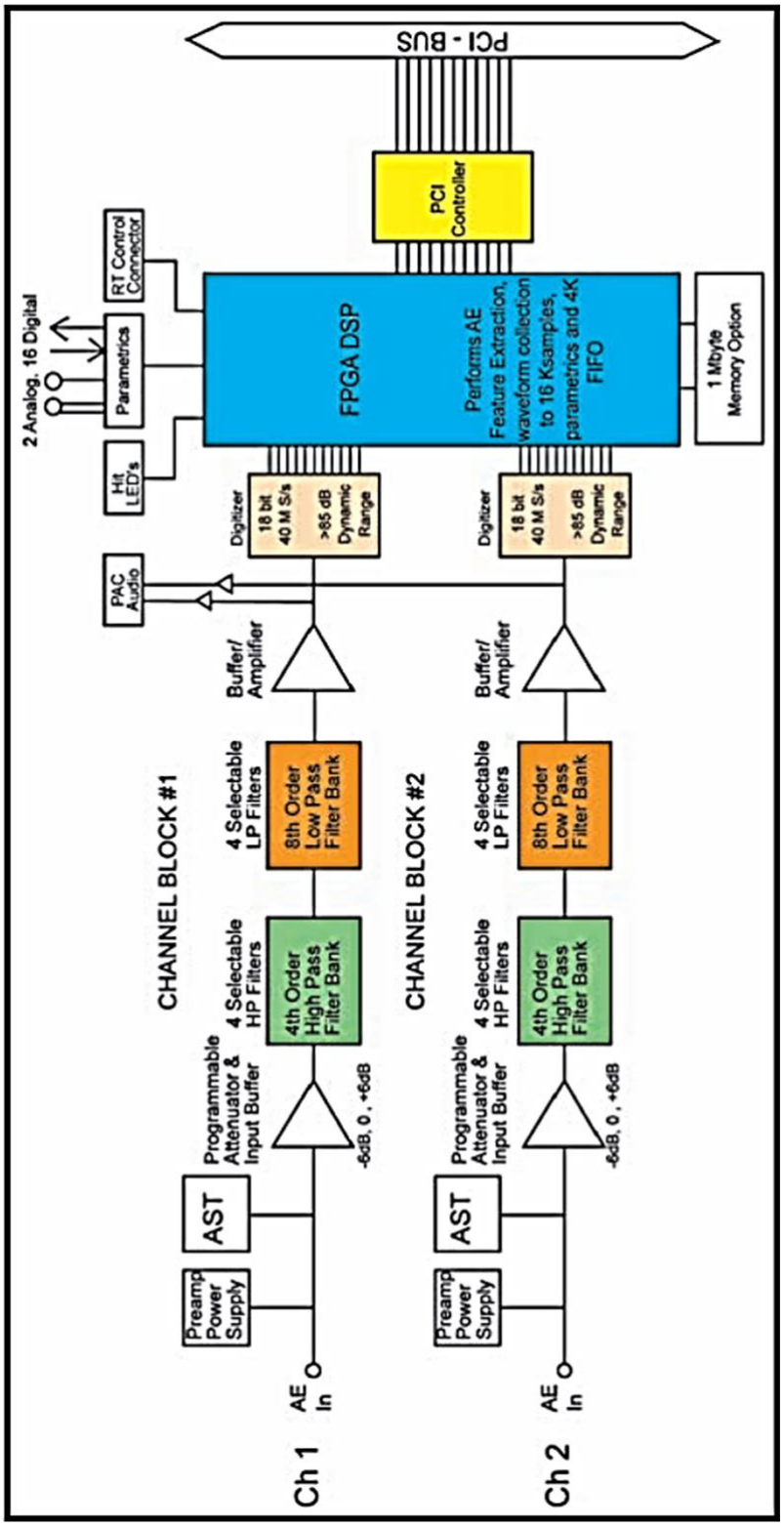


*Figure 3.1: PCI-2 AE System block diagram, figure reproduced from MISTRAS* (2009)

The HDT defines the length of time that the acquisition system will wait for in order to determine the end of a hit; this is perhaps explained best through the use of an example. During hit based AE testing each sensor continuously monitors the surface vibrations of

the structure under investigation; once the amplitude of the signal caused by those surface vibrations crosses the user defined threshold on a particular sensor, the acquisition system begins to record the signal received by that sensor. During the process of recording the incoming signal (or hit), the acquisition system also performs an analysis of that signal by tracking its amplitude. Each time the signal's amplitude drops below the user defined threshold, the HDT timer is started. If the signal's amplitude surpasses the threshold again before the duration of the HDT then the HDT timer is reset. This process continues until the signal amplitude drops below the threshold for a duration of time longer than the HDT, at which point the incoming signal ceases to be recorded; the signal that was recorded up until that point is saved to the computer's hard drive as a waveform; and any AE feature data selected to be recorded, such as the peak amplitude, rise time and duration, is saved for that hit. If too small a HDT is used then the entirety of a single wave may not be recorded as one hit, and instead might be recorded as multiple hits, Figure 3.2. Conversely, if too large a HDT is used then multiple waves which arrive within a short space of time of one another could be recorded together as a single hit, instead of multiple hits.

Once a hit has been recorded, the recording sensor is temporarily deactivated; the HLT defines the length of time that the acquisition system will wait for before re-arming a sensor to record again. If too short a HLT is used then late arriving reflections might retrigger the sensor to record again; this would lead the end user to think that there had been two AE events generating stress waves when in fact there had been just one, Figure 3.3. Conversely, if too large a HLT is defined then the system might fail to record the stress wave released by a second AE event which occurs shortly after the first; this would lead the end user to think that there had been just one AE event when in fact there had been two.

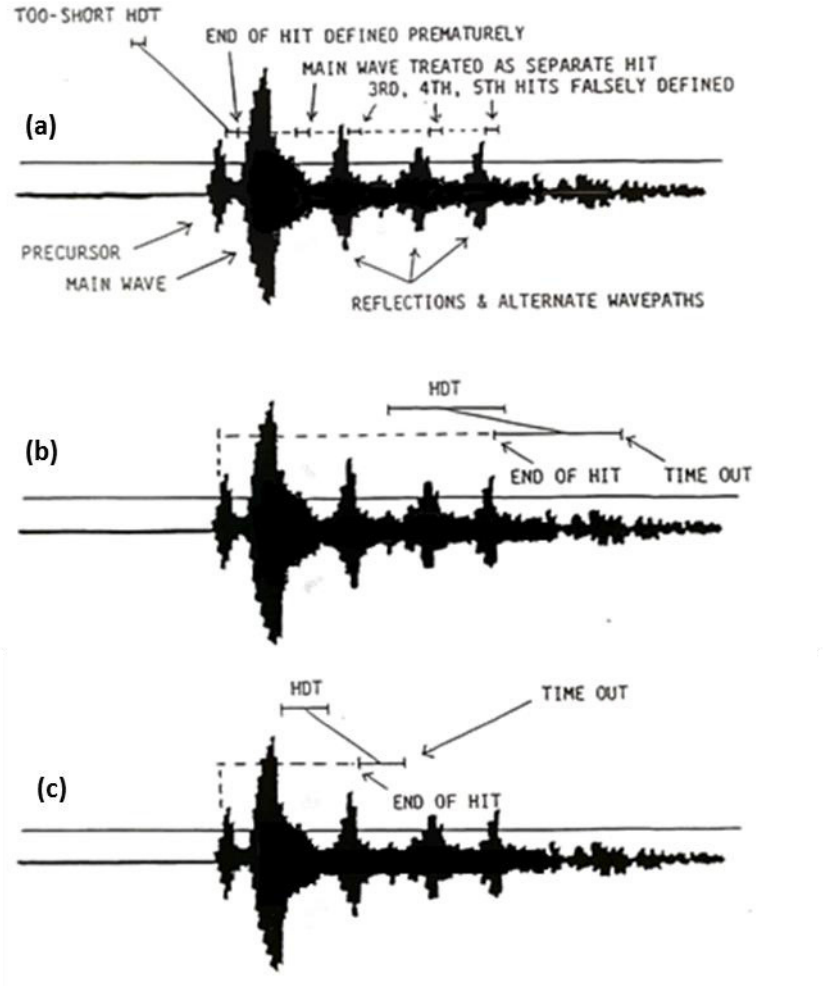


*Figure 3.2: Example of different HDTs and their effect on the manner in which a hit is recorded for (a) a HDT which is too short, (b) a HDT which allows the entire wave and reflections/alternate wavepaths to be recorded, and (c) a HDT which allows only the main wave and limited number of reflections to be recorded, figure recreated from Physical Acoustics Corporation* (2004)

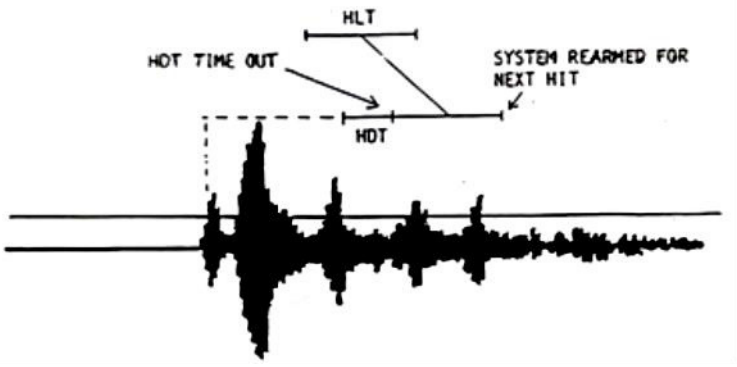


*Figure 3.3: Example of HLT which disarms the sensor for a length of time which prohibits the two late arriving reflections from being recorded as new hits, figure reproduced from Physical Acoustics Corporation* (2004)

Finally, the PDT defines the length of time that the acquisition system will wait for in order to determine the peak amplitude of a hit. Initially, in the instance that the signal first crosses the threshold, the peak amplitude is simply the maximum amplitude that was reached by the wave during the threshold crossing. The acquisition system will then wait for the length of time designated by the PDT before logging and saving that peak amplitude value as the peak amplitude for the hit. However, if during this waiting time the signal reaches a greater amplitude than the previous peak amplitude then the PDT timer will reset, and the acquisition system will begin to wait again. This process continues until the recorded signal does not surpass the current peak amplitude within the PDT waiting period, at which point the value of the peak amplitude is logged and saved for the hit. If too small a PDT is used then the peak amplitude of the main wave will be missed, Figure 3.4. Conversely, if too large a PDT is used then there is the potential that the amplitude of superpositioned reflections is identified as the peak amplitude.

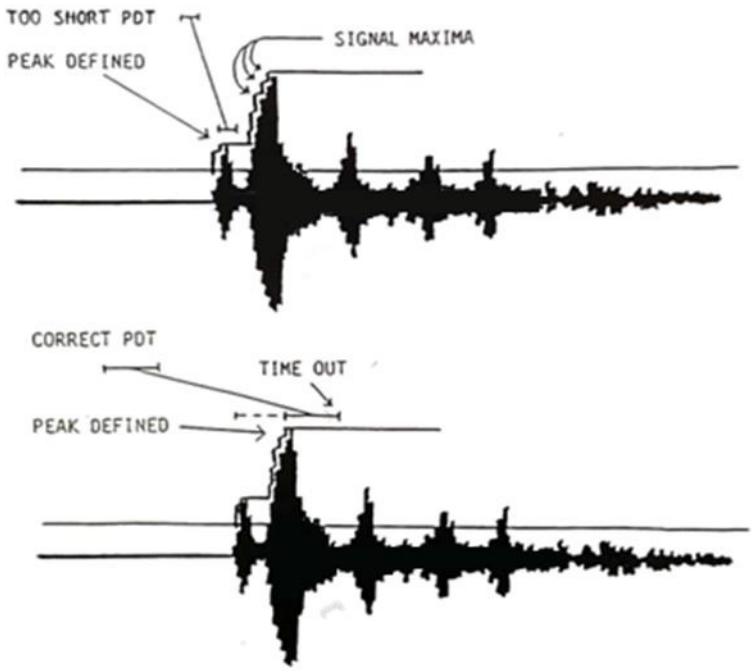


*Figure 3.4: Examples of different PDTs and their effect of the identification of the peak amplitude of the hit for (a) a short PDT which causes the main wave amplitude to be missed, and (b) a PDT which allows the main wave amplitude to be logged as the peak amplitude, figure recreated from Physical Acoustic Corporation* (2004)

AEWin also allows the user to apply additional controls to limit which hits are recorded, through the use of Front End Filters. A Front End Filter is effectively a 'rule' that can be applied to one, a number, or all of the recording sensors, which prohibit them from recording a hit if one of the AE features of that hit is outside a user specified limit. For example, a Front End Filter can be used to prohibit a hit from being recorded by a particular sensor if the peak amplitude of that hit is larger, or smaller, than a user defined limit.

Front End Filters are particularly useful when collecting the grid data required for the delta-T mapping technique. Whilst collecting the grid data, it is necessary for each sensor to record just a single hit from each artificially generated H-N source. However, it can often be the case that generating a single H-N source results in a number of sensor observing reflections that are of sufficient amplitude to trigger the collection of multiple hits on that sensor. Through experimentation, the largest peak amplitude of the reflections can be determined; a Front End Filter can then be applied to sensors to prohibit them from recording hits that have a peak amplitude lower than that value, and thus prohibit them from recording hits from reflections. It should be noted that this is different from simply changing the threshold (the threshold above which the acquisition system will trigger a hit to be recorded), since changing the threshold would cause sensors to be triggered from different parts of the propagating wave, and hence the arrival times logged for each hit would not accurately represent of the first arrival of the wave at the recording sensor.

### 3.1.2 Transducers

Piezoelectric transducers are the devices used in AE monitoring to convert the surface displacements generated by elastic waves into an electrical signal for processing by the measuring equipment. As their name suggests, piezoelectric transducers use the piezoelectric effect in order to produce electricity from mechanical excitation; Figure 3.5 shows the typical architecture of an AE sensor with the piezoelectric crystal/element inside. As shown in Figure 3.6, a piezoelectric crystal is one which does not have central

symmetry in its charge, which means that when it undergoes deformation in a particular direction it becomes polarised and hence generates and electrical field (Arnau 2004). Typically, within an AE sensor this piezoelectric element has an electrode on each face, one which is grounded and one which acts as the signal lead, and sits against the wear plate. Above the piezoelectric element is a damping material which acts to minimise reflections and also suppress some of the piezo's natural resonance (Elman & Muravin 2011).

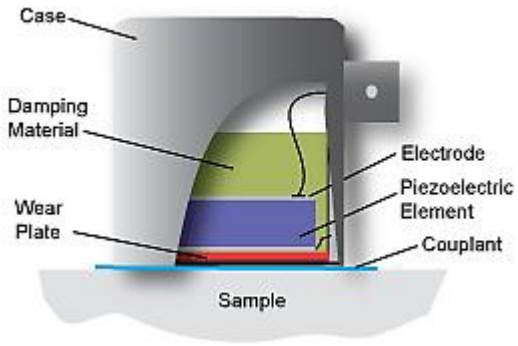


*Figure 3.5: Typical AE sensor architecture, figure reproduced from NDT Resource Centre* (n.d.)

Since their purpose is to detect ultrasonic surface waves, AE sensors typically operate over the range of 20kHz-1MHz, though the frequency response of any individual sensor is a function of a number of things; notably the piezo-element's physical dimensions and the level of damping. A piezoelectric element's resonant frequency is inversely proportional to its thickness (Ferrari & Lucklum 2008) whereas an element's diameter dictates the area over which the surface motion is averaged. Damping acts to supress the piezo-element's resonance and produces a less biased frequency response. There are many types of piezoelectric sensor produced for use in a range of industries but they can broadly be broken down into two main categories; sensors which are highly resonant to particular frequencies or sensors which offer a more broadband response.

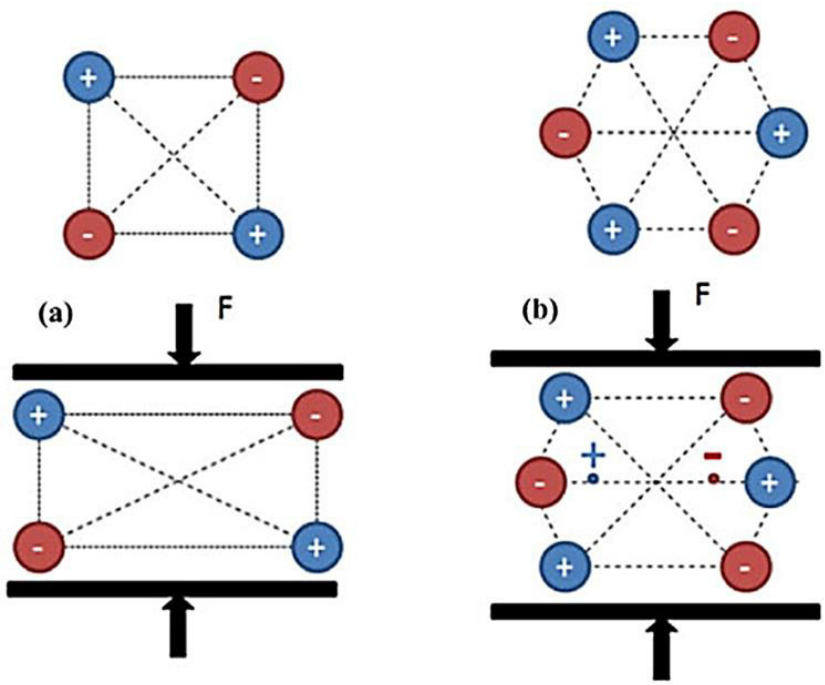


*Figure 3.6: Examples of 2D crystal structures; (a) non-piezoelectric square which exhibits no polarisation change under the applied force and (b) piezoelectric hexagon which exhibits polarisation under the applied load, figures reproduced from Ramadan et al (2014)*

Resonant sensors produce a greater amplitude electrical output signal for input signals with frequencies which are close to the sensor's resonant frequency. Figure 3.7 gives an example of the calibration chart for an R30S sensor produced by MISTRAS. The sensor has a resonant frequency of 360KHz and so input signals at this frequency will produce disproportionately larger voltage than input signals of other frequencies; because of this, resonant sensors should only be used if the frequency content of the AE signal itself is of no interest. Analyses using AE features such as amplitude, arrival time or energy can be performed using the data collected from resonant sensors, however ultimately, since these features have a dependency on the frequency response of the recording sensor, only data collected from similar sensors should be compared. Due to their nature, resonant sensors also have frequency bands where their response is very low and thus consideration should be paid to this when choosing which sensor to utilise in a given situation. Despite these considerations, resonant sensors are typically more sensitive than their broadband sensor counterparts and, since in most practical applications the

frequency bands of interest are known, remain the most commonly used (Vallen Systems 2012).

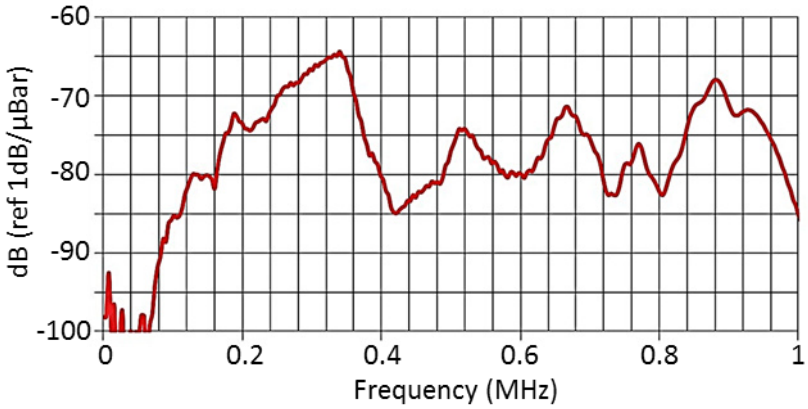


*Figure 3.7: Calibration Chart for MISTRAS' R30S - 300 kHz AE Sensor, figure reproduced from MISTRAS* (2011a)

Broadband sensors, also referred to as wideband sensors, offer a flatter frequency response with fewer and less pronounced resonant frequency peaks. They are typically produced by increasing the level of damping on the piezoelectric element which acts to lower the amplitude of resonant frequencies. However, this also leads to a reduction in their sensitivity and thus wideband sensors find less application outside the research environment than resonant sensors. The merit of broadband sensors is that they give a more accurate representation of the surface displacement caused by an AE source which makes them useful tools for quantitative frequency or modal analysis. Figure 3.8 shows an example calibration chart for a wideband sensor and demonstrates the flat frequency response which is in direct contrast to that of the resonant sensor in Figure 3.7. As well as resonant and wideband varieties, AE sensors also come in single ended and differential variants. Single ended sensors have just one piezoelectric element and operate as described above. Differential sensors contain two piezoelectric elements which have opposite polarisation directions and so excitation signals cause them to produce two equal magnitude yet opposite sign outputs, which if summed would cancel each other out. These two signal outputs are fed to a differential preamplifier which eliminates common-mode noise resulting in up to 2dB lower noise output (MISTRAS 2011b).

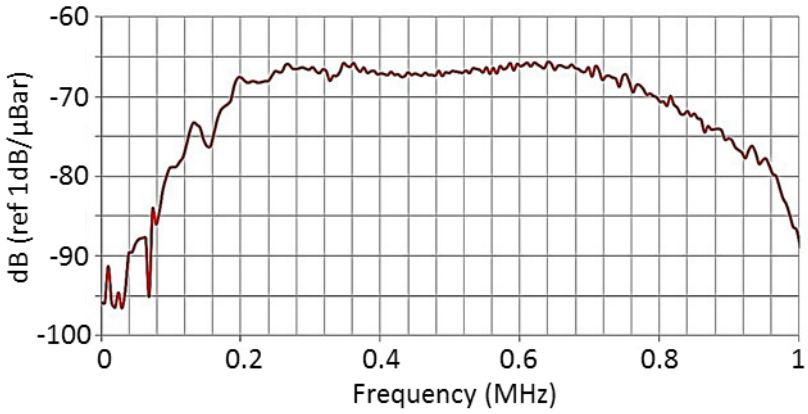


*Figure 3.8: Calibration Chart for MISTRAS' F50a - 200-800 kHz High-Sensitivity Flat Frequency Response AE Sensor, figure reproduced from MISTRAS* (2013)

Two types of sensor were used in this work, Nano30 and WD, both manufactured by MISTRAS Group and the details of their characteristics, as rated by the manufacturer in accordance with ASTM E1106 (ASTM 1986), are presented in Table 3.1. The manufacturer's data sheets for each sensor can be found in the Appendix A and examples of each of their calibration certificates, produced by the manufacturer in accordance with ASTM E976 (ASTM 1984), can be seen in Figure 3.9. The Nano30 is a resonant, single ended sensor with a resonant frequency of approximately 300kHz though it should be noted that, as far as resonant sensors are concerned, the Nano30 offers a relatively wideband response. The WD sensor is a wideband, differential sensor which provides a flat frequency response whilst maintaining reasonable sensitivity.

*Table 3.1: Manufacturer's specification of AE sensors used during this thesis*

| Sensor | Dimensions (mm) Diameter x Height | Operating Frequency Range (kHz) | Resonant Frequency (kHz) (shear[compression]) | Differential? |
|---|---|---|---|---|
| Nano30 | 8 x 8 | 125 – 750 | 140 [300] | No |
| WD | 18 x 17 | 100 – 1000 | 125[450] | Yes |

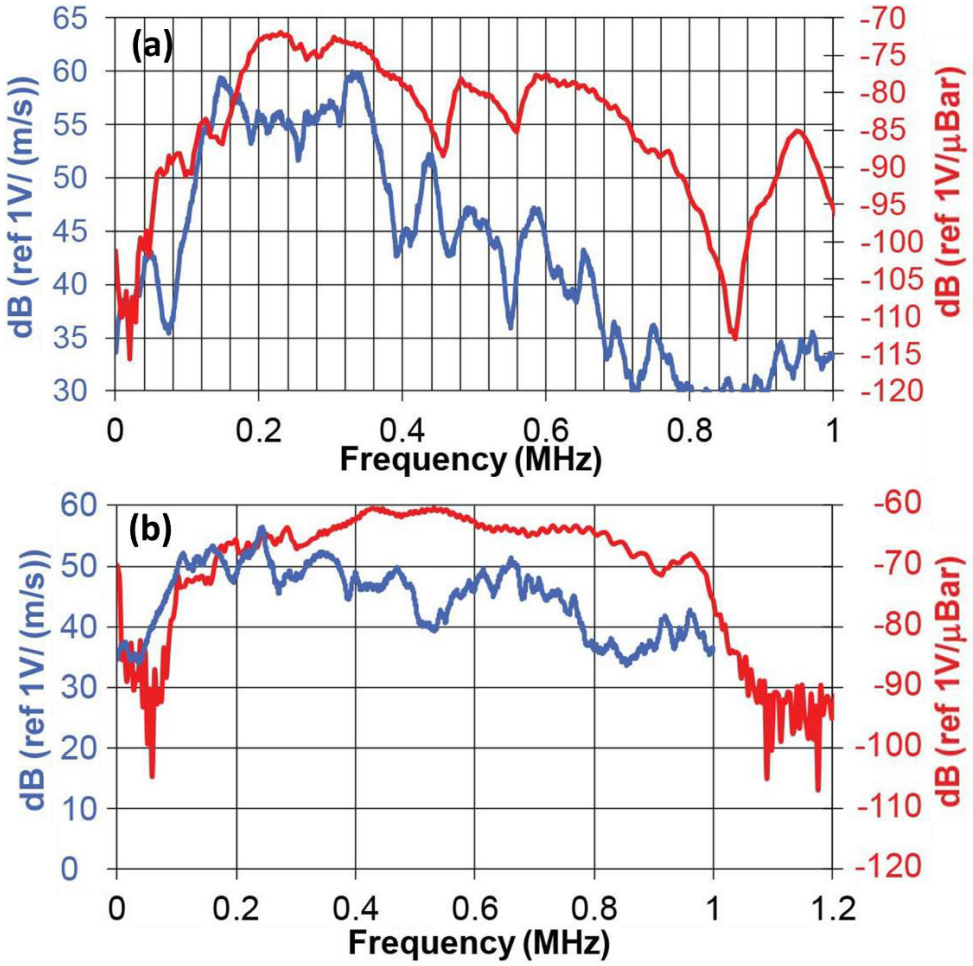


*Figure 3.9: Manufacturer's calibration certificates for (a) Nano30 and (b) WD AE sensors, using both the shear (blue line) and compressional (red line) calibration methods*

### 3.1.3 Sensor Mounting

Achieving a good acoustic coupling between the AE sensor and the surface to which it is attached is paramount to successfully detecting as much AE activity as possible, since a poor coupling reduces the sensitivity of the recording sensor which might result in low amplitude activity going undetected. Operating sensors with a poor coupling may also result in unreproducible AE detection and a low fidelity recording of the surface's displacement, and hence lead to the determination of unrepresentative AE signal features such as amplitude, rise time and duration. These consequences could mislead the end user of an AE-centric SHM system to believe that the severity of damage in a monitored structure is less than it actually is and therefore, having a means of consistently adequately mounting AE sensors is vital to the success of AE as a

technique. To mount an AE sensor effectively to the surface of a structure, two main parameters must be satisfied;

1. The sensor must be physically restrained to the surface using a clamping method.
2. The sensor must be acoustically coupled to the surface.

#### *3.1.3.1 Clamping Methods*

The purpose of clamping is to bring the AE sensor into close contact with the surface and maintain an adequate and constant acoustic coupling between the sensor and the structure. The clamping method used should satisfy this requirement without creating any AE of its own, due to friction or the movement of lose component parts, nor should it disrupt any of the AE generated in the structure under investigation. According to ASTM 650 (ASTM 1998), for an AE sensor to be adequately physically restrained to a surface there must be sufficient pressure that the surface and sensor do not move relative to one another. This pressure should also be applied constantly to ensure that there is an intimate contact between the sensor and the surface throughout the entirety of the testing period in order for AE occurring at any time to be transferred directly to the sensor. There are two main methods of mounting sensors; through the use of compression mounts or through the use of adhesion. Compression mounts use force to hold the sensor against the surface and typical, well-tested, clamping methods include;

*Electrical tape* – Adhering electrical tape to the surface of the structure and stretching it over the top of a sensor can provide the appropriate mounting pressure, as shown in Figure 3.10.

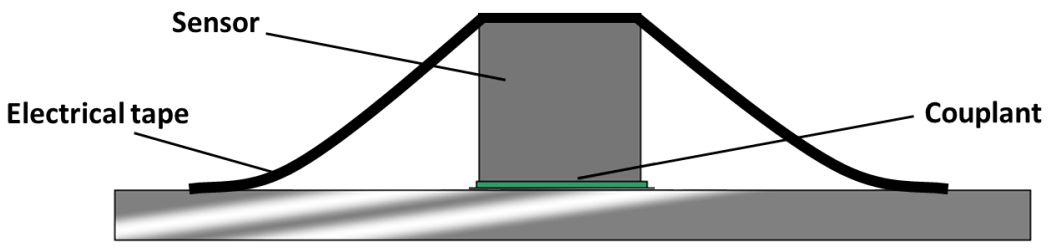


*Figure 3.10: Electrical tape mounting schematic*

*Aluminium 'hat' clamps* – 'Top hat' shaped aluminium clamps are often used to mount sensors on concrete structures. The mounting pressure comes from the screws which can be tightened to increase the pressure accordingly, as shown in Figure 3.11, however, this method requires the structure to be permanently modified in order to accommodate the mounting screws.

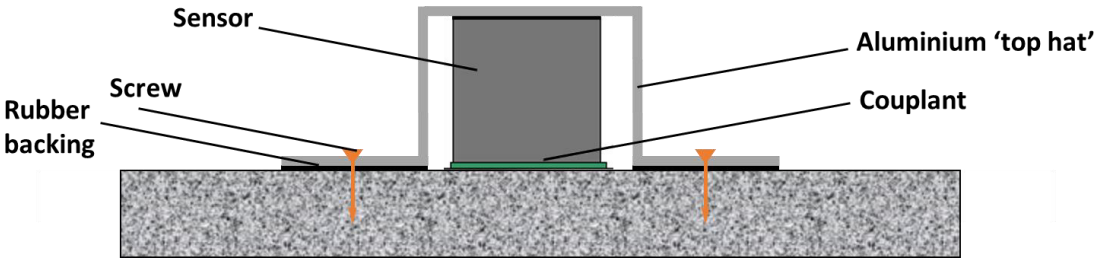


*Figure 3.11: Aluminium 'top hat' mounting schematic*

*Magnetic clamps* – Two varieties of magnetic clamps are commonly used, small and large, and depending on the material under inspection, must be used in different ways. For the large magnetic clamp, which was designed by PAC, the magnets supply the holding force to the surface and the spring loaded end-plate provides the mounting pressure on the sensor. The smaller magnet clamps, which were proposed for use on smaller, more difficult to handle AE sensors by Baxter (2007), use a foam tab to transfer the holding magnetic force into a mounting pressure on the sensor, Figure 3.12. When nonmagnetic materials, such as carbon fibre composites are used, the magnetic clamps can still be used, albeit in a modified way. Steel tabs must be bonded to the surface of the specimen or a second magnet must be positioned on the opposite side of the specimen in order to offer the primary magnet with a means of providing a clamping force to the surface, Figure 3.13.

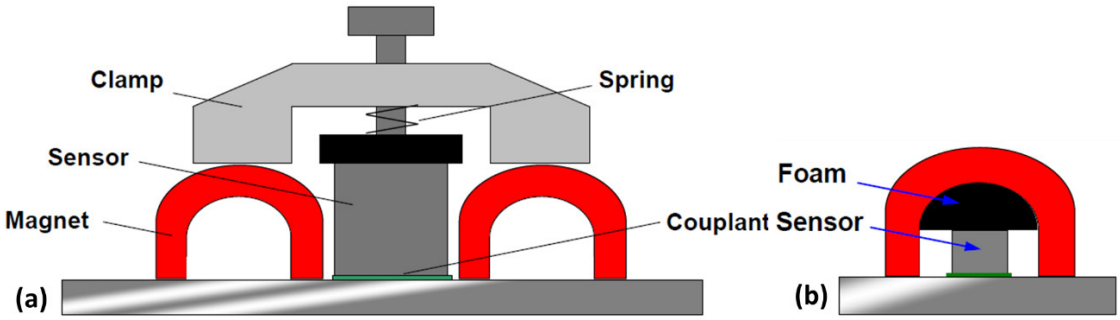


*Figure 3.12: Magnetic clamp mounting schematic for ferromagnetic structure (a) for large sensor and (b) for small sensor* (Eaton 2007)

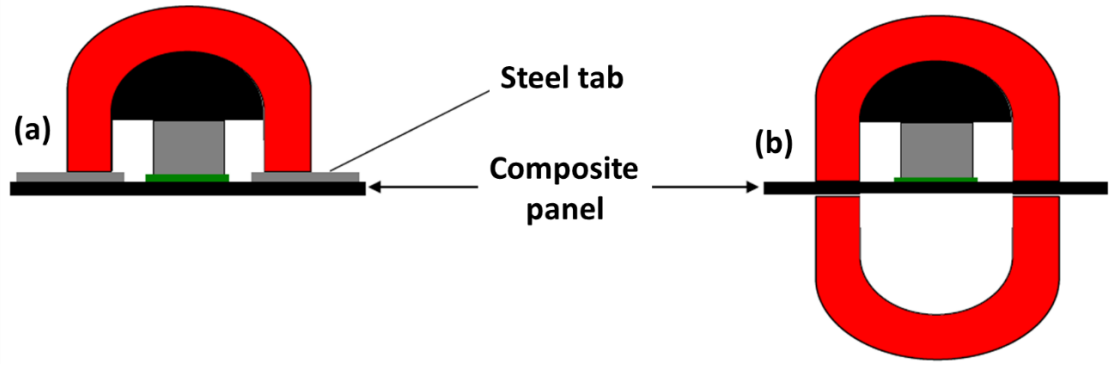


*Figure 3.13: Magnetic clamp schematic for nonmagnetic structure using (a) steel tabs and (b) two magnets* (Eaton 2007)

*Self-adhesive tabs with cable ties* – Similar to the electrical tape method, adhesive tabs can be bonded to the structures surface either side of a sensor and used to support a cable tie. Looping the cable tie over the top of the sensor and tightening it provides the mounting pressure.

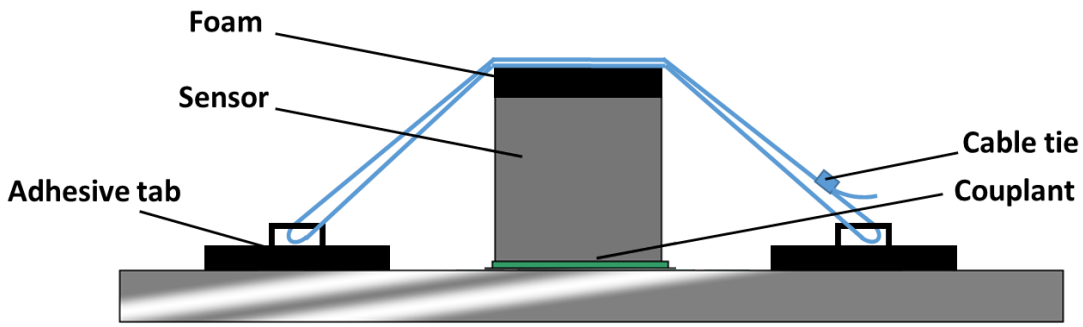


*Figure 3.14: Self-adhesive tab and cable tie mounting schematic*

Finally, it is possible to bond a sensor to a structure using an adhesive such as cyanoacrylate or silicone sealant. When a sensor is mounted in this way pressure must be applied to the sensor whilst the adhesive is curing so that once it is set, the sensor face is in close contact to the structure's surface. Bonding sensors is a good solution for structures with geometrical obstructions which make mounted methods impractical. Bonding sensors also results in a more permanent fixation, so is a preferred method of sensor mounting for longer duration testing. However, certain adhesives can cause damage to the sensor and the specimen's surface when they are removed and, due to the curing time, bonding sensors results in a longer experimental setup time. It should be noted that, whilst the use of an acoustic couplant is highly recommended for compression mounted sensors, the adhesive itself acts as the couplant when sensors are bonded to a surface and so additional acoustic couplant is not needed in this instance.

#### *3.1.3.2 Acoustic Couplants*

Acoustic couplants are used in order to maximise the transmission of acoustic energy from the structure to the sensor by removing the presence of air, which has a low acoustic impedance, from between the sensor face and surface and replacing it with the couplant, which has a higher acoustic impedance. Much like the clamping methods described in Section 3.1.3.1, there is no *one-size-fits-all* acoustic couplant for every scenario and the selection of a couplant is based on the AE monitoring application at hand. A number of considerations when deciding the suitability of a couplant for a AE monitoring purposes are highlighted by Theobald (2012);

- How long will the measurement take?
- Is long-term stability important?
- How often is the sensor removed?
- Could the sensor be permanently bonded?
- Is there any source of movement or vibration which could displace the sensor?

- What are the environmental conditions i.e. temperature, humidity?
- Could the couplant react with the measurement surface or cause corrosion?
- What type of wave is being measured? (Is good in-plane displacement transmission required?)

The ASTM 650, Standard Guide for Mounting Piezoelectric Acoustic Emission Sensors, (ASTM 1998) highlights several acoustic couplants which should be considered. Liquid couplants, such as propylene glycol, have a lower acoustic impedance than other commonly used couplants (Baxter 2007), however, they are very easy to clean from the structure after use. Their low viscosity increases the ease with which they can force air out from between the contact but also causes them to dip and/or dry out rapidly so they are not suitable for use on tests which are intended to last longer than a couple of hours or for coupling sensors to vertical faces. Liquid-based gels such as ultrasound gel and glycerine offer a slightly higher viscosity than straight-liquid couplants which makes them more appropriate for use on rougher and even vertical surfaces. They offer a higher acoustic impedance that liquid couplants whilst retaining the ability to be easily removed from the surface after testing, however, they are still prone to drying out after several hours of use. Grease couplants offer a higher viscosity again and so are unlikely to dry out and offer better long term stability than liquids and gels, making them the most popular general purpose couplant for AE monitoring. The higher viscosity does mean that a higher application force is needed to remove the air from between the contact. Greases are also marginally more difficult to remove from the surface after testing. Dry couplants, such as elastomers, were developed to overcome the aforementioned issues associated to liquid based couplants and are available in a wide variety of acoustic impedances, though since they generally offer a lower acoustic impedance than greases, gels and liquids they are less popular for AE monitoring.

The majority of AE sensors have a dominant response in the direction normal to the structure's surface, however, if a larger sensitivity to the in-plane motion of the surface is desired then a more viscous couplant or rigid bond should be used.

Once an appropriate couplant has been chosen the contacting surfaces should be prepared and cleaned before its application. Again, and keeping in line with the common theme of this section, this cleaning is done in order to enhance the capability of the sensor to detect acoustic waves in the structure, by removing any grit or obstructions which could act to separate the sensor and surface slightly and reduce their acoustic impedance. A commonly used cleaning agent, and the one used in this study, is acetone solvent (Theobald 2012). It may also be necessary to consider additional forms of surface preparation. Loose paint might trap air pockets that separate the structure's surface and the sensor and would act to severely limit the acoustic transmission. Similarly, encapsulants, loose mill scale, weld spatter and oxides should be considered and removed or avoided as appropriate.

There are some rare incidents where the use of a couplant is impractical, such as high temperature conditions or surfaces which require extreme cleanliness. When this is the case, the AE sensor can be 'dry coupled' to the surface by applying a large enough holding pressure. The magnitude of the pressure required cannot be known definitely in advance and should be determined experimentally, however ASTM 650 recommends a minimum of 0.7MPa (ASTM 1998).

Once mounted the sensor must be tested to determine whether or not the attachment has a sufficient transfer of energy from the structure to the surface. This sensor calibration test can be performed using an H-N source.

### 3.1.4 H-N source

As discussed in section 3.1.4, correct sensor mounting is paramount to the success of AE as a technique, and so the determination of whether or not a sensor has been adequately mounted to a surface is also of vital importance. Realising this, Hsu and Breckenridge (1981) and Nielson (1980) investigated the applicability of various AE sources for the purpose of AE sensor calibration; their work highlighted the practicality of utilising a pencil lead break (PLB) for this purpose. A PLB source is generated by

pressing a pencil lead tip on to a surface which causes that surface to displace. As the force is increased the pencil lead breaks and the accumulated stress in the surface is released causing a rapid displacement of the surface and hence the release of an acoustic wave. The technique quickly gained popularity due to its repeatability and accessibility, and was dubbed the Hsu-Neilson (H-N) technique.

The standard procedure for generating an H-N source as agreed to by the European Working Group on Acoustic Emission (EWGAE) in October 1980 and later in ASTM E976 (ASTM 1984) consists of the following steps, Figure 3.15;

1. The lead feed button on the pencil is pressed repeatedly until the lead protrudes.
2. The end of the lead is levelled with the end of the guide tube by pressing the tip of the pencil perpendicularly towards an even surface while the feed button is pressed down.
3. The button is pressed six times causing the lead to protrude 3 mm.
4. The pencil is guided obliquely towards the structure until the guide ring rests on the surface.
5. The pencil is pivoted about the point of contact towards a steeper position thus causing the lead to break.

If carried out in this manner, an H-N source generated at a distance of 25mm from the central axis of a correctly mounted and acoustically coupled resonant AE sensor will produce AE with an amplitude of 97 to 100dB (a broadband sensor might typically record a slightly reduced amplitude signal on account of its lower sensitivity). Hence, by generating H-N sources adjacent to an AE sensor it can be determined whether or not that sensor is mounted correctly. This was the method used throughout this study to ensure correct sensor mounting; any sensor producing an unsatisfactory response (i.e. hits with amplitudes below 97dB) to the H-N source was removed and re-mounted until correct attachment was achieved.

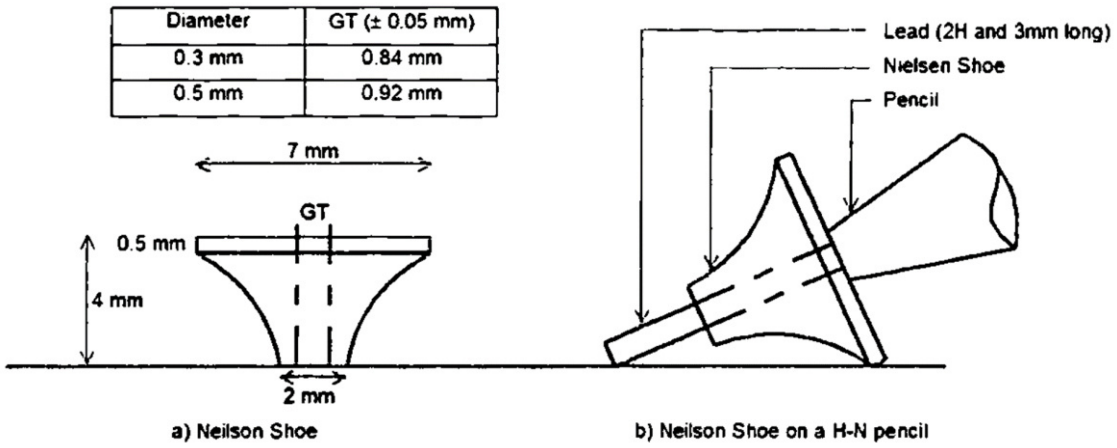


*Figure 3.15: Generation of an H-N source, figure reproduced from ASTM* (1984)

### 3.1.5 Velocity Measurement

There are numerous occasions where knowledge of the velocity of AE traveling in a particular medium might be needed, for instance during the calculation of the location of AE signals using the TOA or SSMAL techniques. It is also desirable to obtain the AE velocity purely from the perspective of curiosity or interest, as it assists in developing an overall understanding of the manner in which AE waves propagate in the medium in question, especially if the velocity of multiple wave modes are investigated. In order to experimentally determine the velocity of AE waves when traveling in a flat plate, i.e. for both the $S_o$ and $A_o$ Lamb wave mode, the following procedure can be followed;

1. Position two AE sensors at a set distance apart on the surface of the specimen. Each sensor should be adequately attached and coupled to the surface, and connected to the appropriate acquisition hardware.
2. Whilst recording AE hits, an H-N source should be generated adjacent to one of the sensors, in line with both channels, as shown in Figure 3.16. The H-N source should be generated at a distance from the first recording sensor which is greater than ten times the thickness of the plate specimen, in order to ensure that Lamb waves have enough distance over which to develop.
3. The hits recorded by each of the sensors will have acquisition times associated with them by the acquisition system. By investigating the waveform of each of the

hits in closer detail, Figure 3.17, the time of arrival of each of the wave modes within each hit can be determined. By adding the time of arrival of one of the wave modes within the waveform to the acquisition time of that hit, the absolute arrival time of that wave mode can be calculated.

4. The velocity of either of the wave modes can then be calculated using Equation 3-1;

$$C_{S/A} = \frac{T_{CH2\ S/A} - T_{CH1\ S/A}}{d_2}$$

*Equation 3-1*

Where; $C_{S/A}$ = the velocity of the $S_o$ or $A_o$ wave mode

$T_{CH1\ S/A}$ = the absolute arrival time of the $S_o$ or $A_o$ wave mode at channel 1

$T_{CH2\ S/A}$ = the absolute arrival time of the $S_o$ or $A_o$ wave mode at channel 2

$d_2$ = the distance between CH1 and CH2

It is important to note that this process gives you solely the velocity of each of the wave modes for the particular material tested and in the orientation tested. In orthotropic materials such as composites, where AE velocity has been demonstrated to exhibit directional variability (Lopresto 2009), this measurement should be performed for multiple propagation directions in order to build up a more comprehensive understanding of the propagation behaviour.

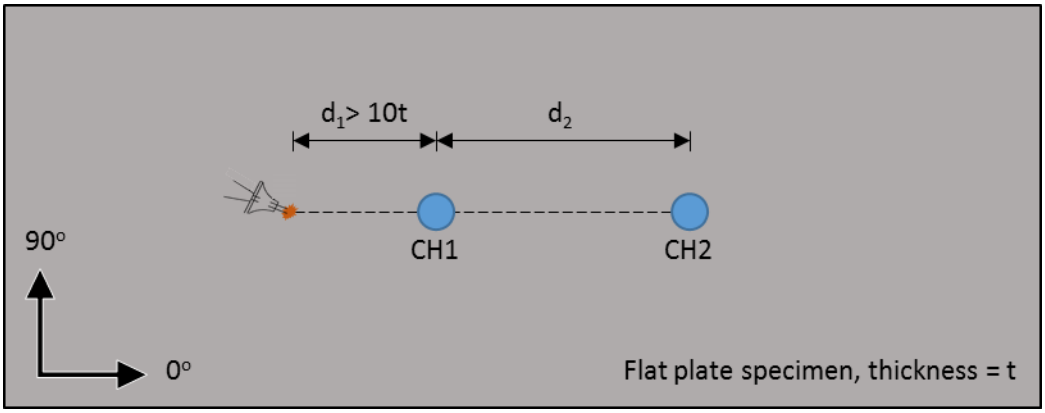


*Figure 3.16: AE velocity test sensor positioning*

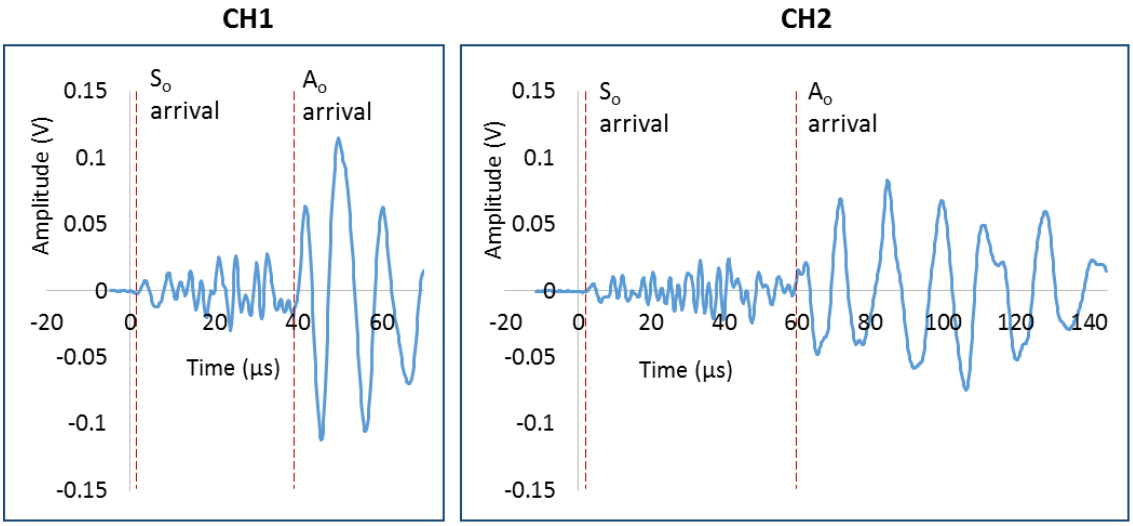


*Figure 3.17: $S_o$ and $A_o$ AE wave mode velocity determination from typical AE hits recorded from subsequent sensors. Notice that there is a larger time delay between the arrival of the $S_o$ and $A_o$ wave modes for the second channel, on account of the $S_o$ wave mode travelling at a higher velocity.*

### 3.1.6 Wavelet Transform

A wavelet transform is the name given to the time-frequency representation of a signal. Whilst it is based on the same mathematical principles as the Fourier transform, a wavelet transform differs from a Fourier transform in that it displays the time varying frequency components of a signal; as opposed to a Fourier transform which gives the spectral details of an entire signal without any time information (Nesvijski & Marasteanu 2007). Figure 3.18 gives a pictorial example of the difference between a wavelet transform and Fourier transform. The Fourier transform displays an average of the signal's frequency spectra, for the entirety of the signal, and thus gives no indication of the changing nature of the signal's frequency. The wavelet transform displays the frequency spectra of the signal with respect to time, and thus can clearly highlight the changing nature of the signal's frequency.

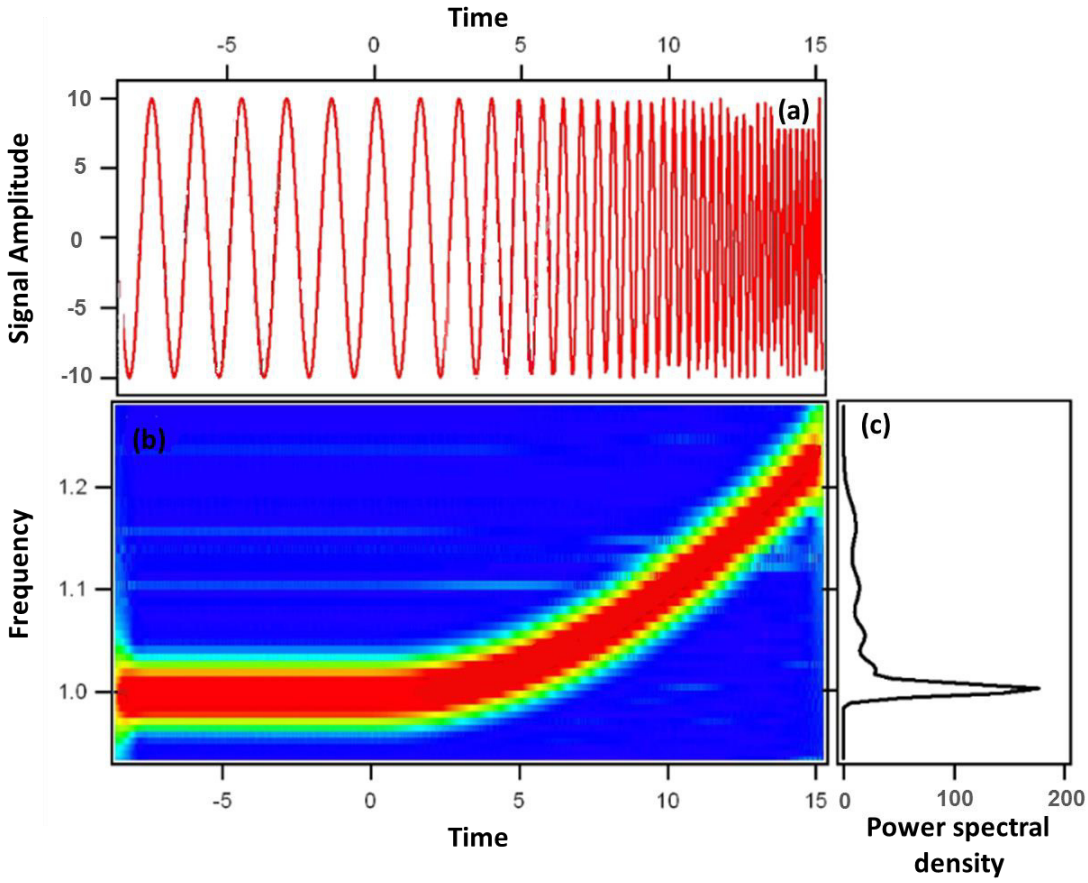


*Figure 3.18: Pictorial example of the difference between a wavelet transform and a Fourier transform; (a) displays the original signal, which has a changing frequency with time; (b) displays a wavelet transform of the signal in (a), where the colour of the represents the frequency power amplitude; (c) displays a Fourier transform of the signal in (a). Figure reproduced from Malegori and Ferrini* (2010)

The wavelet transform is a powerful tool for the interpretation of AE data as it allows for the frequency content of particular sections of a signal to be determined; for example, Hamstad et al (2002) used a wavelet transform to determine the frequencies across which the majority of the energy of the $S_o$ and $A_o$ wave modes existed in a particular waveform.

The software used to create wavelet transforms in this thesis was 'AGU-Vallen Wavelet'; a freeware program developed by Vallen Systeme GmbH, in collaboration with Aoyama Gakuin University and the University of Denver, which is available for download from Vallen Systeme GmbH's website (http://www.vallen.de/downloads).

## 3.2 Digital Image Correlation

For a long time, strain measurements have been an important aspect of mechanical science due to their involvement defining material properties and performance parameters such as the Young's Modulus, Poisson's Ratio and Stress-Strain Curves (Cintrón & Saouma 2008). Over the years however, there has been a growing desire to be able to obtain the full strain field over an area of a test specimen in order to gain a greater understanding of the mechanical performance of that structure and also to be able to better compare empirical results with simulated results. Applying an array of strain gauges to a surface in order to gain a multitude of point measurements and thus build up an image of the strain field is both impractical and costly and so other methods were developed. Initially, photoelastic coatings were adhered to test specimens. Using this method, the surface strains of a loaded specimen are transmitted to the photoelastic coating and, through the use of a reflective cement to bond the coating, the strain field in the coating can be seen using a white light reflection polariscope (Vishay Precision Group 2015). However the technique is inherently invasive and time consuming, and 3D measurements are difficult to perform, hence more accessible optical techniques were developed such as digital image correlation (DIC). DIC is a full field strain measurement technique which uses static images of a structure's surface and digitally automated pattern recognition to determine the surface's displacement and subsequently strain. Thanks to improvements in image processing with microcromputers throughout the 1990's, non-contact techniques such as DIC began to gain momentum and Grediac (2004) presents an overview the use of these measurement methods for composite material characterisation.

Unlike photoelastic coatings and foil crack gauges, DIC's non-contact and non-invasive nature means that it lends itself well to being used alongside AE monitoring, since measurements from both techniques can be taken simultaneously without detrimentally affecting one another. Because of this, DIC has already seen much use as a means of

validating AE testing and methodologies (Carmi et al. 2015; Bhavikatti et al. 2011; Pullin et al. 2010; Alam et al. 2014).

Explained in detail by Schreier et al (2009), DIC works by directly detecting the surface displacements of the structure under investigation from digital images using a process of pattern recognition and tracking. The inspected surface must first be prepared via the addition of a speckle pattern as in Figure 3.19. The method of best practice for the application of a speckle pattern is still a frequent topic of discussion at conferences where DIC users gather, though it is generally agreed that the speckling technique used in each scenario is dependent on a number of factors such as the specimen's material composition, the size of the inspected area and the resolution of the cameras (Kwon et al. 2013). Popular speckling methods include spray paint, airbrush guns, marker pens and screen printing (Chen et al. 2015) and good results have been obtained at Cardiff University in the past using spray painted speckles for specimens between approximately 100x100mm to 500x500mm (Eaton et al. 2008).

*Figure 3.19: Example of DIC speckle pattern from a study on a car bonnet, figure reproduced from Wang et al* (2012)

When using DIC, typically an image is first taken of the surface at rest. After load has been applied to the structure a second image is taken; these two images can then be compared using image correlation software to determine the deflection of the surface due to the applied loading. The image correlation process involves splitting the inspected area into a number of subsets, typically between 13x13 and 31x31 pixels in size. Due to the random speckle pattern applied to the surface, each subset has a unique light intensity (grey level) distribution and, by assuming that this light distribution does not change under deformation, the position of each subset can be tracked from one image to the next (Yoneyama & Murasawa 2008), Figure 3.20. The surface displacement can then be obtained by comparing the known positions of each of the subsets from subsequent images.

The DIC system used during the studies contained in this thesis was a Dantec Dynamics Q-400 (Dantec Dynamics 2013) which consisted of two 2 Megapixel digital cameras, a HiLis (cold, homogeneous, monochromatic) light source and a data logging system capable of receiving up to eight analogue inputs. The cameras were used in conjunction with Schneider Kreuznach lenses, the information for which can be found in Table 3.2. The software used to perform the image correlation process was Istra4D, also supplied by Dantec Dynamics, which uses the procedure outlined by Herbst and Splitthof (2013) to make the calculation.

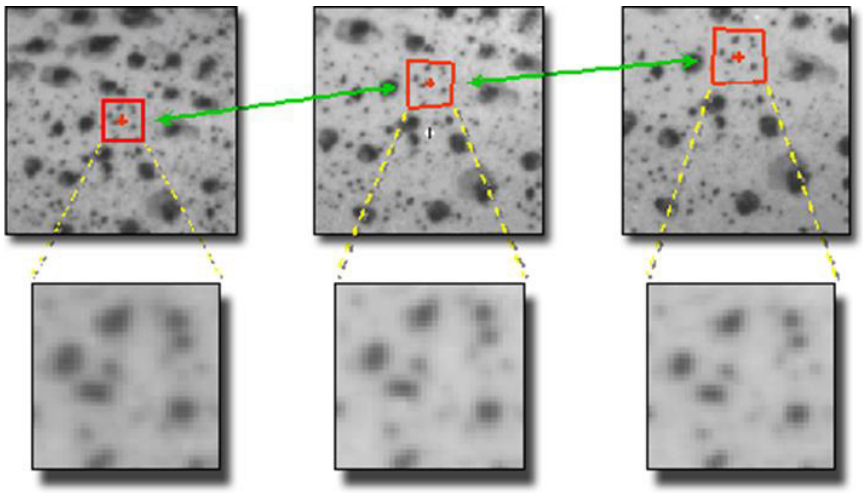

*Figure 3.20: DIC Image correlation process example, figure reproduced from Correlated Solutions* (2013)

*Table 3.2: DIC camera and lens information*

| Cameras | | | |
|---|---|---|---|
| **Number of Cameras** | | **Manufacturer** | **Resolution** |
| 2 | | Limess | 1600x1200 (2 Megapixel) |
| **Lenses** | | | |
| **Manufacturer** | **Name** | **Magnification** | **Working Distance (mm)** |
| Schneider Kreuznach | XNP 2.0/28 Compact | 1:5.9 | >179 |

## 3.3 C-scanning

C-scanning is a method of using ultrasound to inspect the through thickness structure of a specimen. The mechanism by which information is obtained during C-scanning is not dissimilar in nature to the ultrasound scanning techniques used in medical practice to image the inside of the human body and the name 'S-scanning' refers to the way in which the scanning probe is moved in two dimensions in order to take measurements over an area (British Standards Institution 2010). During C-scanning the specimen under inspection sits in a tank which is filled with a coupling medium, typically water. The ultrasonic probe is then passed over the specimen in a straight path along one axis, returned to its original position, moved slightly (typically by the width of the scanning probe's head size) in the tangential axis and then passed over the specimen again, as shown in Figure 3.21. In this way, an image over the entire area is obtained.

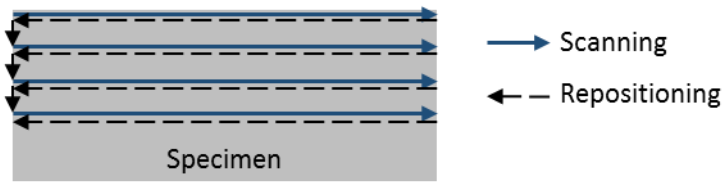


*Figure 3.21: Typical C-scanning inspection path*

A C-scan can be thought of as a series of individual measurements, with each measurement occurring in a similar fashion to those shown in Figure 3.22. The ultrasonic probe acts as both the transmitter and the receiver and, from it, an ultrasonic signal is transmitted through the coupling medium to the specimen. Upon reaching a surface, a portion of the ultrasonic energy will be reflected and a portion will be transmitted.

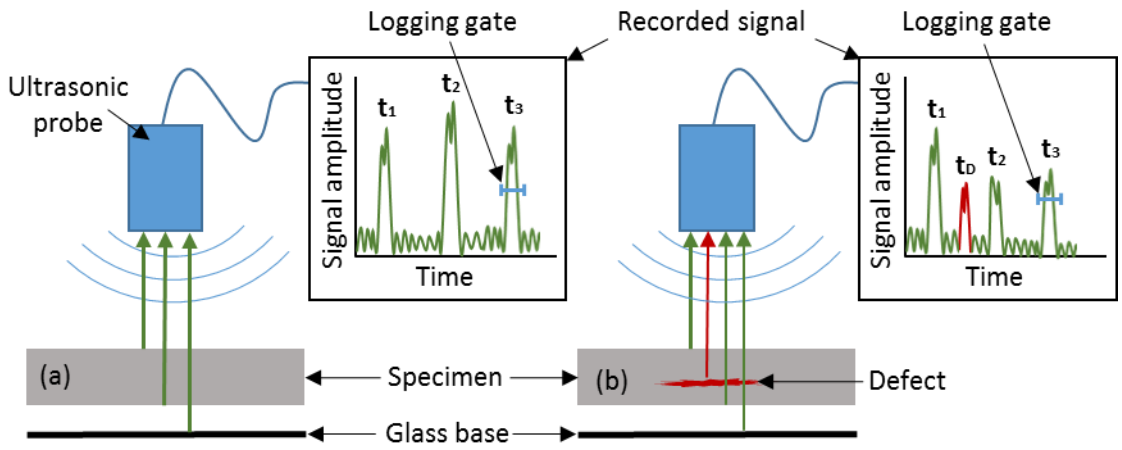


*Figure 3.22: Example of ultrasonic point measurement in a C-scan for (a) a healthy specimen and (b) a damaged specimen*

The distance that the energy has travelled before being reflected will dictate its time of arrival back at the probe as indicated by the spikes of energy at $t_1$, $t_2$ and $t_3$ in Figure 3.22(a). During each individual measurement of the C-scanning process only a single value is logged by the acquisition system; this value is the maximum signal amplitude which occurs in the *logging gate*. The amplitude of the signal reflected from the glass base is chosen to be the amplitude which is logged during a scan by positioning the logging gate at the appropriate time, Figure 3.22. Where there is damage present in the structure, such as a delamination in a composite ply-material, additional surfaces and obstructions are present to reflect and scatter the ultrasonic energy. This results in less energy reaching and reflecting from the glass base, and so a lower signal amplitude is logged, hence damaged regions can be distinguished from healthy regions, Figure 3.22(b). When a large number of these measurements have been taken over the surface of a specimen the areas of damage will be appear as regions of lower signal amplitude.

It should be noted that thickness changes in the specimen under investigation will also result in either more or less or the signal being absorbed/scattered, for thicker or thinner regions respectively. Once a scan has been completed an image as shown in Figure 3.23 is obtained and grants the user an understanding of the through thickness structure of the specimen.

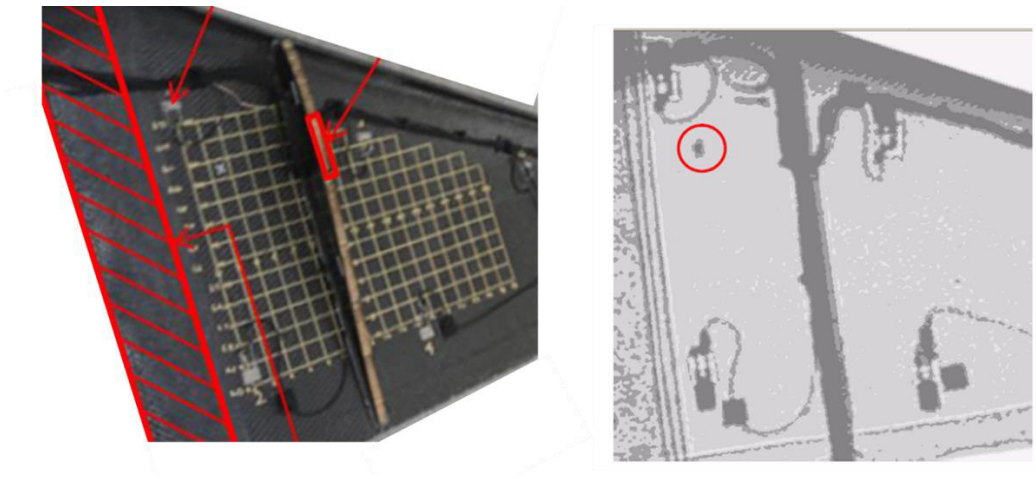

*Figure 3.23: Example of C-scan results taken from a wing shaped specimen with stiffeners, AE sensors adhered to the surface and an impact damage, figure reproduced from Pearson* (2013)

C-scanning's ability to give the user an image of the through thickness state of a specimen is useful for research and validation purposes and has been used in numerous studies in the past to detect damage in composites (Hasiotis et al. 2011; Hocheng & Tsao 2007; Marat-Mendes & Freitas 2011) and also as a validation tool for AE testing (Pullin et al. 2013; Pearson 2013; McCrory et al. 2015).

However, its use is limited as it does not have the spatial resolution to determine the presence of smaller damage mechanisms such as matrix cracking (Seyed Yaghoubi et al. 2012), or any damage which is aligned parallel to the ultrasonic signal (Kapadia 2007).

Previous studies on composite materials have shown good response when using probes with frequencies between 2.5MHz and 5MHz and thus a 5MHz probe was used for the scans on composite materials performed during the studies contained in this thesis.

## 3.4 Graphical Representation

For clarity and ease of understanding, many of the results in this thesis are presented in a graphical format. This is customary for techniques such as AE, DIC and C-scanning, and the common graphical displays which have been used are outlined below;

**Waveforms:** are the packets of raw AE data recorded by the sensors and are presented in the time domain as a plot of signal amplitude vs time, Figure 3.24. The signal amplitude is typically given in Volts (V) or decibels (dB), and time is typical given in microseconds (μs). Decibels are a logarithmic unit calculated, from the ratio of the AE signal voltage with a 1μV reference voltage at the transducer, using Equation 3-2.

$$Amplitude = 20log_{10}\left(\frac{V_s}{V_{ref}}\right)$$

*Equation 3-2*

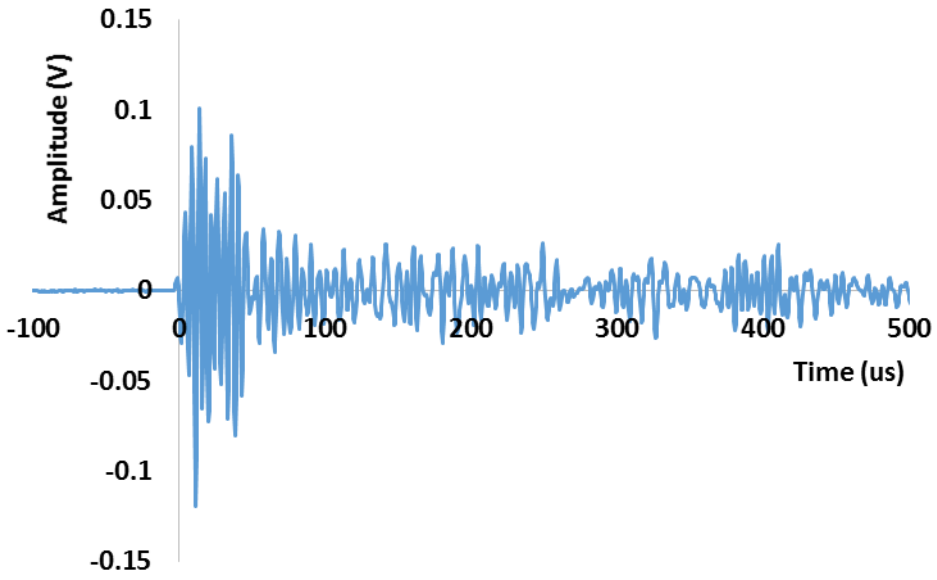


*Figure 3.24: Typical representation of an AE waveform*

**Historical Plots:** are used to describe the amount of AE activity occurring over the duration of a test and give an indication of the progression of AE activity. Historical plots regularly include activity level indicators such as cumulative hits or cumulative energy vs time, Figure 3.25, or AE features such as signal amplitude vs time, Figure 3.26.

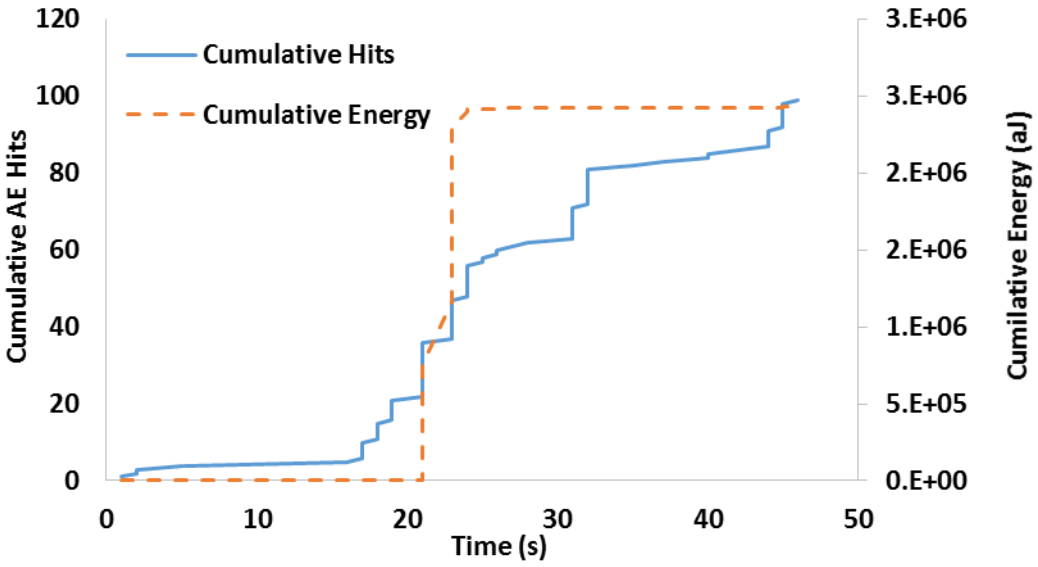


*Figure 3.25: Typical historical plot of cumulative hits and cumulative energy vs time*

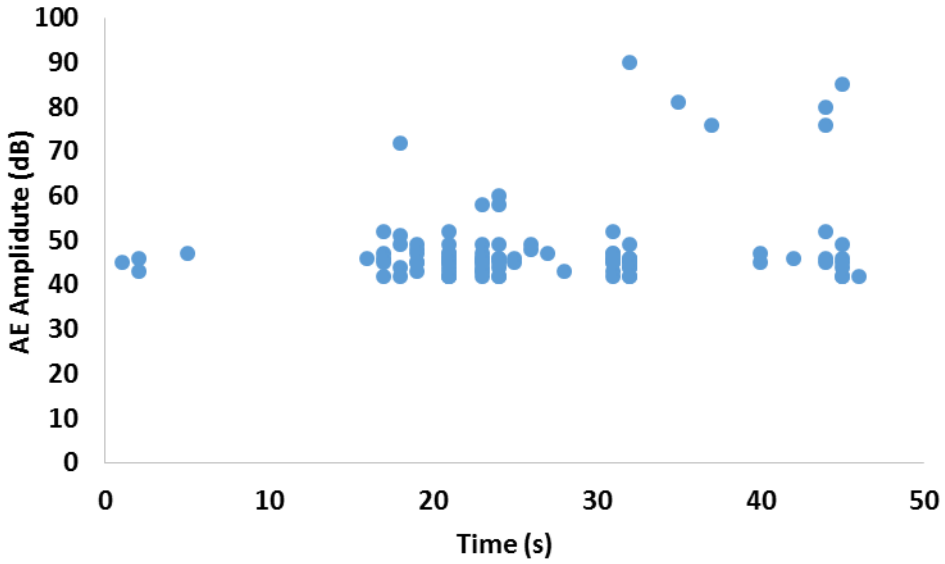


*Figure 3.26: Typical historical plot of an AE feature (amplitude) vs time*

Historical plots can also be made to show the level AE activity relative to the applied load in order to show how the specimen reacted to the load. This is the manner in which results are plotted when investigating the Felicity and Kaiser Effect (Grosse 2002), Figure 3.27.

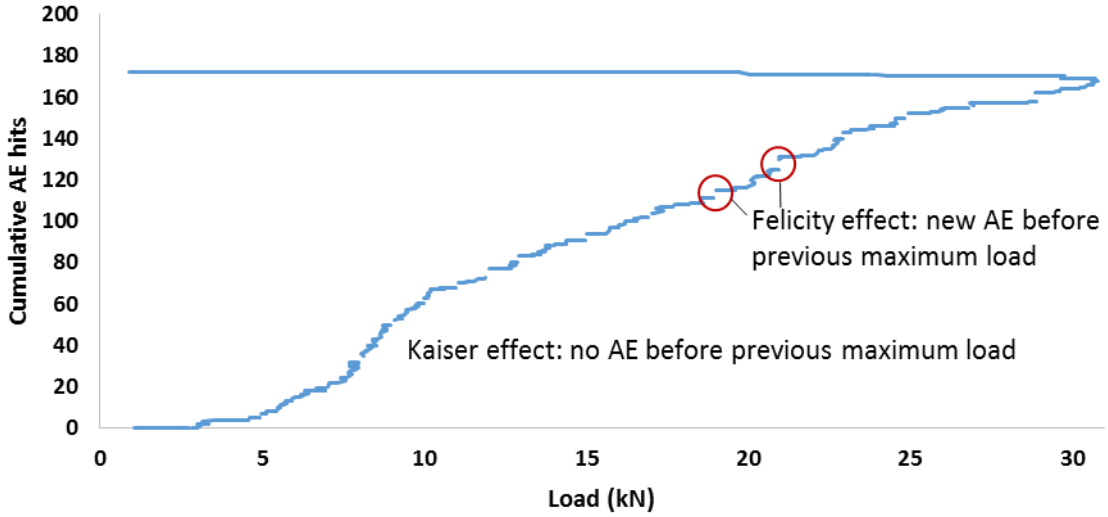


*Figure 3.27: Example of load based historical plot, showing the Kaiser and Felicity effects*

**Location Plots:** are used to indicate the whereabouts of AE activity occurring in a specimen. Linear location plots display the source location of AE between a sensor pair and are often used to locate cracks along the length of a thin specimen. The locations are generally binned spatially so are thus a plot of cumulative events vs distance, Figure 3.28.

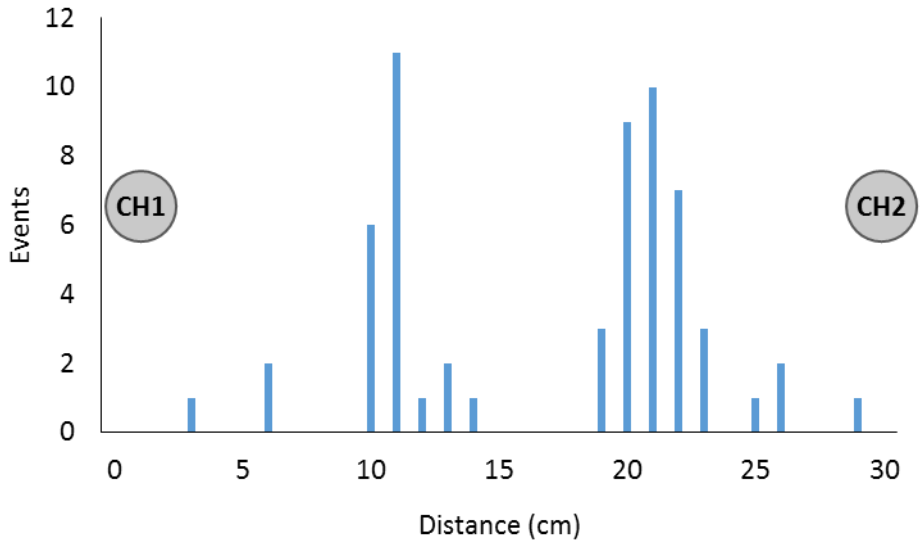


*Figure 3.28: Example of linear location plot*

Two-dimensional AE location plots show the location of AE sources over the monitored area of a specimen. Typically, each AE event located is plotted as a separate point on a

graph of y-position vs x-position, Figure 3.29 (a), and occasionally the energy of the events are binned spatially to show the amount of energy released as AE from regions of the specimen, Figure 3.29 (b).

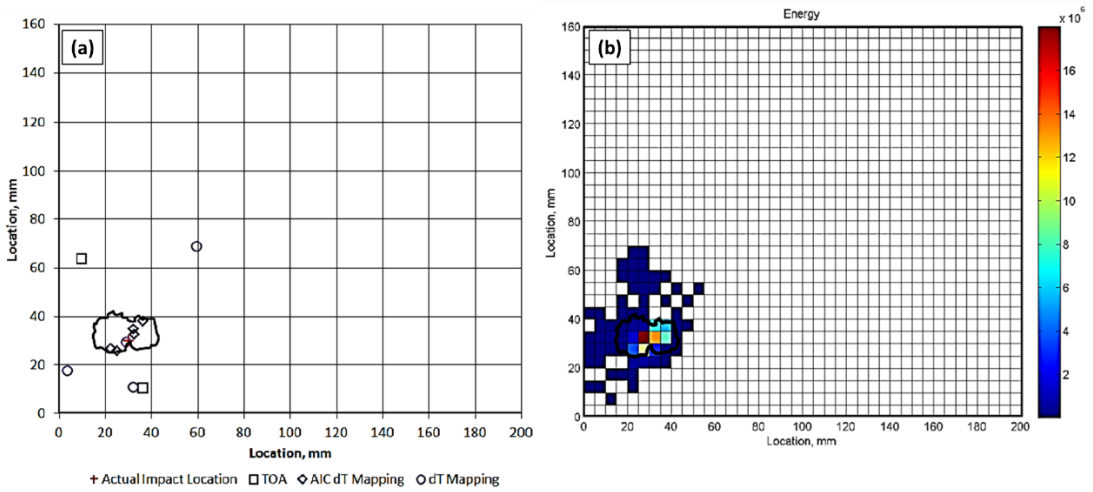


*Figure 3.29: Typical AE location plot for (a) y-position vs x-position location of each event detected and (b) spatially binned energy of located events, figure reproduced from Pearson* (2013)

**DIC contour plots:** The information gathered from a DIC analysis includes the full field displacement of the subsets on the surface of the specimen and the full field strain experienced by the subsets on the surface of the specimen and is typically displayed overlaid onto a photograph of the specimen in question, Figure 3.30.

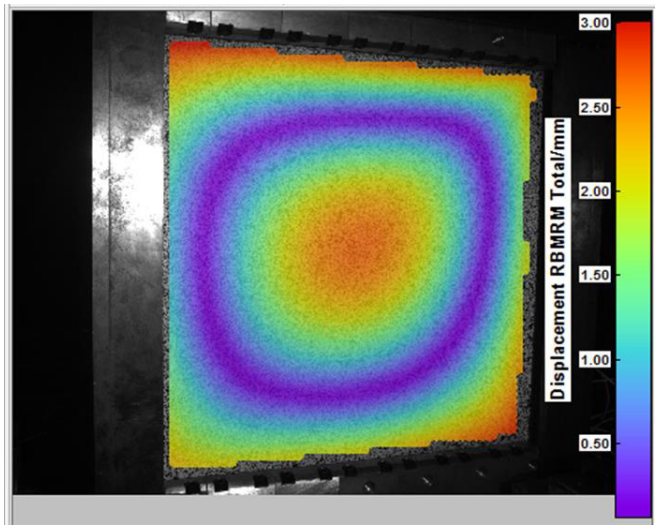


*Figure 3.30: Example of a DIC contour plot showing the total displacement of a buckling test specimen calculate by the correlation software*

**C-scanned images:** show a 2D plot of the attenuation of the ultrasonic signal over the surface of the specimen to give the user an indication of the through thickness structure of the scanned specimen, Figure 3.31. In C-scanned images, the darker the colour the higher the level of attenuation of the ultrasonic signal, hence why the lightning struck area appears darker, as it caused more of the signal to scatter or be absorbed.

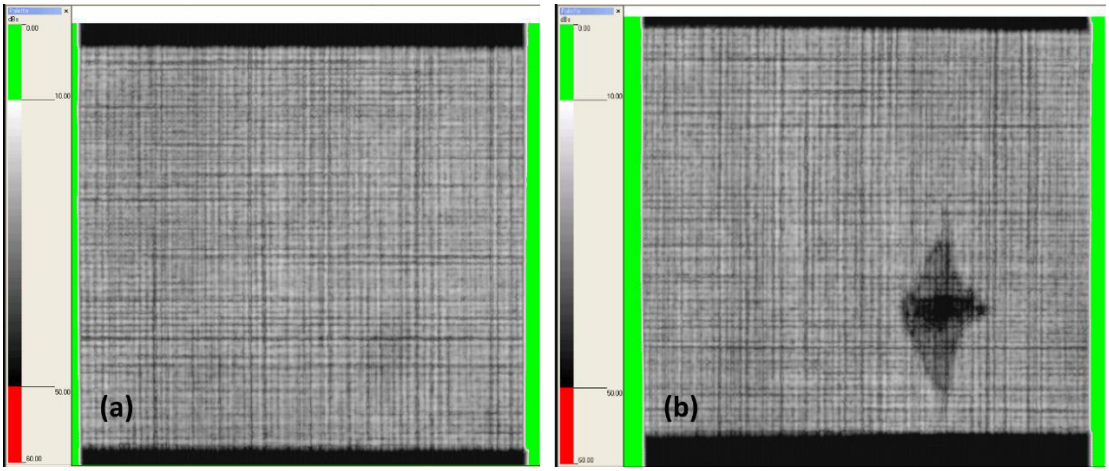


*Figure 3.31: Example of C-scanned image of (a) undamaged carbon fibre composite panel and (b) lightning struck carbon fibre composite panel*

# 4 Delta-T Mapping Optimisation and AE Monitoring of GLARE

## 4.1 Introduction

As described in Section 2.1.3, GLARE is an aerospace specific FML material manufactured from thin sheets of aluminium and glass fibre which offers weight saving compared to aluminium as well as providing better impact, fatigue, fire and corrosion resistance. These benefits have seen the use of GLARE increase and it is now used as a major constituent of the fuselage in the Airbus A380, the world largest passenger aircraft. However, due to the increased complexity brought about by the interaction of the different material layers and their anisotropic properties GLARE presents additional challenges in terms of structural health monitoring and AE compared with monolithic aluminium structures. GLARE's layered material composition, and the introduction of geometric irregularities in the form of splines and doublers, means that the conventional AE TOA location technique might struggle to achieve satisfactory accuracy. Extensive work has been conducted at Cardiff University in the past to improve the accuracy of AE's event location capacity, culminating in the development of a bespoke *delta-T mapping* location technique, explained in Section 2.2.5.3. Previous studies have shown *delta-T mapping* to provide improved accuracy over conventional TOA location however it has not yet seen use on FMLs such as GLARE, for which it might also be able to provide an improved performance.

Despite its proven advantages, *delta-T mapping* is still in its infancy and more can be done to optimise the technique. For instance, since the mapping process of the *delta-T mapping* technique consists of interpolating the difference in time of arrival, Δt, values between points on the training grid in order to obtain a detailed Δt maps for each sensor pair, it stands to reason that the spatial resolution of the training grid used will influence the accuracy of the location result. A coarse training grid would require interpolation over a larger spatial distance in order to calculate the Δt maps and hence might allow the disruptive effects of abnormal geometrical features to be discounted. Somewhat

surprisingly, a previous experiment investigating the effect of training grid resolution concluded that no significant improvement could be made using a finer grid (Eaton et al. 2012), however this study was conducted using a relatively simple specimen with no geometrical abnormalities. Thus the opportunity presents itself to perform a study into both the use of *delta-T mapping* on GLARE for the first time as well as to examine the impact of the training grid resolution on the accuracy of the *delta-T mapping* location results when used in this complex material and in a specimen with many geometric abnormalities.

This chapter contains the details of an experimental study into the effect of the training grid resolution on the *delta-T mapping* location results for AE events collected in a complex, GLARE specimen. The *delta-T mapping* location results were also compared with those obtained using the TOA approach to determine

## 4.2 GLARE Panel Specimen

The GLARE panel used for this study was supplied by Airbus and measures approximately 1200mmx700mm, has an average thickness of 3.1mm and once formed part of the fuselage of an A380 freighter aircraft, Figure 4.1. The panel is made from GLARE 4B, meaning that is comprised of five layers of aluminium and four layers of GFRP, with each GFRP layer containing two prepreg GFRP sheets orientated at 90° to one another, as displayed in the schematic in Figure 4.2. Due to the location from which the panel was cut, it happens that the panel incorporates splice and doubler features. As well as these, it can be seen that the panel encompasses many other features that give it a complex geometry such as aluminium stiffeners, GLARE stringers, rivets and holes, Figure 4.1.

Since it was desirable to assess the training grid resolution's impact on *delta-T mapping*'s accuracy when faced with a more challenging geometry, the area of interest highlighted in Figure 4.1 was selected for the location test to take place as it appeared to be the

most irregular. Present in that region are 17.7mm diameter holes, 9mm diameter rivets, 8.25 mm diameter rivets and 4.5mm diameter holes.

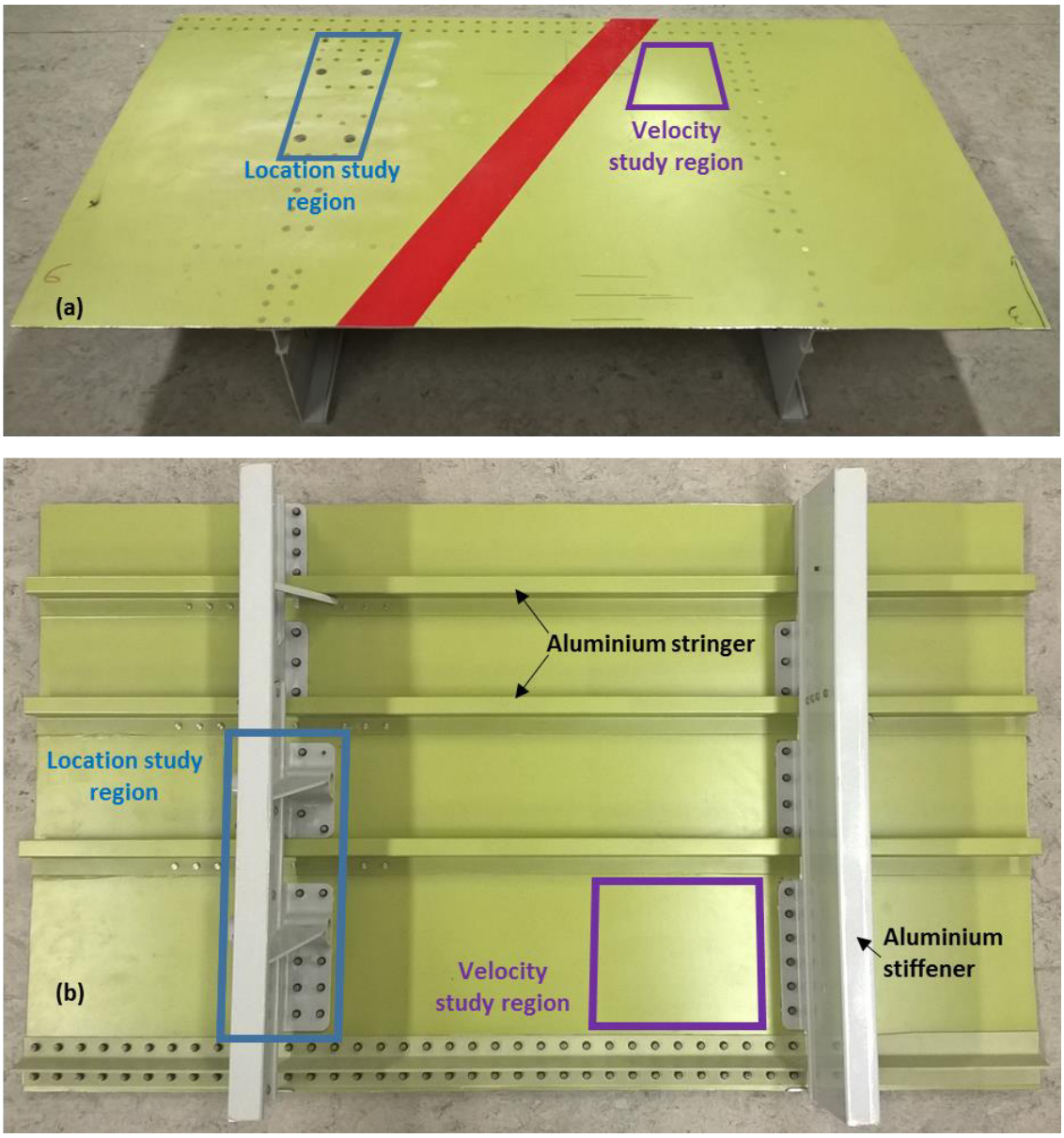


*Figure 4.1: GLARE fuselage panel used for the study (a) from top with the areas used for the delta-T mapping and preliminary velocity study highlighted (b) showing underside with stringers and stiffeners*

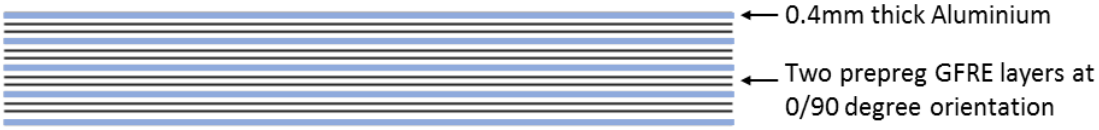


*Figure 4.2: schematic representation of GLARE layup*

## 4.3 Preliminary Investigation into GLARE Specimen $S_o$ mode AE Velocity

In order to calculate locations using TOA the average velocity of the $S_o$ wave mode travelling through the specimen must first be known and thus a velocity test was conducted on the GLARE panel. The velocity study region highlighted in Figure 4.1 was selected for this test as it contained the least number of irregular features which might otherwise disrupt the wavefront and interfere with the velocity calculation. In order to obtain the average velocity for the material, the velocity in the 0°, 45°, and 90° orientations, relative to the longitudinal axis of the specimen, was determined and averaged. The velocity study consisted of acoustically coupling two Nano30 AE sensors (125-750kHz) with multipurpose brown grease onto the specimen in line with each of the three orientations tested. In order to reduce the error associated with first arrival time detection, it was desirable to position the sensors at a large distance from one another, however the stringers on the underside of the specimen created spatial constraints and so the furthest the sensors could be positioned from one another was 275mm, 160mm and 160 mm for the 0°, 45°, and 90° orientations respectively. Once in place the sensors were connected to PAC pre-amplifiers, each with a built in frequency filter of 20-1200kHz, set to a gain of 40dB. Data was captured using a MISTRAS PCI2 system with the AE acquisition settings shown in Table 4.1.

*Table 4.1: AE Acquisition settings*

| Threshold (db) | Filter (kHz) | Sample rate (kHz) | Length (ms) | Pre-trigger (ms) | PDT (ms) | HDT (ms) | HLT (ms) |
|---|---|---|---|---|---|---|---|
| 40 | [20-2000] | 4000 | 1.5 | 0.5 | 0.4 | 0.8 | 1 |

Ten H-N sources were excited 30 mm behind sensor 2 at each orientation configuration in order to allow enough distance for plate waves to be established in the panel before the wavefront reached sensor 2, Figure 4.3.

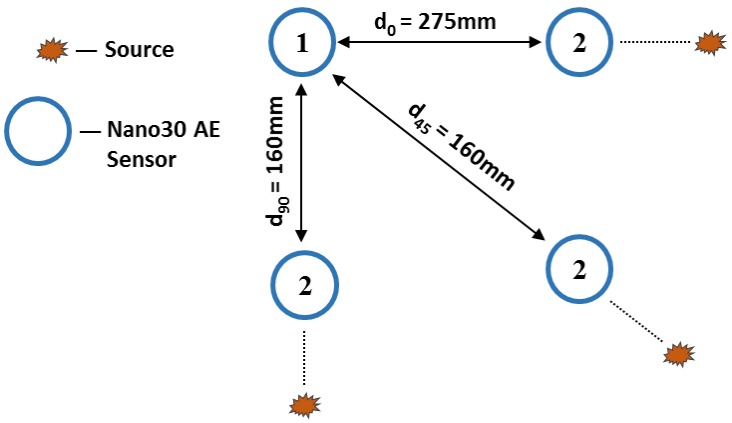


*Figure 4.3: GLARE velocity test configuration*

The average time of flight of the $S_0$ wave mode between the sensors at each orientation was calculated from the ten recorded events. The distance between the sensors was then divided by the average time of flight for each orientation to obtain the velocity and those velocities were in turn used to calculate the average $S_o$ mode velocity for the specimen to be 4836 ± 65 m/s, Table 4.2.

*Table 4.2: Velocity of H-N source wave in GLARE panel*

| Orientation (degrees) | $S_0$ wave mode velocity (m/s) |
|---|---|
| 0 | 4918 ± 66 |
| 45 | 4719 ± 80 |
| 90 | 4870 ± 48 |
| **Average** | **4836 ± 65** |

## 4.4 Delta-T Mapping and TOA Location Test Procedure

A 1x1cm resolution training grid spanning an area of 15x35cm was drawn onto the upper surface of the specimen in the area of interest selected. Six Nano30 AE sensors (125-750kHz) were then clamped in pseudo-regular positions surrounding the grid using a pair of magnets on the top and bottom surfaces and acoustically coupled to the surface using multipurpose brown grease, Figure 4.4. Pseudo-regular positioning was used as previous studies using *delta-T mapping* have found that location inaccuracies can arise

due to symmetrical sensor placements causing similar Δt values to have multiple crossing points (Eaton 2007). The AE hardware and acquisition setup matched that used in the preliminary velocity study.

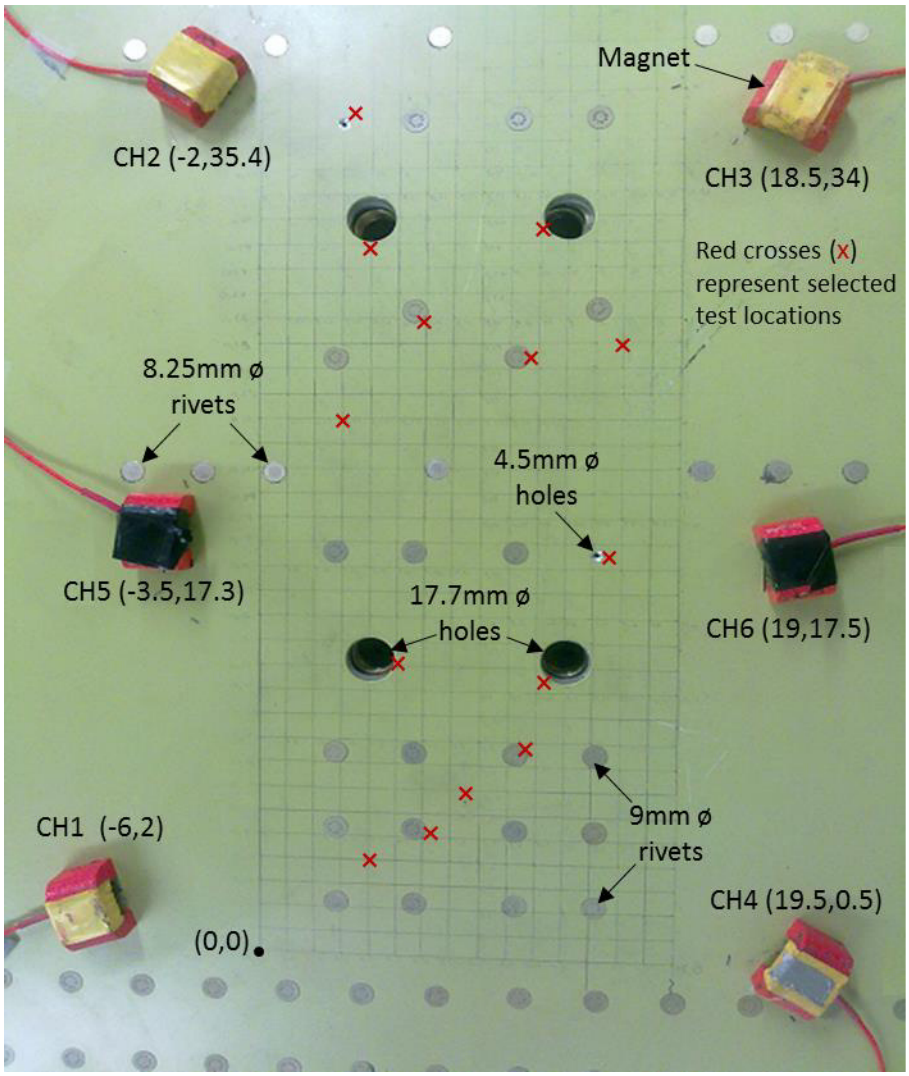


*Figure 4.4: 1x1cm resolution training grid and AE sensors attached to GLARE specimen with geometric features and selected test locations highlighted*

To collect the data necessary to generate the Δt maps for each sensor pair, AE was recorded whilst a H-N source was generated five times at each grid point. In order to ensure that each event was only registering one hit on each channel during the collection of this data, the AE acquisition setup was adjusted via the addition of front end filters as required. The Δt maps, containing the information of the contours of constant Δt between sensor pairs, were then created from the training grid data collected from the 1x1cm

resolution grid by processing that data using the algorithms designed by Baxter (2007). Rather than collect entirely new sets of training grid data for lower resolution training grids, the raw data collected for the 1x1cm grid was manipulated to remove the events necessary to mimic the data that would have been collected for 2x2cm, 3x3cm, 4x4cm, 5x5cm and 7x7cm resolution grids and Δt maps for these resolutions were created.

Fourteen locations inside the delta-T grid were then selected based on their surrounding geometrical features for use in the location test, Figure 4.4, and AE was recorded whilst ten H-N sources were generated at each of them. The AE data recorded from each of these chosen locations was then processed using the *delta-T mapping* technique in conjunction with each of the six different Δt map sets that were created from the six different resolution training grids in order to calculate the estimated locations of each event for each grid resolution.

As well as investigating the effect of the delta-T grid density on the accuracy of its location calculation, this study also aims to provide a comparison of *delta-T mapping*'s accuracy against conventional TOA Location for the GLARE geometry. To this end, the AE recorded from the H-N sources at the fourteen chosen locations were also processed using the conventional TOA location technique in the PAL's AE WIN software.

## 4.5 Results and Discussion

Examples of the Δt maps created from each of the training grid resolutions can be seen in Figure 4.5. Note first that due to the total size of the grid, 15x35cm, it was not possible to obtain Δt maps up to the edge of the grid area for each of the resolutions, hence why some of the grids display zero values around the perimeter. It can be seen that there is a large disparity in the level of detail between the Δt maps created from the 1x1cm and 7x7cm resolutions training grids. The 1x1cm grid produced the Δt map with the most amount of detail and the level of detail then diminishes for lower resolution grids, as expected.

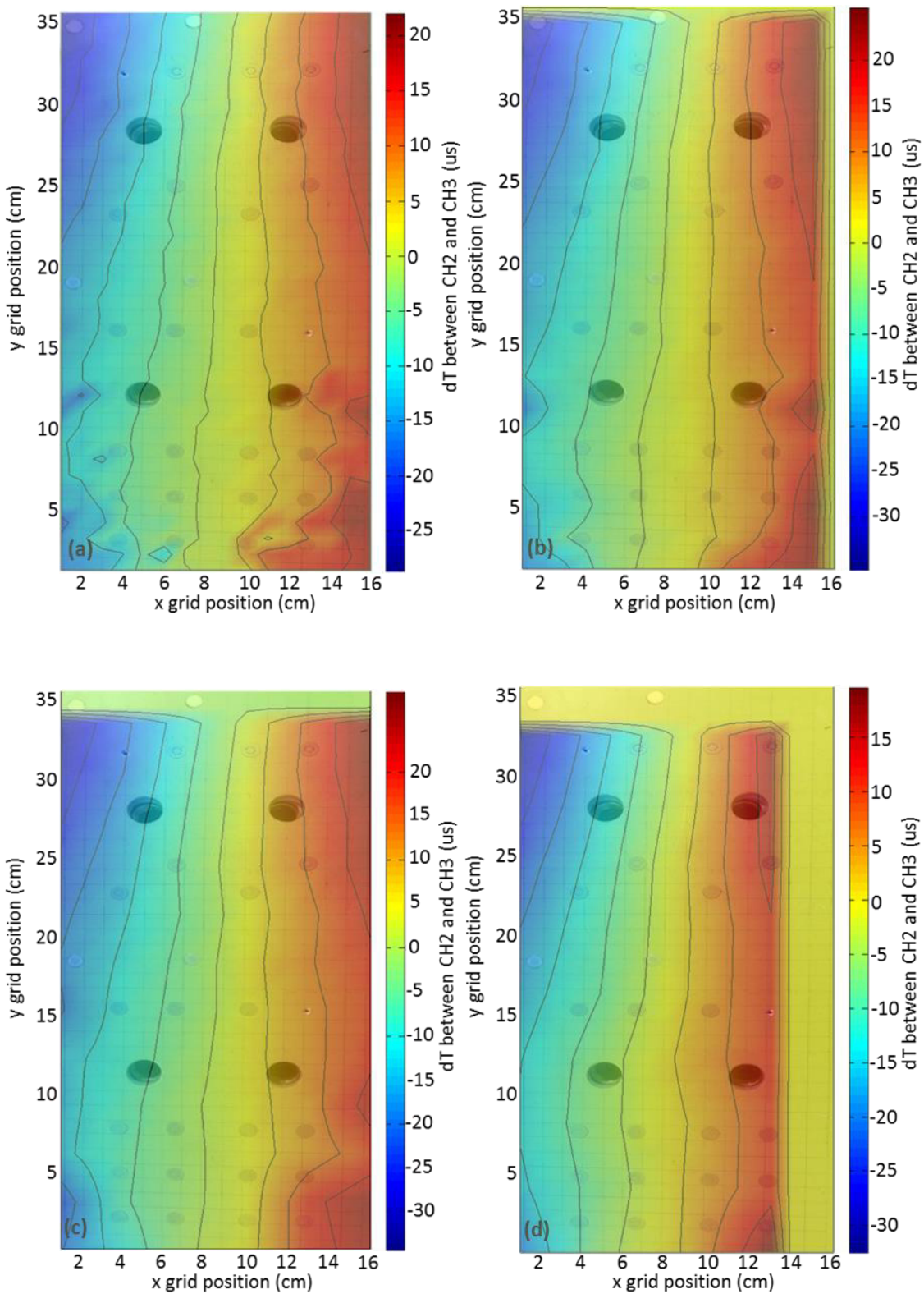
(a)
(b)
(c)
(d)
y grid position (cm)
x grid position (cm)
dT between CH2 and CH3 (us)

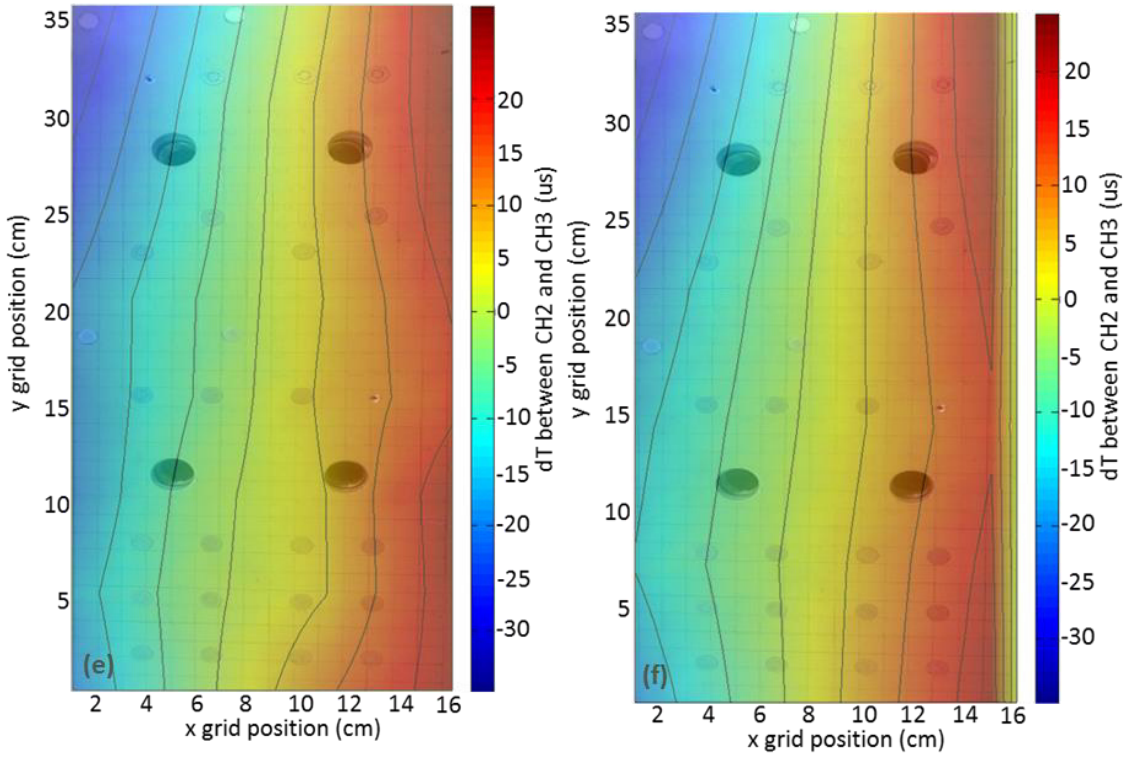


*Figure 4.5: Δt maps between CH2 and CH3 generated from (a) 1x1 (b) 2x2 (c) 3x3 (d) 4x4 (e) 5x5 and (f) 7x7 cm resolution training grids with contours of constant Δt and a photo of the grid area overlaid*

Paying attention to the photo of the specimen's surface which has been overlaid with 50% transparency onto the figures; it is interesting that the impact of the holes on the Δt values is not more pronounced. It might be expected that when the a source is generated in a position that has a direct line of sight to one sensor but has its line of sight obscured by a hole to another sensor that a pronounced effect would be seen in the Δt values between those two sensors due to disruptions in the wave's path, but that does not appear to be the case.

The locations of the fourteen selected test points, as well as the results of the TOA and 1x1cm resolution *delta-T mapping* location techniques can be seen in Figure 4.6. It is apparent that both techniques have calculated locations which are in reasonable agreement with the actual source locations, but with the TOA results visually appearing more erroneous than those calculated by *delta-T mapping*. To obtain a quantitative measure of the accuracies of the two techniques, the distance from each calculated location to the actual location was determined to give a 'distance error' for each location.

The distance error for each location was then averaged to obtain the average error for each technique. This was carried out for the TOA locations and the *delta-T mapping* locations for each resolution training grid, Figure 4.7.

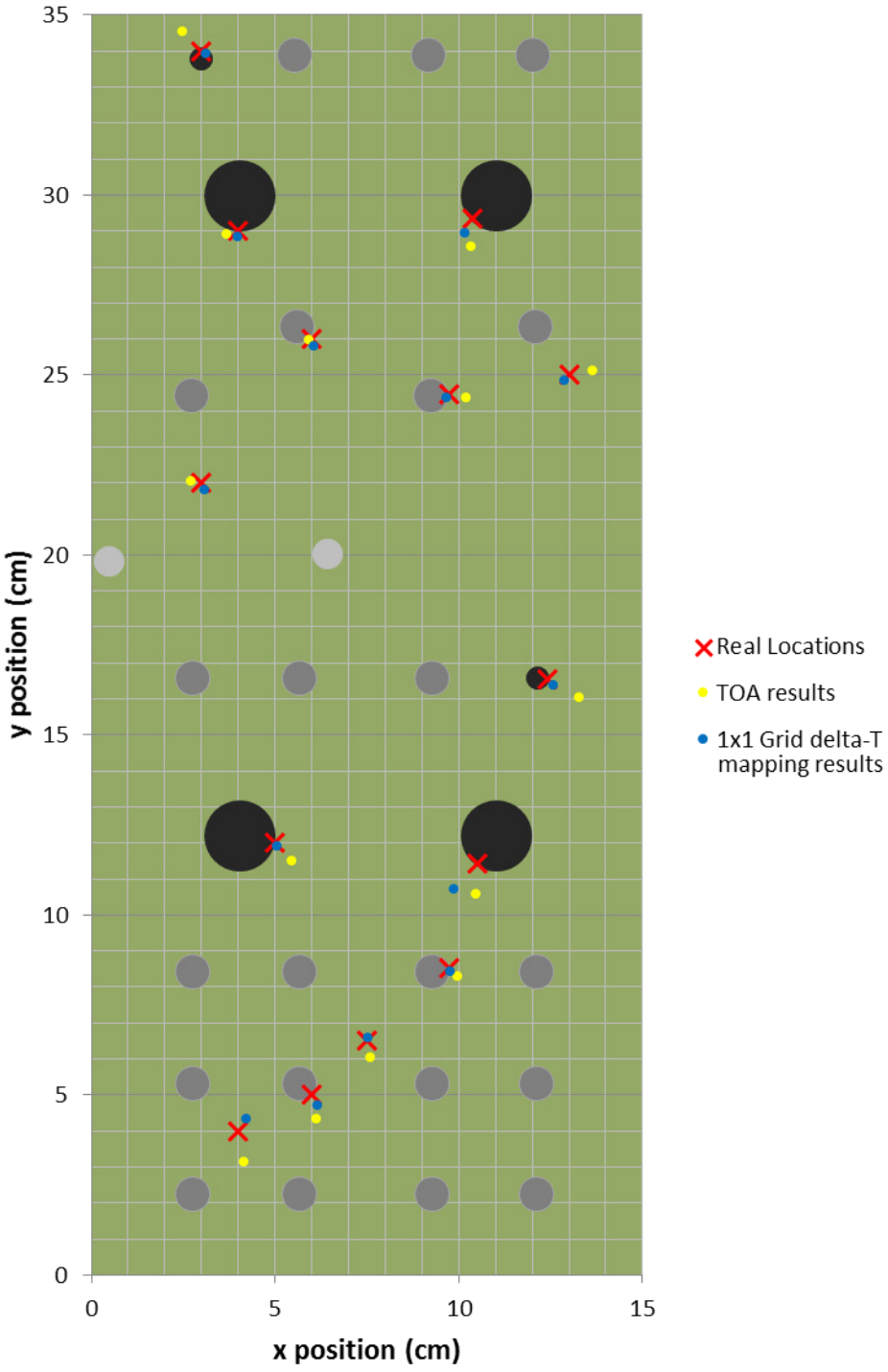


*Figure 4.6: Comparison of locations calculated using TOA and delta-T mapping against actual source location*

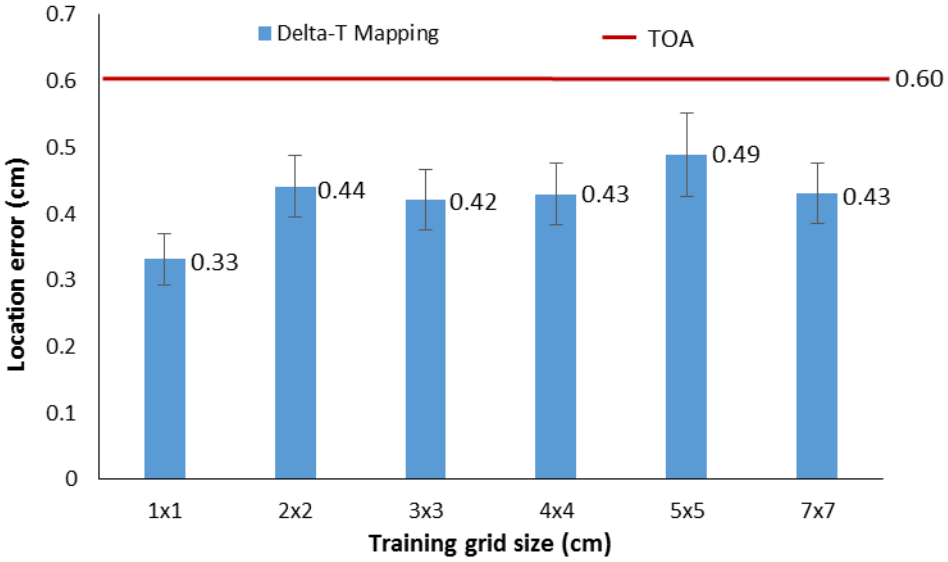


*Figure 4.7:* Average error from actual locations for TOA and different delta-T grid sizes

It is observed that both TOA accurately locates the artificial sources in the geometry to within 0.603cm of their true position and that the *delta-T mapping* technique always achieves a lower error. The error for the *delta-T mapping* results produced by the 1x1cm resolution training grid was the lowest of any technique offering a 45% reduction in error over TOA and a 25% reduction in error compared to the average error of the other resolution *delta-T mapping* results. Somewhat surprisingly, the error in the *delta-T mapping* results produced from the 2x2, 3x3, 4x4, 5x5 and 7x7 cm was reasonably consistent with no reduction in accuracy observed for lower resolution grids.

Intuitively, it might have been expected that the error of the TOA results would be much higher for this complex, composite specimen, however several reasons for this become apparent. TOA's accuracy has been documented to decrease when used in composite materials with highly orthotropic properties, such as unidirectional GFRE in which velocities have been recorded to vary from 4682 m/s along the fibre orientation to 2594 m/s orthogonal to the fibre orientation (Toyama et al. 2002). This is because the conventional TOA calculation assumes a constant wave speed in all directions. The results in Table 4.2 show that the $S_0$ wave mode's velocity exhibits little variation with propagation direction in the GLARE specimen and so the assumption made by the TOA calculation method holds approximately true and its accuracy is not diminished.

Further to this it should be noted that the H-N sources used during this location study produce AE signals with much larger amplitudes than those that would be expected in most real-world applications. The TOA technique utilises a threshold crossing method to determine the first arrival time of AE and thus can suffer inaccuracies when detecting low amplitude AE since the first arrival is less pronounced and hence missed. Therefore, the use of a H-N source means that the TOA accuracy calculated in this study is larger than could be expected to occur in practice. In order to overcome low amplitude signals, the *delta-T mapping* technique incorporates an AIC calculation to more accurately determine the first arrival time of AE signals. Acknowledging this, it is suggested that the improvement in accuracy seen by *delta-T mapping* over TOA would be more pronounced in a practical application where lower amplitude AE is expected to be released.

Finally, the six sensor array used in this study has as average sensor spacing of 19.4cm, from one sensor to the next adjacent sensor. This is a lower sensor spacing than would be expected to occur in practice and would contribute to greater accuracies in both techniques, especially TOA which would benefit more from the decreased levels of signal attenuation brought about by this closer sensor spacing due to the reasons highlighted in the previous points about first arrival time calculation.

It was predicted that the large number of rivets in the specimen would disrupt the wave propagation, altering the wave velocity and hence first arrival time. This would result in a reduction in the accuracy of the TOA locations as TOA assumes the wave velocity to be constant in all directions and the effects of these geometrical abnormalities would not be accounted for. However, the accuracy of the TOA results was acceptable and the detrimental effect of the rivets and irregular geometry does not appear to have been observed to any significant degree, likely due to the size of these features being too small to make a disruptive enough impact on wave propagation.

There is a large jump in error between the 1x1 cm resolution *delta-T mapping* results and the other grid resolution *delta-T mapping* results. The largest geometrical features

on the surface of the GLARE specimen are the 1.77 cm diameter holes. Thus the observation can be made that it is when the training grid size is larger than the largest defect size that the largest increase in error is observed in the *delta-T mapping* results.

Looking at the results of the velocity study; the directionally uniform velocity observed in the GLARE specimen suggests that GLARE has a fairly consistent in-plane stiffness in all directions, since the $S_0$ mode velocity is related to the in-plane stiffness of the material, despite the fact that the material layup contains orthotropic GFRP layers. The uniformity of the velocity suggests that the signals generated were travelling in an isotropic material which leads to the hypothesis that the majority of the AE wave energy may be travelling in the upper most, isotropic, aluminium layer of the GLARE material and not in fact traveling as a plate wave through the entire thickness of the GLARE. To investigate further, PAC Dispersion Curves software was used to calculate the $S_0$ mode wave speed in a 0.4 mm thick aluminium plate to be 5400 m/s. Furthermore, as previously stated, $S_o$ mode AE velocity in GFRP has been recorded to vary from 4682 m/s along the fibre orientation to 2594 m/s orthogonal to the fibre orientation and measure at 3205 m/s for a mixed layup. The average velocity measured in this study, 4836 m/s, is somewhere between the velocities expected for the constituent materials and thus it is unlikely that the majority of the AE wave energy is merely travelling in the upper most aluminium layer of the GLARE as theorised.

## 4.6 Conclusions

H-N sources were generated on the surface of a complex GLARE panel specimen and located using both TOA and *delta-T mapping*. The data recorded from the H-N sources was processed with *delta-T mapping* several times, each time with using Δt maps generated from training grids of different resolutions; 1x1, 2x2, 3x3, 4x4, 5x5 and 7x7 cm. The location results showed that *delta-T mapping* produced more accurate results than TOA for all grid resolutions tested. The most accurate locations were obtained from the *delta-T mapping* results processed using the Δt maps generated from a 1x1cm resolution training grid which could locate signals to within 0.332cm of their actual

position. After an initial reduction in *delta-T mapping* location accuracy from the 1x1cm to 2x2cm resolution training grid, from 0.332cm to 0.441cm, there was no further decrease in the accuracy of the *delta-T mapping* results for diminishing grid resolutions. The observation was made that once the training grid resolution exceeded the largest defect in the GLARE panel, which in this case was 1.77cm, that the accuracy of the *delta-T mapping* results decreased and after this point it remained more-or-less constant. Whilst true that *delta-T mapping* offered a 45% reduction in error when compared to the TOA results, it should be noted that all techniques produced results that would be satisfactory in practice. This said, due to a number of contributing factors discussed, it is expected that the accuracy of the TOA results would be significantly lower than *delta-T mapping* in practice where signal amplitudes would be much lower and sensor positioning would be scarcer.

A velocity study was also carried out on the GLARE panel specimen with the results showing that the $S_o$ Lamb wave mode velocity varied only slightly with propagation direction, and had an average velocity of 4836 m/s.

The work from this chapter formed the basis for the following conference publication:

J. McCrory, R. Pullin, M. R. Pearson, M. J. Eaton, C. A. Featherston and K. M. Holford. (2012) 'Effect of Delta-T Grid Resolution on Acoustic Emission Source Location in GLARE', 30th European Conference on Acoustic Emission Testing & 7th International Conference on Acoustic Emission, University of Granada, Spain; 09/2012.

# 5 Additive Hits Analysis

## 5.1 Introduction

One of the large challenges for the development of a fully realised SHM system is satisfying the power requirements. Because of this, the damage detecting component of an SHM system should require minimal power to operate and even then careful power management is required in order to achieve full functionality without the need for large power reserves, such as batteries, which would increase the mass of the system. Wavestreaming, described in Chapter 2, is an AE technique that records packets of AE information periodically and thus requires less power than an AE technique that collects information continuously. The use of wavestream collection to track the progression of damage in a structure has been demonstrated in the past. By comparing the RMS values of the wavestreams collected in a tensile fatigue test, Pullin et al (2013) were able to identify the presence of impact damage in a carbon fibre composite panel. Furthermore, a more detailed investigation of the frequency spectra of the wavestreams recorded suggested that wavestreaming could not only detect but also track the progression of different AE source mechanisms in the structure. Following on from a similar study by Mascaro et al (2005), Eaton et al (2014) used wavestreaming to monitor the drilling process in a carbon fibre composite panel; the RMS of the wavestreams was used as an indicator to track the progression of wear in the tool and also the condition of the hole being drilled. Subsequently a more detailed, windowed RMS and frequency analysis was used on a wavestream by wavestream basis to investigate the exact cutting, wearing and damage mechanism as the drill bit became more worn. Holford et al (2013) looked at the potential of wavestreaming techniques in rotating machinery applications by monitoring AE in a cyclically loaded gear tooth. A rolling cross-correlation approach, whereby each recorded wavestream was compared to the previous one, enabled the detection of the increase in regularity which occurred in the wavestreams due to damage emitting AE at regular intervals during loading. A more detailed banded frequency

analysis was able to more thoroughly visualise the presence and progression of damage in the tooth.

Despite its merits, analysing wavestreaming information has a number of drawbacks. Since AE data is typically captured at around 2 to 5 MHz, recording data continuously for an entire second results in data files with millions of data points meaning that manipulation of this data is slow and computationally intensive. Furthermore, there is no guarantee of capturing high-amplitude/relevant AE data during the time that the wavestream is being recorded and frequently the majority of what is recorded is background noise which complicates attempts to withdraw information from the *useful* parts of the recording, i.e. the transient AE hits, as in Figure 5.1. Additionally, if the noise happens to occur at a consistent frequency then there is the chance that a frequency analysis might be skewed and interpretation of that data would become problematic, especially if the analysis involved investigating the peak frequency.

To maintain the advantages that wavestreaming offers, such as the ease of data analysis by means of comparison of successive wavestreams and the inherent power saving due to its periodic activation, whilst overcoming the issues involved with the size of the data files recorded and the effect of noise on the frequency power spectrum; a novel method of analysing hit driven data, called an *Additive Hits Analysis* (AHA), is presented.

An Additive Hits Analysis consists of consecutively conjoining all of the AE hits which are recorded within a user specified time window to produce one, longer signal, which closely resembles a wavestream recording but without the vast periods of low amplitude noise. This can be repeated for a number of time windows throughout the duration of a test, in order to obtain several AHA data sets. A similar analysis methodology to that which is employed on conventional wavestream data can then be performed on this additive hits data but with fewer of the aforementioned issues regarding data size and noise.

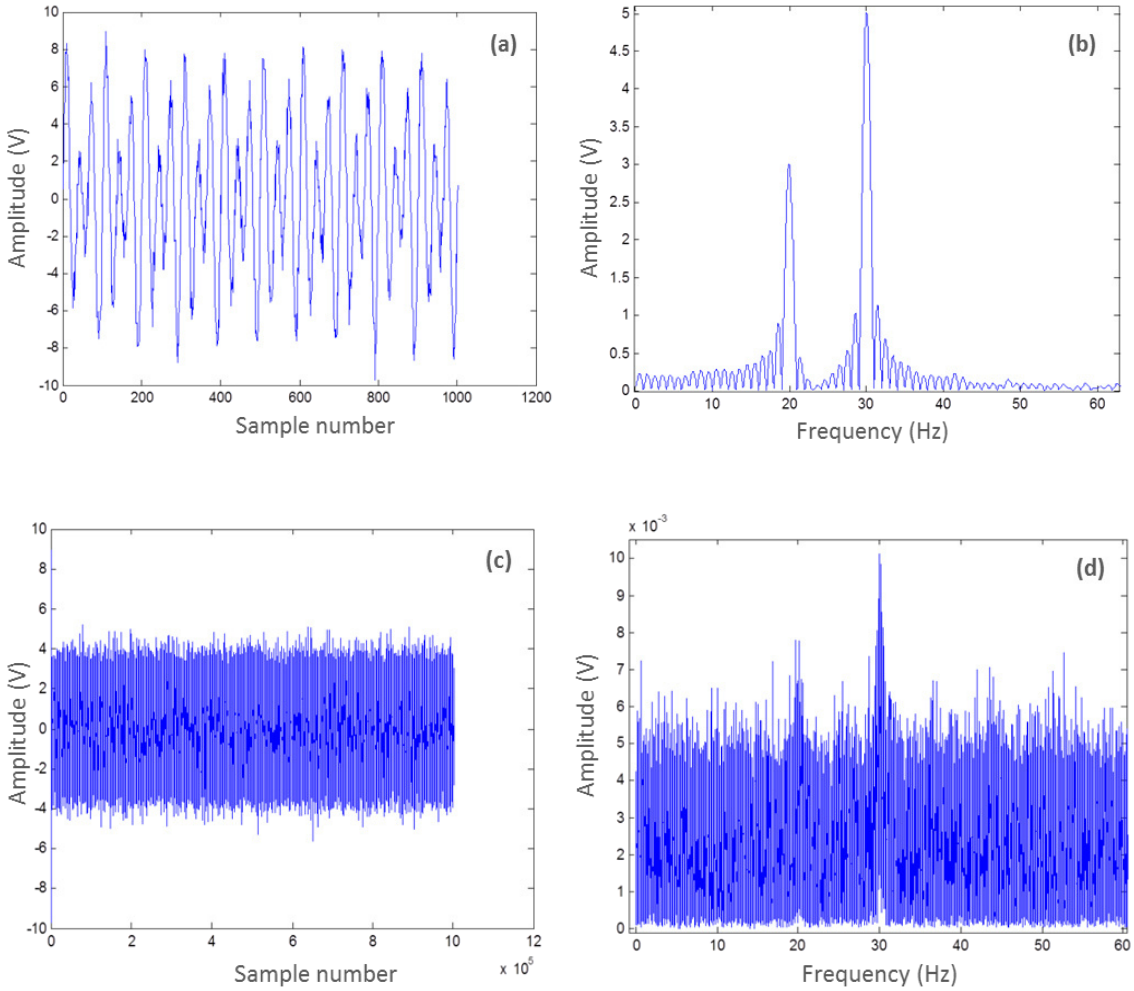


*Figure 5.1: (a) Signal 1: 1000 point long, 3 Volt 20Hz and 5 Volt 30Hz sine waves added together with noise of the same length (b) Frequency spectrum of signal 1 (c) Signal 2: 1000 point long 3 Volt 20Hz and 5 Volt 30Hz sine waves added together with 1,000,000 point long noise signal (d) Frequency spectrum of signal 2.*

The procedure for generating the AHA data files, by sequentially summing waveforms in user specified time windows, would take a considerable length of time to do manually; thus a Matlab script was created which automated the process. This chapter describes a fatigue experiment that was carried out on a cantilever steel beam specimen, and the AHA of the data recorded from that experiment, in order to demonstrate the AHA technique and determine its effectiveness at tracking crack propagation when compared with conventional wavestreaming.

## 5.2 Experimental Procedure

### 5.2.1 Specimen preparation

In order to investigate whether the AHA approach provides the aforementioned benefits over conventional wavestreaming, the two techniques were compared, side-by-side, using the same test data. To this end a fatigue test experiment was designed for a 1000x70x20mm aerospace grade 300M steel bar specimen. The specimen was notched prior to testing in order to accelerate the development of a crack and also allow the location of that crack to be known; this provided confidence that the AE and DIC monitoring were being carried out in the correct region of the specimen. The notch had the dimensions shown in Figure 5.2. A cylindrical cut was also made toward one end of the specimen as a seat for a steel roller which would later serve to transfer load to the specimen. The surface of the specimen in the region around the notch was polished with acetone before the 10x10mm *delta-T mapping* training grid seen in Figure 5.3 was drawn onto the surface. Four MGL Nano 30 AE sensors (125-750kHz) were then adhered to the surface using Loctite 595 silicone sealant, which also served as the acoustic couplant between the sensors and the specimen, in the positions shown in Figure 5.3. Pressure was applied to the sensors during the adhesive curing process and, once cured, an H-N sensitivity test was conducted on each of the sensors with satisfactory results.

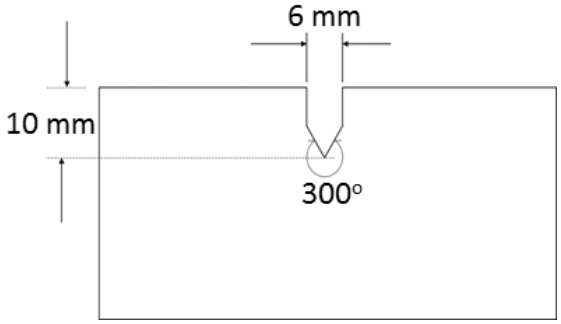


*Figure 5.2: Dimensions of the notch*

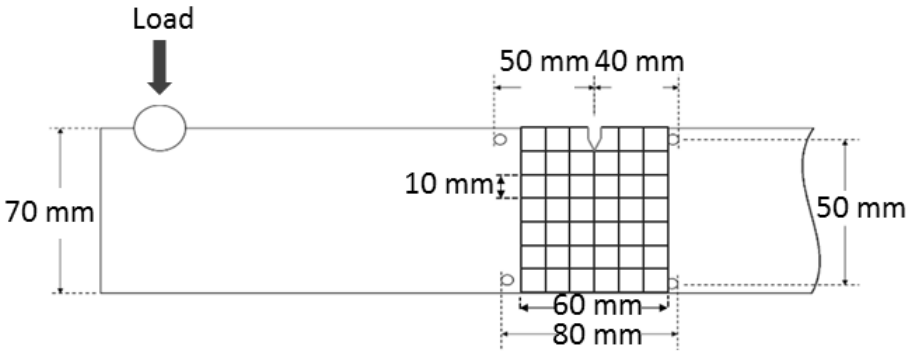


*Figure 5.3: Position of sensors and delta-T mapping training grid*

The sensors were connected to PAC pre-amplifiers, each with a built in frequency filter of 20-1200kHz, set to a gain of 40dB. These were in turn connected to a PAL PCI-2 acquisition system which was used throughout the entirety of this testing to record AE data. The acquisition settings within the AEWin software were set as shown in Table 5.1.

*Table 5.1: AE Acquisition settings*

| Threshold (db) | Filter (kHz) | Sample rate (kHz) | Length (ms) | Pre-trigger (ms) | PDT (ms) | HDT (ms) | HLT (ms) |
|---|---|---|---|---|---|---|---|
| 40 | [20-2000] | 2000 | 1.5 | 0.5 | 0.2 | 0.4 | 1 |

The delta-T training data was collected, by generating five H-N sources at each of the grid points, and subsequently used to calculate the delta-T maps for this specimen. In order to assess the accuracy of the Δt maps generated a number of trial H-N sources were generated at the positions outlined in Table 5.2 and Figure 5.4 and recorded by the AE loading test.

AE was not the only monitoring method used during this test. In order to verify the changes in the rate of crack growth that were to be detected by AE, and gain a more thorough understanding of the crack progression, DIC monitoring was also used. In preparation for this, a speckle pattern was applied to the specimen, in the region

surrounding the notch on reverse side to which the training grid was drawn, using black and white spray paints, Figure 5.5.

*Table 5.2: Map accuracy test break locations*

| Location | Coordinates |
|---|---|
| Loc 1 | (3 , 5) |
| Loc 2 | (3 , 4.5) |
| Loc 3 | (3 , 3.5) |
| Loc 4 | (3 , 2.5) |
| Loc 5 | (3 , 1.5) |
| Loc 6 | (3 , 0.5) |
| Loc 7 | (1.5 , 4.5) |
| Loc 8 | (5.5 , 3.5) |

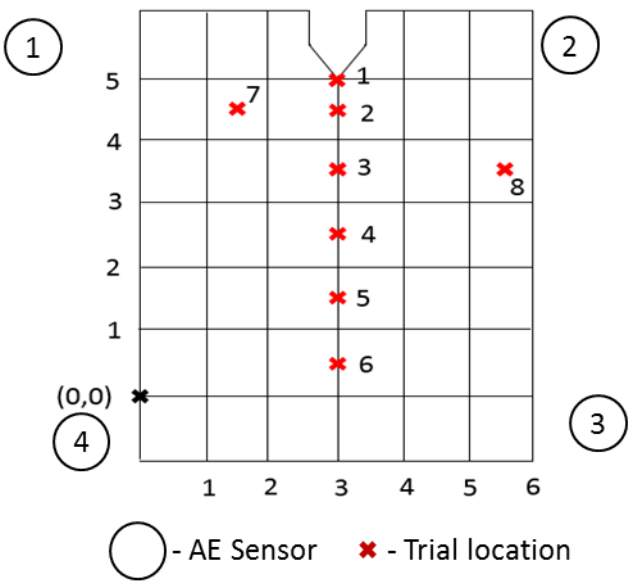


*Figure 5.4: Trial delta-T mapping locations*

*Figure 5.5: DIC Speckle pattern on surface of specimen*

### 5.2.2 Fatigue test

The unmodified end of the specimen was placed on a metal block and clamped firmly in place so that the modified, free end was suspended above the bed of the load machine, causing the specimen to act as a cantilever beam. When clamped, the specimen was positioned in such a way that the suspended end was situated underneath the actuator so that the actuator head could be lowered to make contact with the steel roller shown in Figure 5.3. Once the specimen was in place, the DIC cameras were positioned so that they captured the region of interest around the notch and were calibrated accordingly.

In order to develop a fatigue crack, the specimen was loaded cyclically from 0.5 to 11kN at a rate of 1Hz; the force was applied vertically downwards to the steel roller. Conventional AE hit activity was recorded for the entire duration of the experiment. As well as this, once every 200 cycles the AE acquisition system would trigger the collection of wavestream data for 1.5 seconds; wavestreams of this length were recorded in order that each wavestream record 1.5 loading cycles and hence would be guaranteed to record the peak load. It was desirable for the wavestreams to capture activity occurring during the peak load as it is at this point in the loading cycle that cracking and crack growth is expected to occur and hence it is the point of the loading cycle in which AE related to the damage process is most likely to be released. Once at the beginning of the test and subsequently every 200 cycles the cyclic loading regime was paused and the specimen was loaded to 11kN and held at that load whilst a DIC image was taken. The specimen was loaded for 67,099 cycles until a crack, visible to the naked eye, was present at the notch tip; at this point it was assumed that there would be sufficient data to conduct an analysis. For added clarity a photograph of the experimental setup is shown in Figure 5.6.

It should be noted that, due to slight eccentricity in the test set up, the roller travelled gradually during the loading cycles and so at several points during the experiment the loading regime was paused in order to allow for the roller to be repositioned. This happened at 10,561 s, 15,810 s, 20,381 s, 40,725 s and 61,044 s. Furthermore, at

approximately 16,000 s, the capture rate of the wavestreams and DIC images was reduced, from once every 200 cycles to once every 500 cycles, in order to reduce the quantity of data collected.

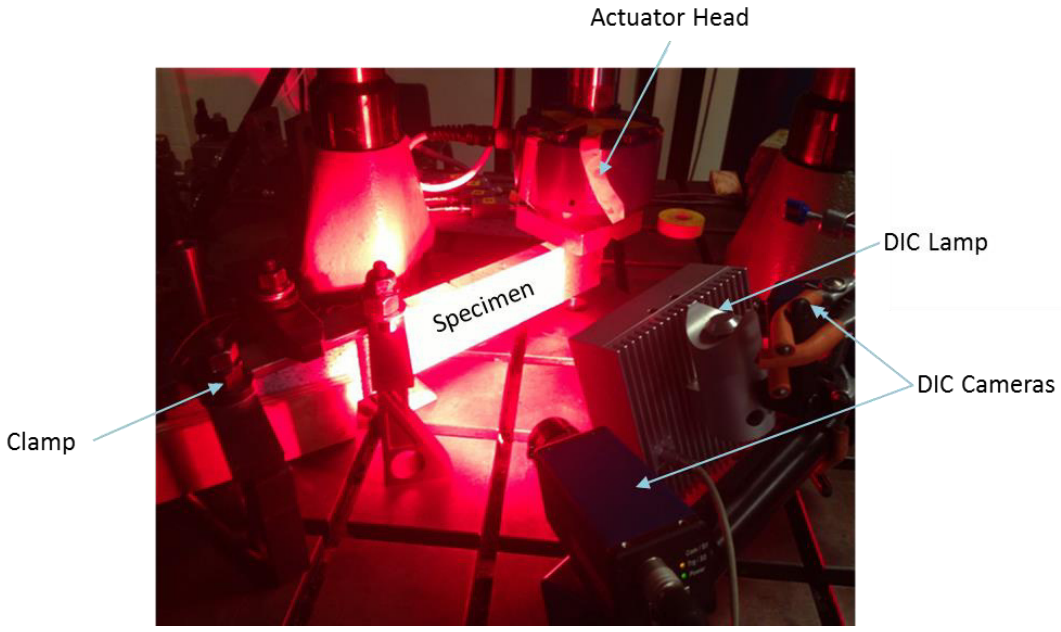


*Figure 5.6: DIC and specimen setup for loading*

## 5.3 Results and Discussion

### 5.3.1 DIC Results

The images taken using the DIC system were processed on the Istra4D software. An area of interest around the notch was selected and the images were correlated. Ten marker points were created around the notch area, Figure 5.7.

By tracking the positions of the points it was possible to calculate the distance between them and hence determine how this distance changed over the course of the experiment. The change in the distance between marker points (DBMP) either side of the notch is related to the opening of the crack, and hence crack growth rate. Figure 5.8 shows the change in the distance between the points 1 and 2.

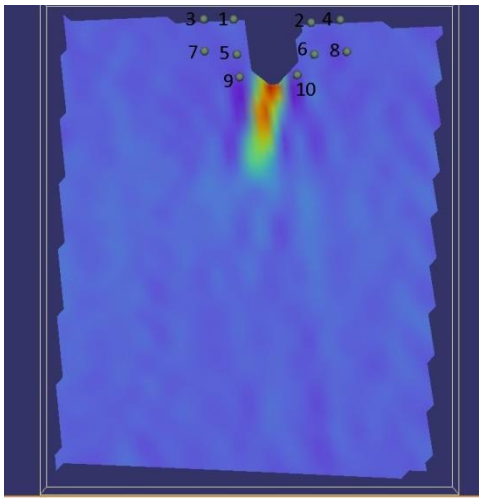


*Figure 5.7: Location of points investigated from DIC*

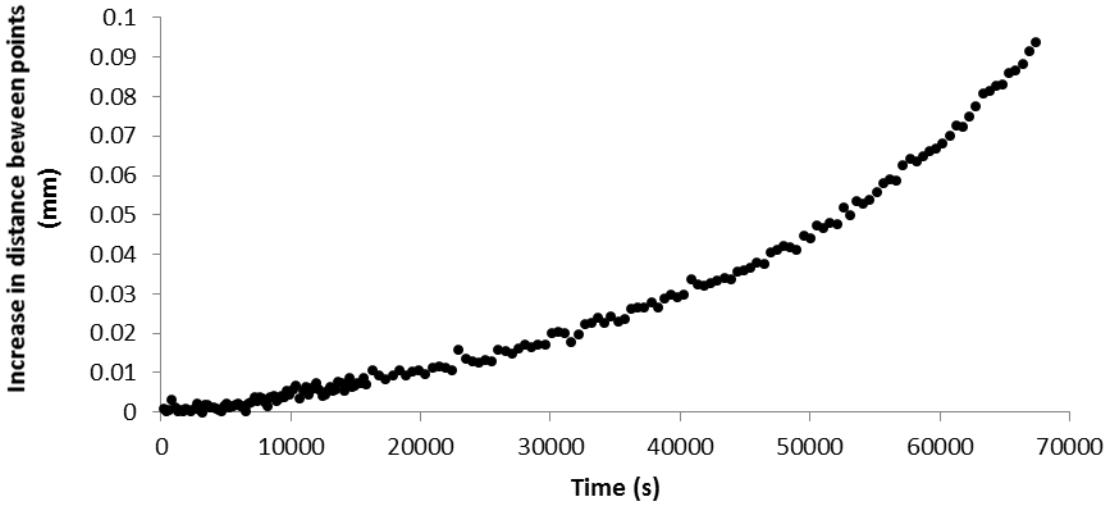


*Figure 5.8: Change in distance between marker points 1 and 2 over the course of the experiment*

As expected, the distance between the points increases as the test progresses, as a result of crack growth and deformation of the specimen. Furthermore, the rate at which the points move apart increases as the test goes on, which suggests that the rate of crack growth also increases as the test goes on. This agrees with the Paris Law, Equation 2-2, which states that crack growth is proportional to the stress intensity factor, which increases with crack length and applied stress.

In order to investigate the point at which the DIC results are capable of detecting the presence of cracking, the distance between marker points 1 and 2 was plotted for the initial portion of the test only, Figure 5.9.

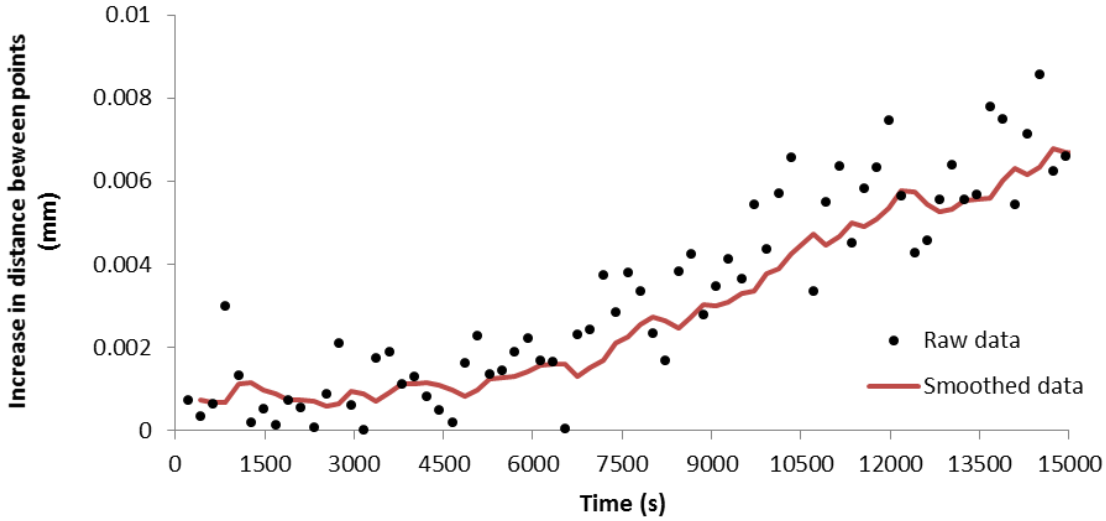


*Figure 5.9: Change in distance between marker points 1 and 2 at the beginning of the test*

The first thing apparent from this plot is the level of noise in the DIC data. Since each image is taken whilst the specimen is held at maximum load, 200 loading cycles after the last, it is expected that the two markers either side of the notch should either remain at the same distance (i.e. no crack growth) or move apart (crack growth); it is counterintuitive to assume that they would move closer together. The fact a number of data points in the plot shown in Figure 5.9 do indicate that the points get closer from one image to the next shows that there is noise in the DIC data. This noise is thought to result from a number of factors such as the electronic noise from the digital cameras and also slight variations in both the lighting and the load applied to the specimen when the images were taken. For this reason the data was smoothed using an exponential smoothing function in MS Excel to give the solid line seen in Figure 5.9. From the smoothed data it can be seen that there is a relatively steady distance between the two points either side of the notch until approximately 7385 seconds, at which time the gradient changes significantly, which suggests that there was an increase in crack growth rate at this time. In order to obtain an impression of the precision of the DIC

results, the mean and standard deviation of the increase in the distance between the two points were calculated using the data from 0 to 7000 seconds, i.e. before crack growth is conceivably detectible with the DIC system. These were found to be 0.0012mm and 0.00082mm respectively and thus the noise in the data in this region of the test is 70% of the mean value. For this reason it is expected that small variations in the crack growth rate will not be able to be identified using the DIC data as they will be drowned out by the noise, however the larger overall trends are still relevant and informative.

In order to investigate the effect of realigning the roller, the increase in the distance between two points either side of the notch around the times at which the roller was realigned were plotted, Figure 5.10. It is difficult to determine whether the DIC results show any correlation with the times at which the roller was realigned because of the noise in the data. Furthermore, the infrequency with which images were taken has resulted in the DIC results having a low time resolution and so it is possible that any effects caused by roller realignment have ceased to exist by the time at which the next image was taken.

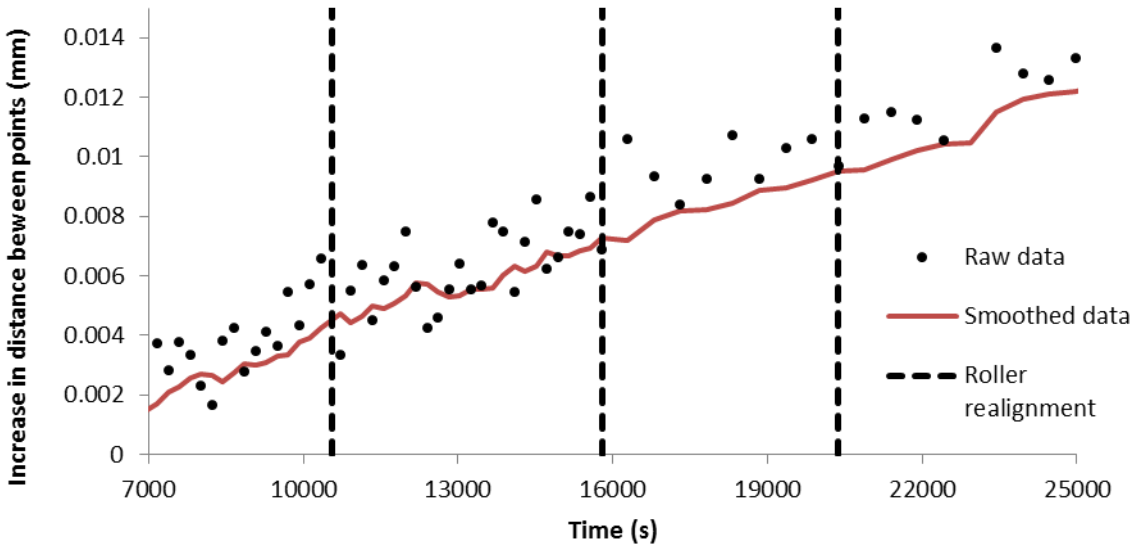


*Figure 5.10: Change in distance between marker points 1 and 2 after roller realignment*

### 5.3.2 Traditional AE Results

The traditional AE features; hits, energy and amplitude, were investigated, as shown in Figure 5.11, Figure 5.12 and Figure 5.13 respectively.

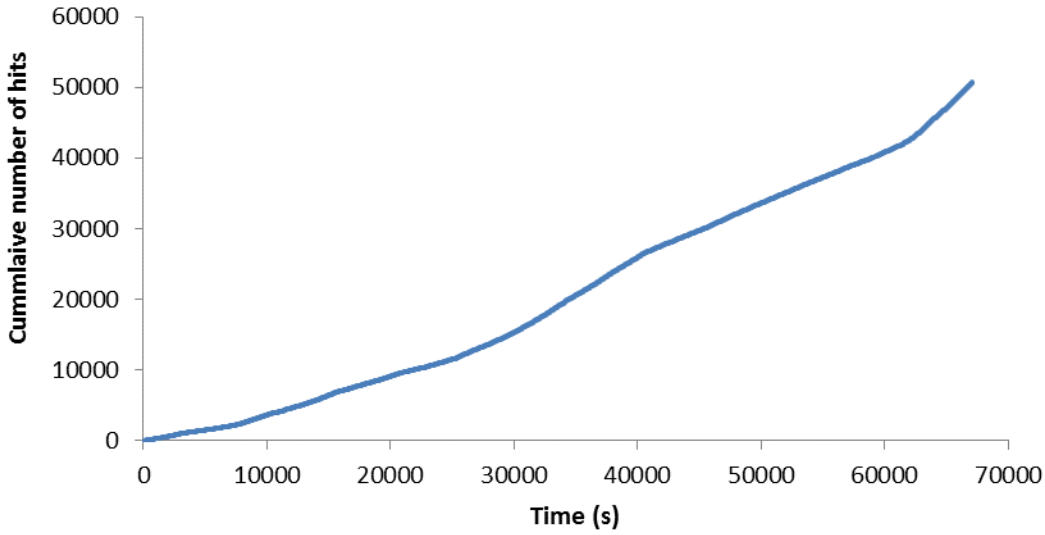


*Figure 5.11: Cumulative AE hits recorded by Channel 1 over the duration of the test*

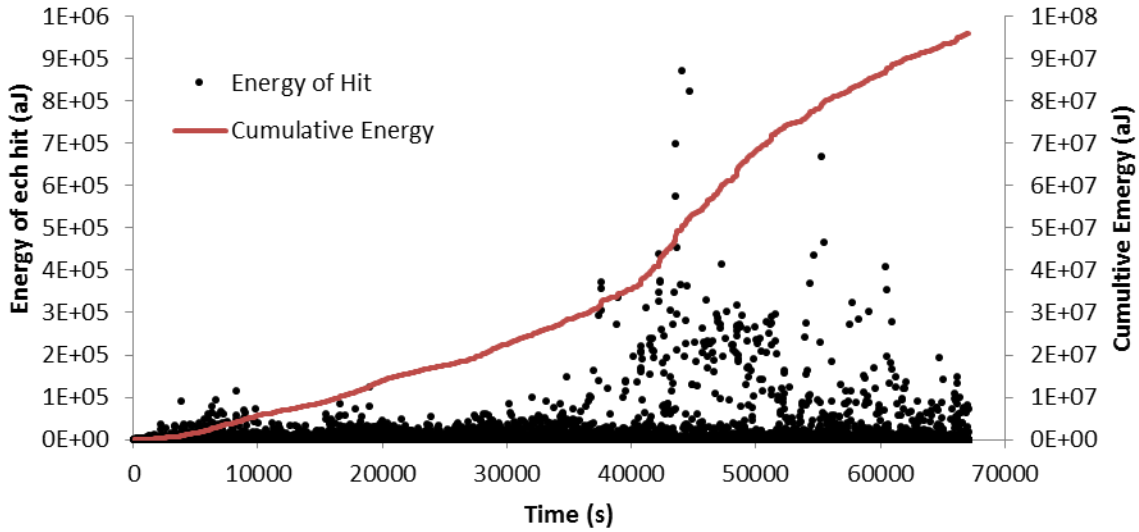


*Figure 5.12: Energy of each hit and cumulative energy of each hit recorded by Channel 1 over the duration of the test*

Figure 5.11 shows that the rate of AE activity, the rate at which hits are detected, increases at various points of the test and slows at others. It is expected that the regions of high release rate correlate to regions of high crack growth rate (Pullin et al. 2010). Figure 5.12 and Figure 5.13 show that there are more high energy, high amplitude hits

later on into the test, suggesting that there was a greater amount of crack growth rate as the test went on.

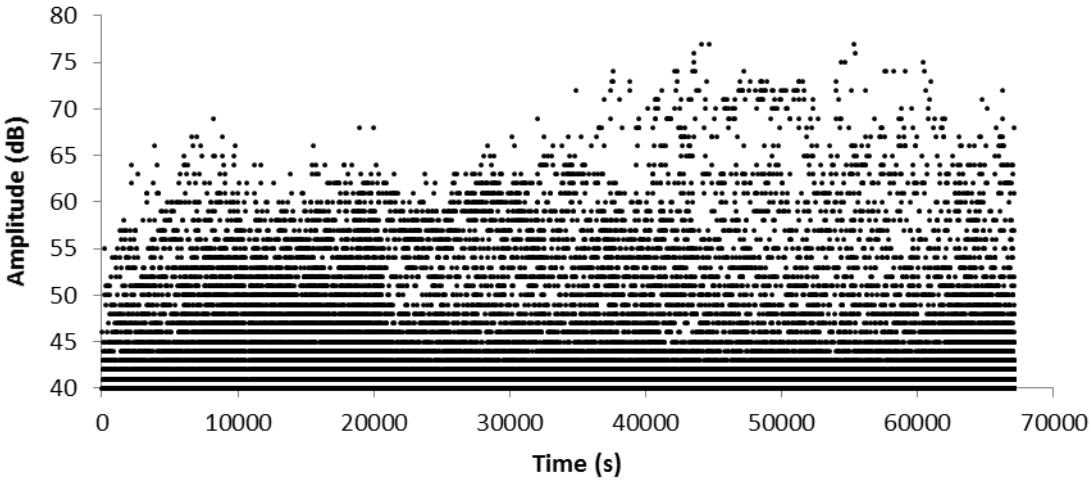


*Figure 5.13: Amplitude of each of the hits recorded by channel 1*

In order to investigate AE's capacity to detect cracking, the graph of cumulative hits, Figure 5.11 was scrutinised in closer detail, Figure 5.14, between 5,000 and 10,000 seconds.

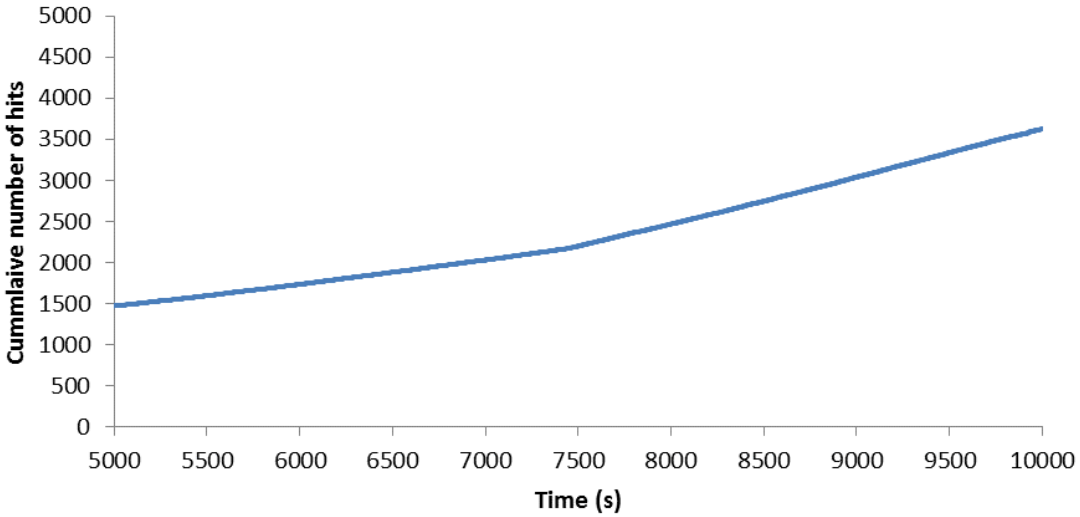


*Figure 5.14: The cumulative AE hits recorded by channel 1 around the time when cracking is thought to have begun according to DIC*

It can be seen that the gradient of the slope in Figure 5.14 changes at 7412 seconds. Something in the structure must have changed at that time to cause the increase in the rate of AE released, and based on the results of the DIC analysis it is apparent that this change in AE release rate can be attributed to increased crack growth activity.

In order to investigate the effects of stopping the test to reposition the roller, the rate of hits being recorded by channel 1 around the times at which the roller was repositioned was examined, Figure 5.15.

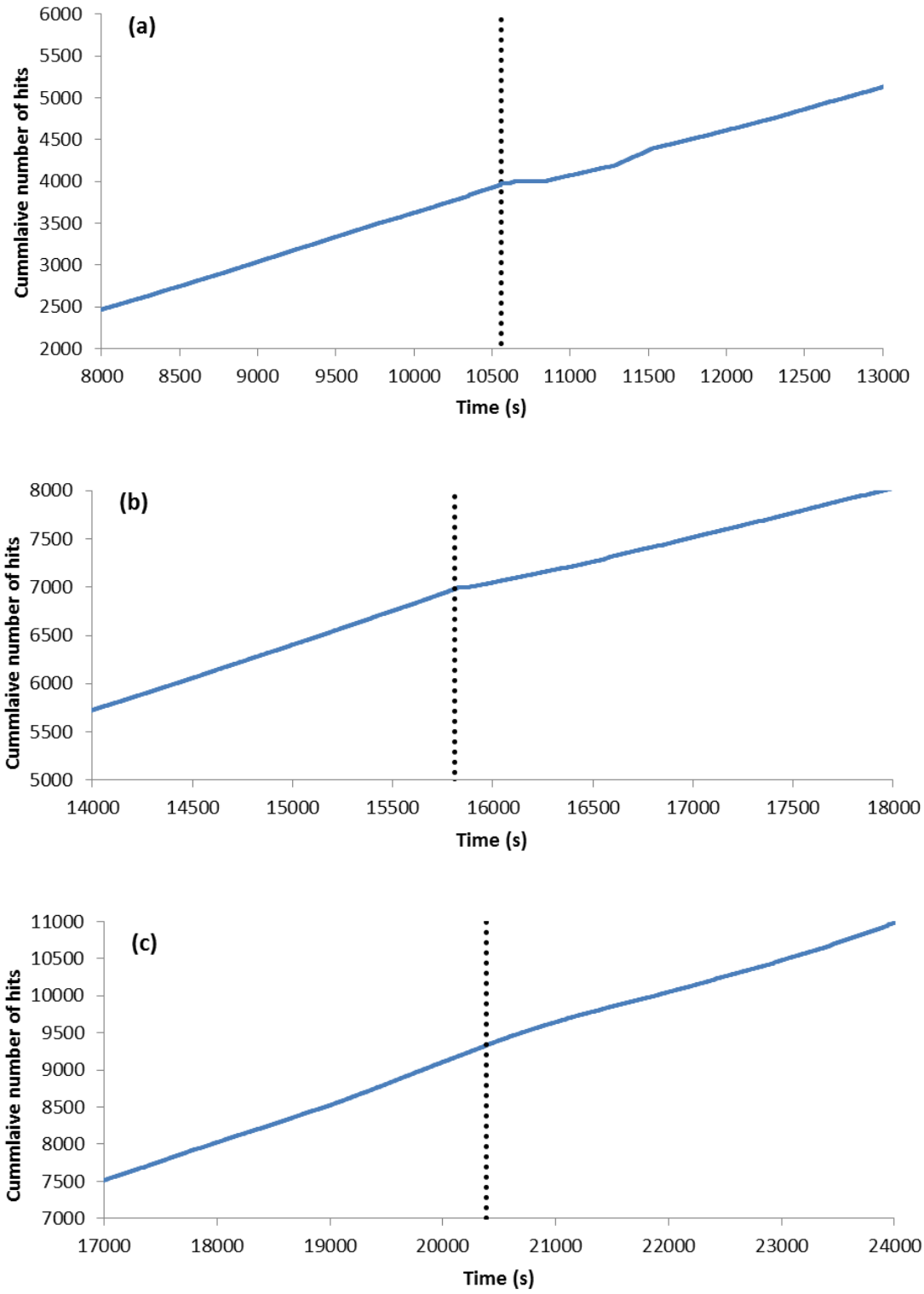

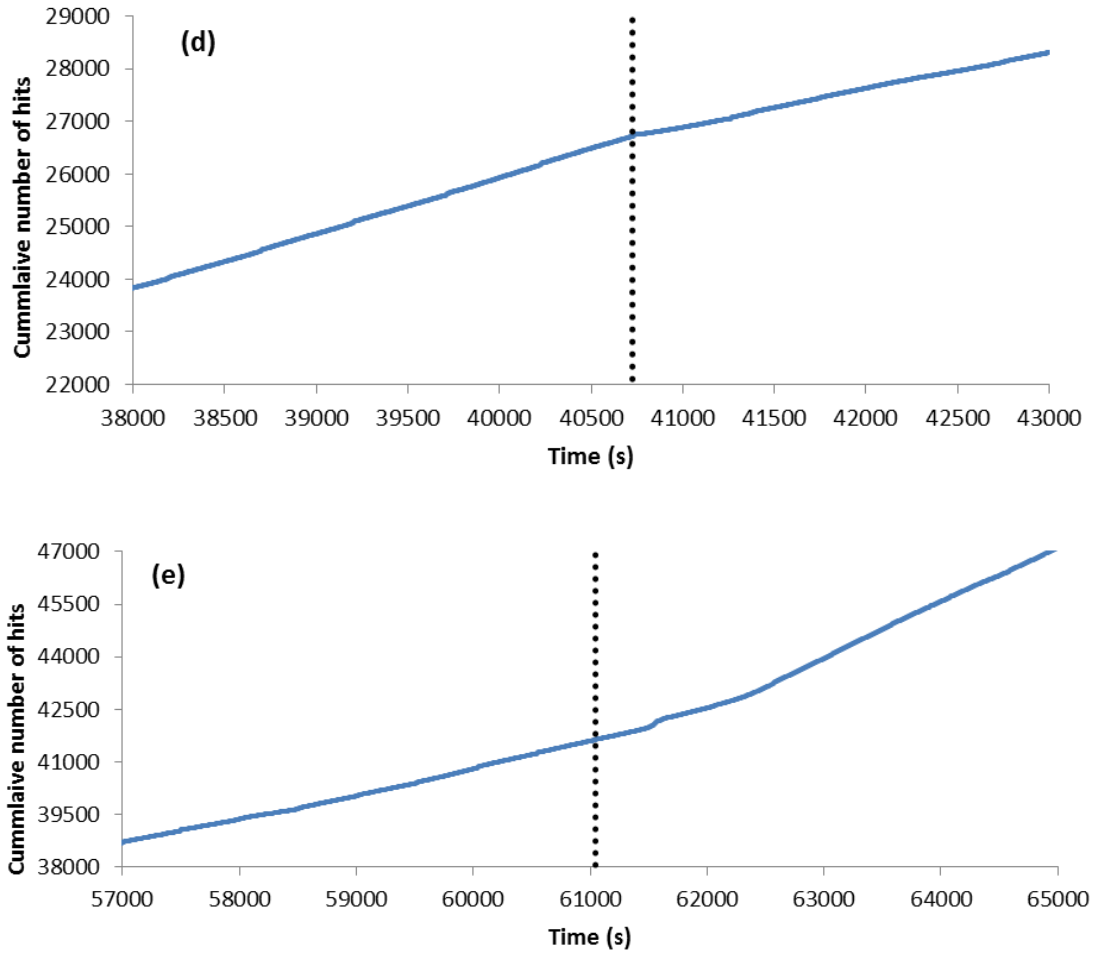


*Figure 5.15: Cumulative AE hits recorded by Channel 1 at the moments of the test when the roller was repositioned (a) 10,561 sec (b) 15,810 sec (c) 20,381 sec (d) 40725 sec and (e) 61044 sec*

Figure 5.15 shows that the repositioning of the roller did appear to have an effect on the rate of AE release. At 10,561, 15,810, 20,381 and 40725 seconds the rate of AE release can be seen to decrease momentarily before rising again suggesting that the crack growth rate decreased at these moments also. This is understandable since as the roller travelled it would exacerbate the amount of eccentric loading on the specimen, causing one side of the notch to experience a greater stress, and thus increasing crack growth rate. After the roller's position was reset, the level of this asymmetric loading would have decreased and hence the side with the specimen with the longest crack would experience a smaller stress that it had done before the realignment, and the crack growth rate would decelerate, resulting in less AE. It is also worth noting again that the crack growth mechanism itself is a delicate process, dependant on the movement of slip planes in the grains that lie in the region of high plastic deformation around the crack tip (Ritchie

1999). Each time that the roller was repositioned, this process was disrupted and the load orientation changed slightly which would reduce the crack growth rate.

### 5.3.3 AE Delta-T Location and Frequency Analysis

The AE data was processed using the bespoke *delta-T mapping* location program developed at Cardiff University in order to accurately calculate their location. For ease of comparison with the wavestream and AHA to follow, the data of the located waves was binned temporally using time steps the same magnitude as the time steps between the wavestream capture (every 210 seconds from 0 to 15,814 seconds and every 510 seconds thereafter). The number of located events in each time bin as well as the cumulative number of located events was then plotted, Figure 5.16.

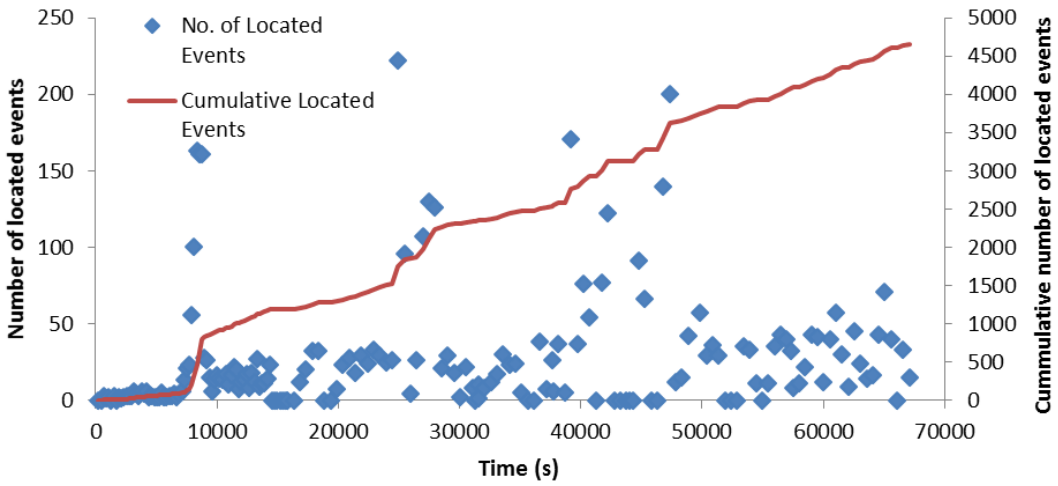


*Figure 5.16: Number of located events in each time step and cumulative number of located waves over the duration of the test*

The rate of occurrence of located events began to increase at approximately 7300 seconds indicating that this was the point at which the rate of crack growth first began to increase. Furthermore, Figure 5.17 shows that as well as the total number of events increasing after 7300 seconds, those events also started to originate from more specific regions, in the vicinity of the notch tip; whereas before that point in the test they had been evenly distributed all over the monitored region. This suggests further that there was an increase in crack growth rate at this time. From the combined information in the above

analysis techniques it can be said, beyond reasonable doubt, that the crack growth rate in the specimen first began to increase significantly at approximately 7300 seconds.

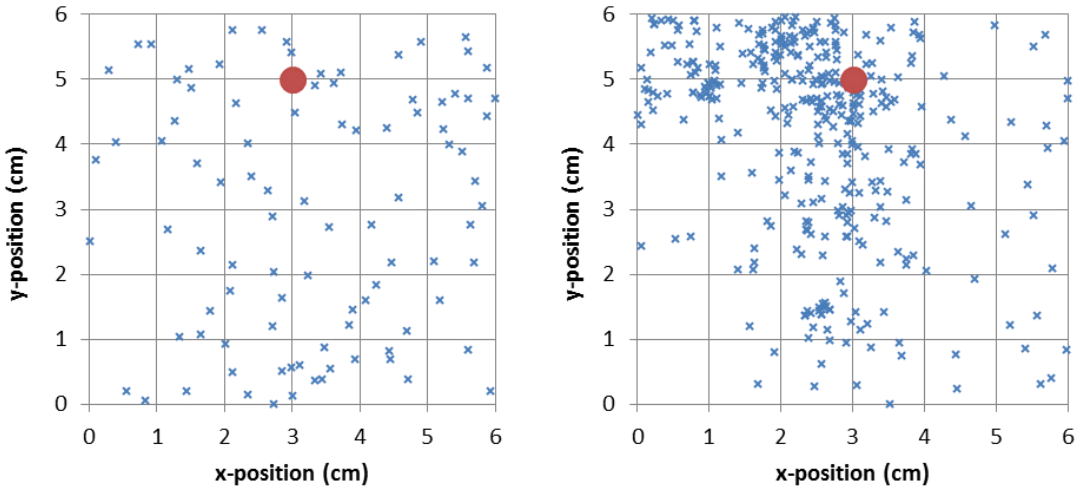


*Figure 5.17: Locations of events calculated using delta-T mapping between (a) 0 and 7000 seconds and (b) 7300 to 8350 seconds*

Several large amplitude events recorded by channel 1 over the course of the test in the vicinity of the notch tip were selected for further analysis, Table 5.3. Large amplitude events were chosen because crack growth related mechanisms are more likely to release large amplitude AE; and events located as originating from the notch region were selected in order to further increase the likelihood that the hits analysed were associated to the cracking process. The waveforms of these hits were imported to Matlab and analysed using a Fast Fourier Transform to inspect the frequency spectrum, Figure 5.18, Figure 5.19, Figure 5.21 and Figure 5.22. Since the first arrival of the wave is the portion of the waveform which is most representative of the source mechanism which released that AE (the tail end of a waveform often contains reflections and sensor ring-down); the first arrival of each of the five selected hits was analysed in more detail.

*Table 5.3: High amplitude events selected for frequency analysis from CH1*

| Index | Time (s) | Amplitude (dB) | x,y Location (cm) |
|---|---|---|---|
| 1 | **8,071** | 59 | 3.02, 4.84 |
| 2 | **8,345** | 62 | 3.40, 5.00 |
| 3 | **10,031** | 88 | 2.81, 4.99 |
| 4 | **60,439** | 67 | 2.65, 4.91 |
| 5 | **65,440** | 67 | 3.00, 4.70 |

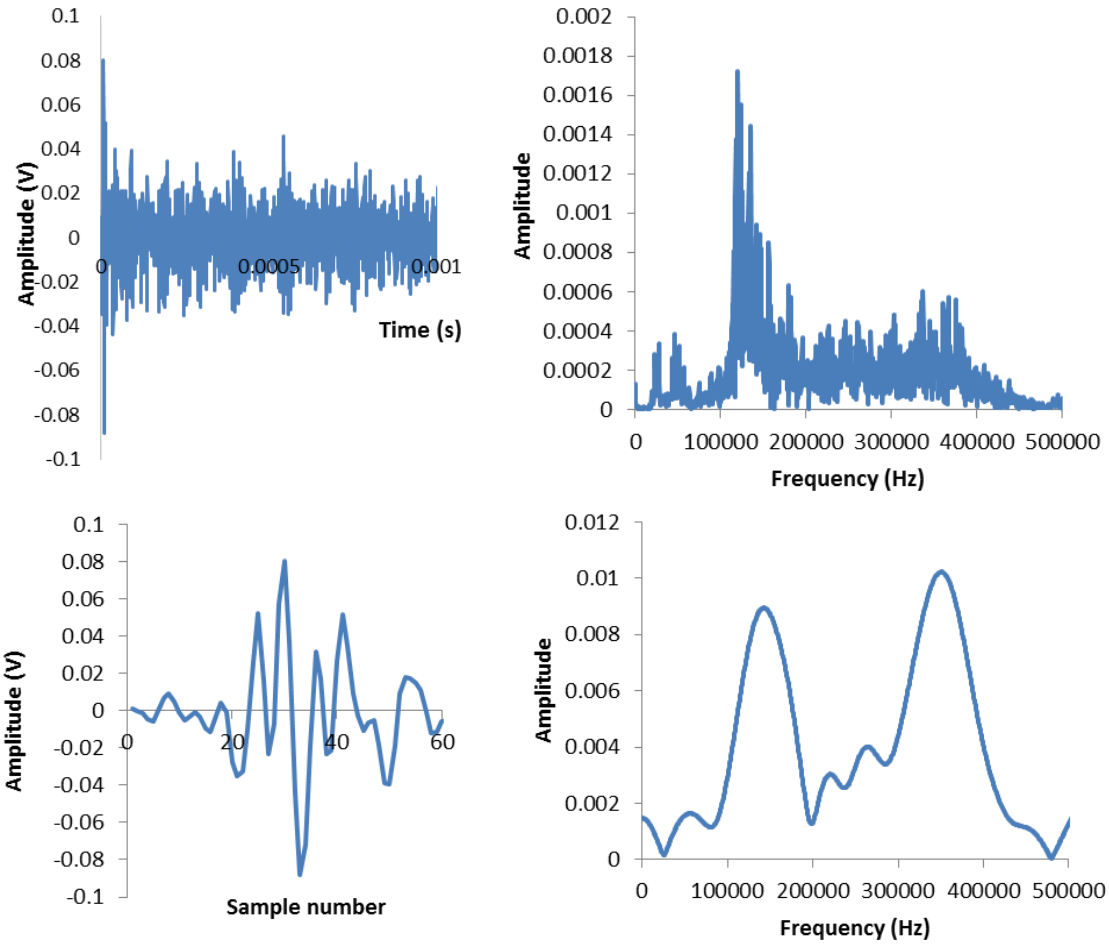


*Figure 5.18: Wave index 1 at 8071 seconds, amplitude of 59dB*

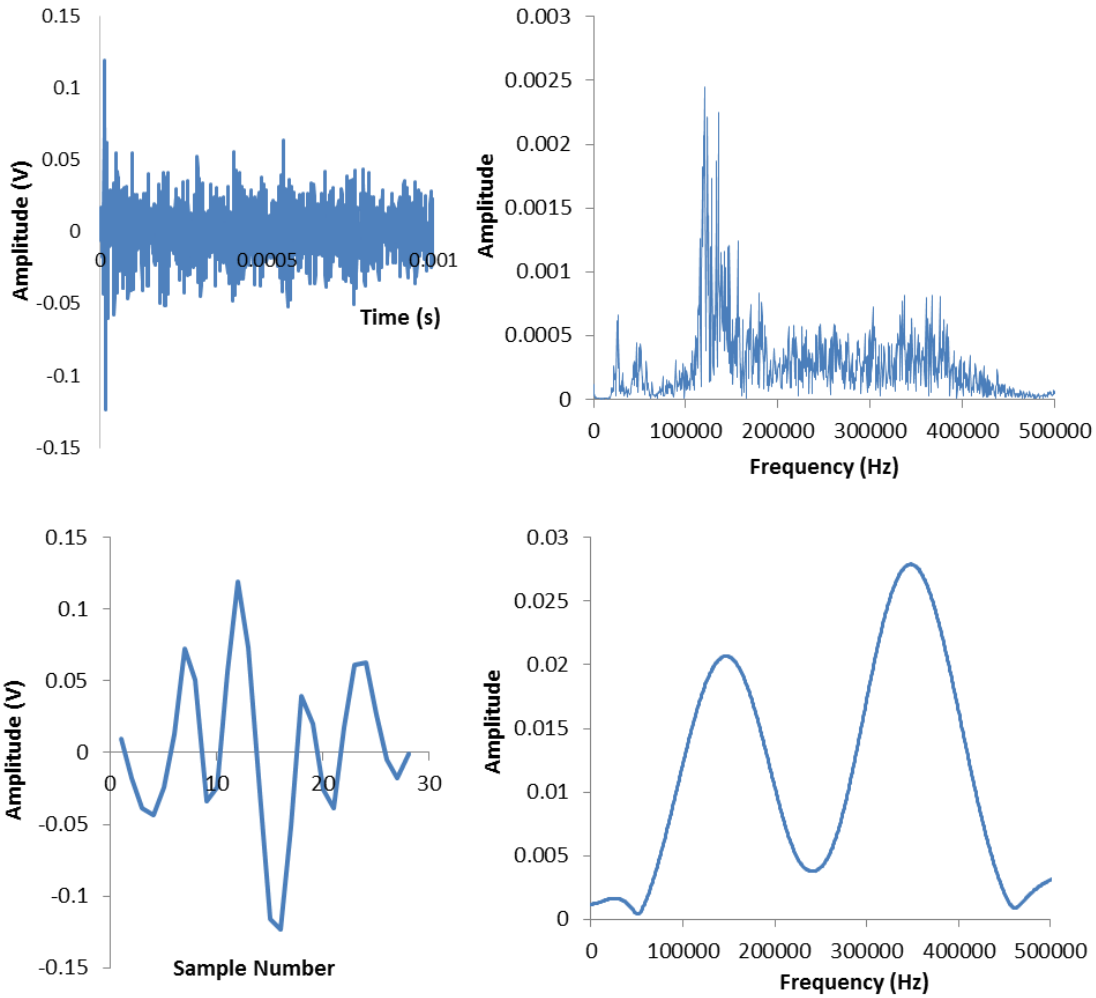


*Figure 5.19: Wave index 2 at 8345 seconds, amplitude of 62dB*

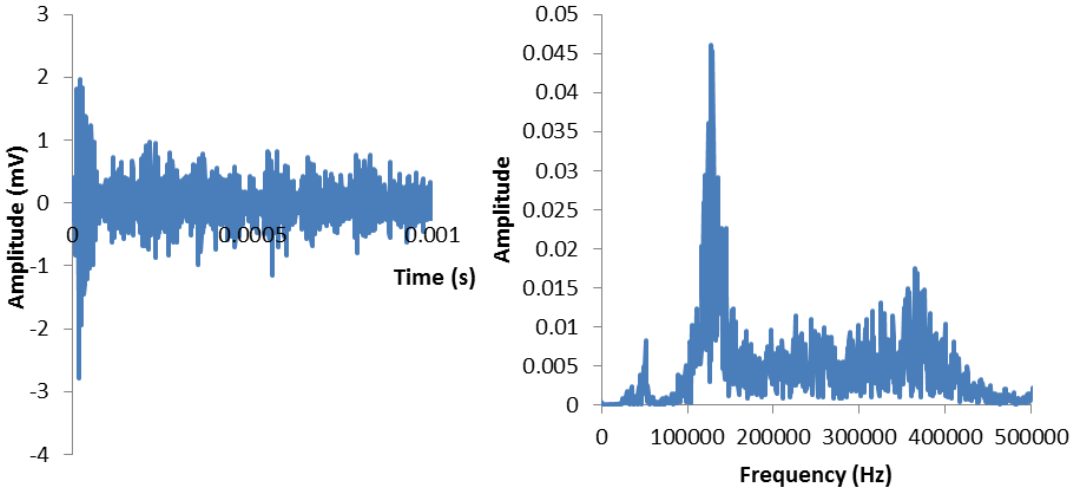

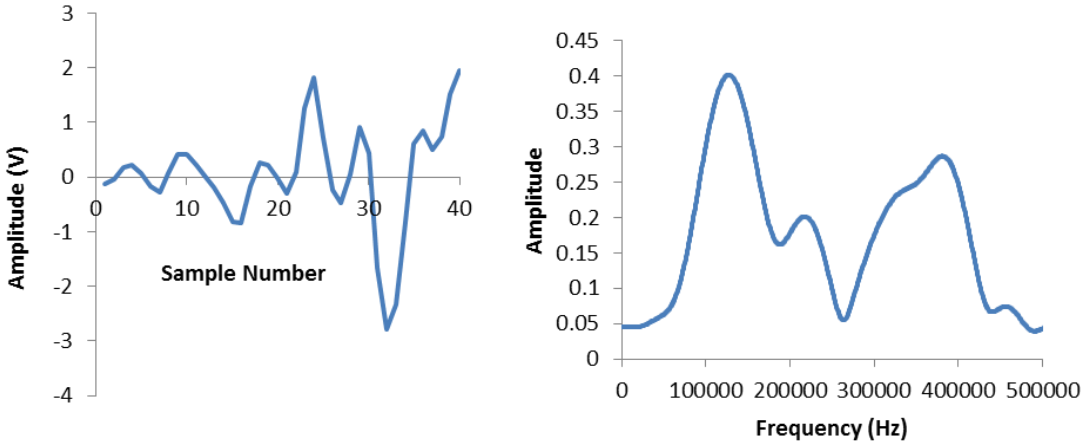


*Figure 5.20: Wave index 3 at 10,031 seconds with an amplitude of 88dB*

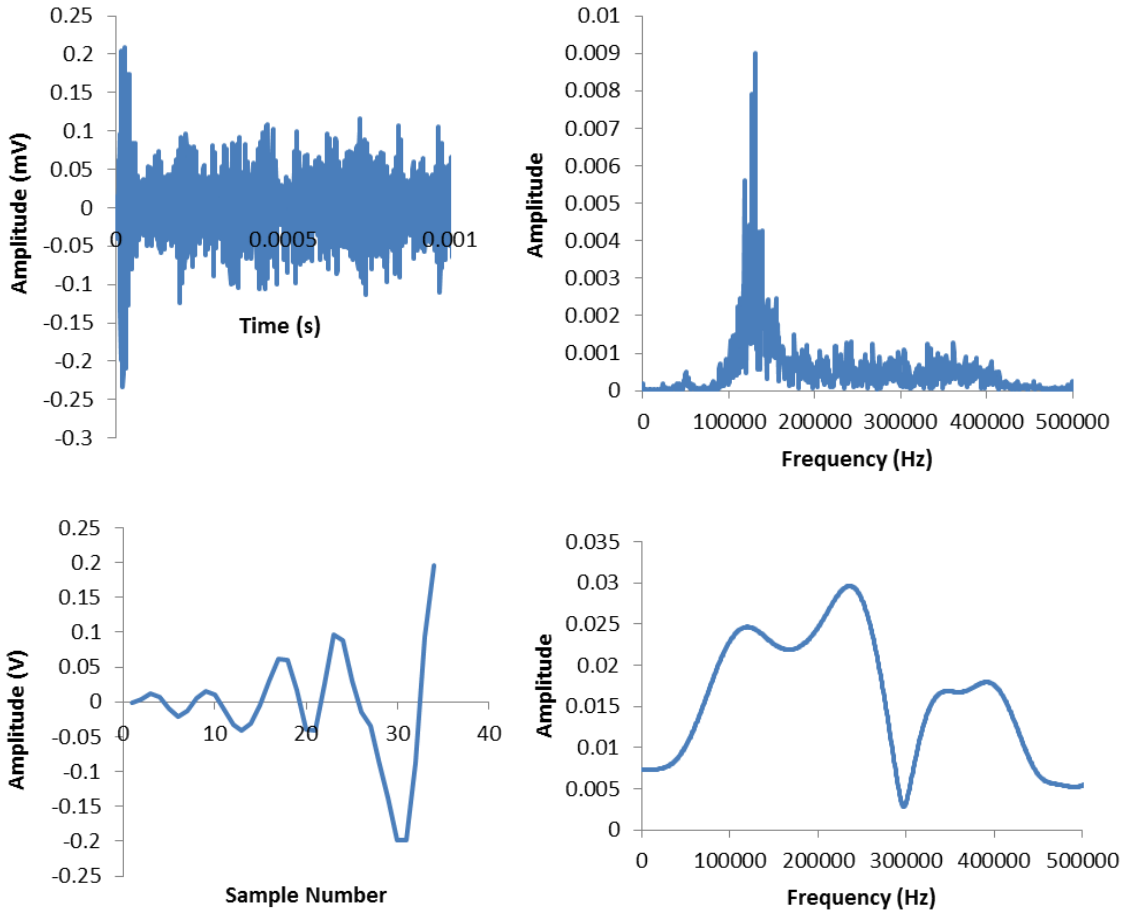


*Figure 5.21: Wave index 4 at 60,439 seconds with an amplitude of 67dB*

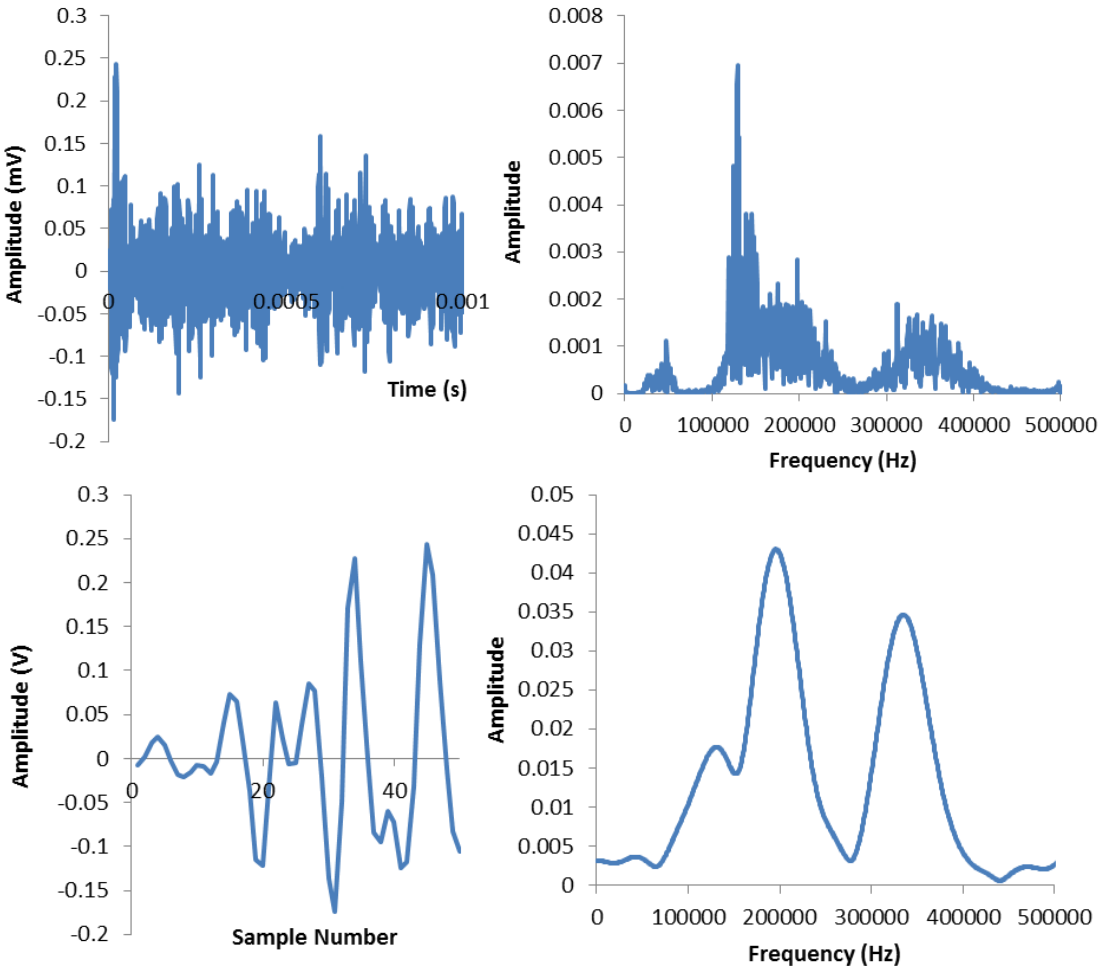


*Figure 5.22: Wave index 5 at 65,440 seconds with an amplitude of 67dB*

From the figures it can be seen that the most dominant frequency for any of the entire signals is approximately 130kHz, however when only the first arrival of the recorded wave is examined, frequencies around the 350kHz region are more prominent. Owing to the fact that these hits were all located as originating from the notched region, and they all had substantial amplitudes, it can be hypothesised that these hits were released by a crack growth related mechanism, and thus the frequency band of highest relevance to detecting cracking process is the band with a peak frequency at approximately 350kHz.

### 5.3.4 Conventional Wavestreaming

The wavestreaming data collected throughout the test was analysed using conventional wavestream analysis techniques, such as those presented by Pullin et at (2013). The root mean square (RMS) value of each wavestream was calculated and plotted, Figure

5.23. It is evident that the RMS of the wavestreams was larger at the tail end of the test indicating that there were more and/or higher amplitude transient signals contained within these waveforms and thus suggesting greater rates of crack growth as the test goes on. There is also an indication within the data that the RMS of the wavestreams was affected by the roller realignment; the RMS can be seen to noticeably drop just after the roller realignment at 10,561, 15,810 and 20,381 seconds. The RMS amplitude did not begin to increase substantially until 8764 seconds into the test, suggesting that this is the point at which crack growth rate began to increase, which is significantly later than the times predicted with previous analysis methods.

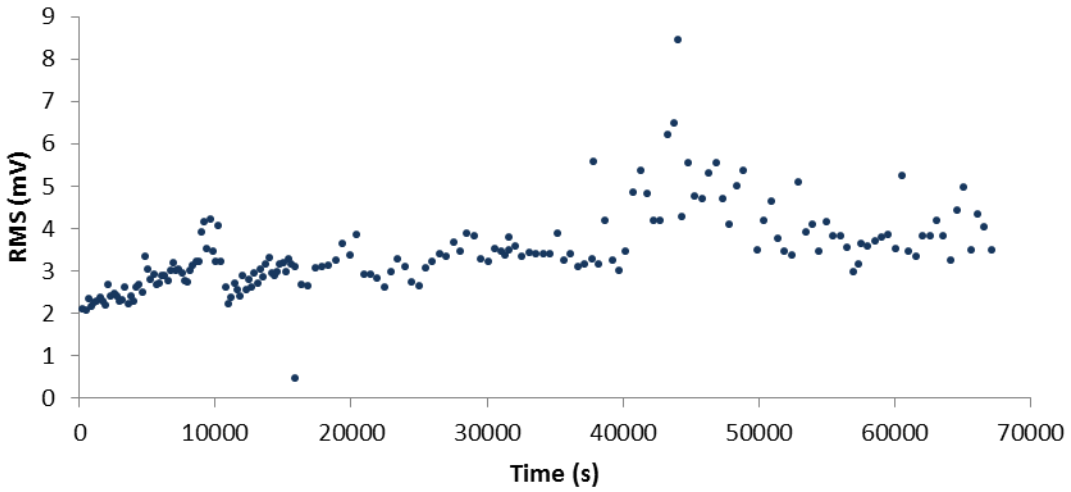


*Figure 5.23: RMS of each wavestream recorded on Channel 1*

The frequency spectrum of two of the wavestreams was calculated; one from the beginning of the test at 458 seconds, when there is believed to be relatively little crack growth, and one from further on in the test during the region of largest RMSs calculated, at 47,800 seconds, Figure 5.24.

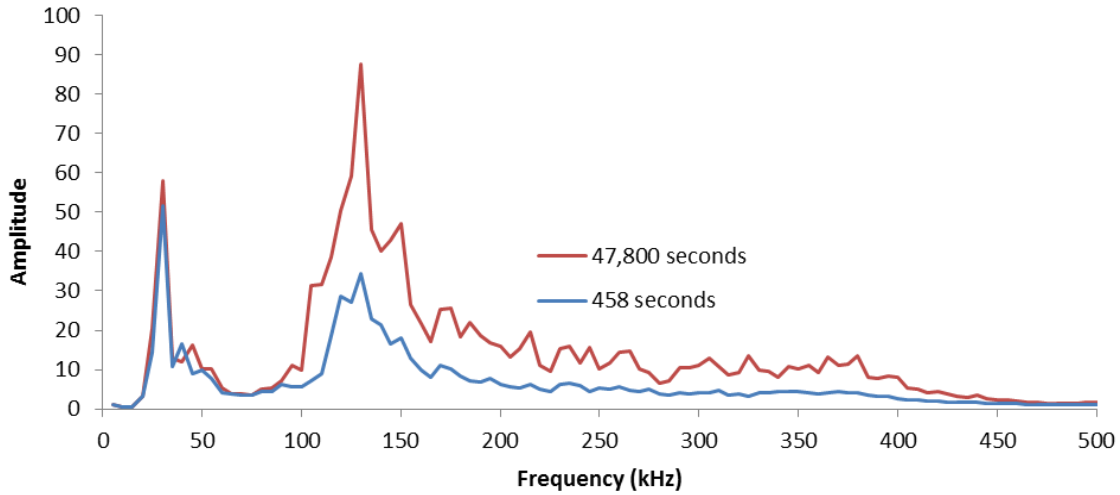


*Figure 5.24: Frequency spectra of wavestreams recorded at 458 and 47,800 seconds*

Since it has been theorised that there was relatively little crack growth occurring at 458 seconds into the test, the wavestream recorded at this time is likely to contain signals which are predominantly due to noise sources, such as friction and electrical noise. If this is the case then the frequency spectra of this wavestream would be the frequency spectra of those noise sources, reflections as well as the resonant frequency of the recording sensor. The wavestream recorded at 458 seconds was found to contain dominant frequencies at 30 and 130 kHz. Due to the cyclic loading regime it is likely that the noise sources present will be fairly constant throughout the test. Since crack growth rates are thought to be much larger by 47,800 seconds into the test, the frequency spectra of the wavestream recorded at this time should contain more frequency content related to the cracking process. Figure 5.24 shows that the dominant frequencies of the wavestream recorded at 47,800 seconds match those of the wavestream recorded at 458 seconds. The magnitude of 30 kHz spike is of the same order in both wavestreams and so is likely solely due to noise. The frequency spike at 130kHz is significantly larger in the wavestream recorded at 47,800 seconds, however it is believed that this 130kHz frequency spike is the resonant frequency of this the CH1 sensor and hence the reason that the amplitude of this frequency is larger in the wavestream recorded at 47,800 seconds is because there is more AE released during this time, due to the cracking process, and any excitation to the sensor will inevitably cause it to vibrate at its resonant frequency.

Other than the difference in the relative magnitudes of the 30 and 130 kHz frequency peaks, there is little difference in the shape of the spectra of the two wavestreams shown in Figure 5.25. There is no pronounced peak in frequency at 350kHz, i.e. the frequency suggested to be attributed to the cracking process, however this may be due to the fact that the signals from cracking are so brief that their impact on the frequency spectrum is drowned out by the noise, as demonstrated in Figure 5.1. In order to investigate further, the activity 350kHz frequency band over the duration of the experiment it was plotted, Figure 5.25. Also shown in Figure 5.25 is the RMS of each wavestream in order to discern weather the 350kHz frequency band displays any specific trends above and beyond that of the overall activity.

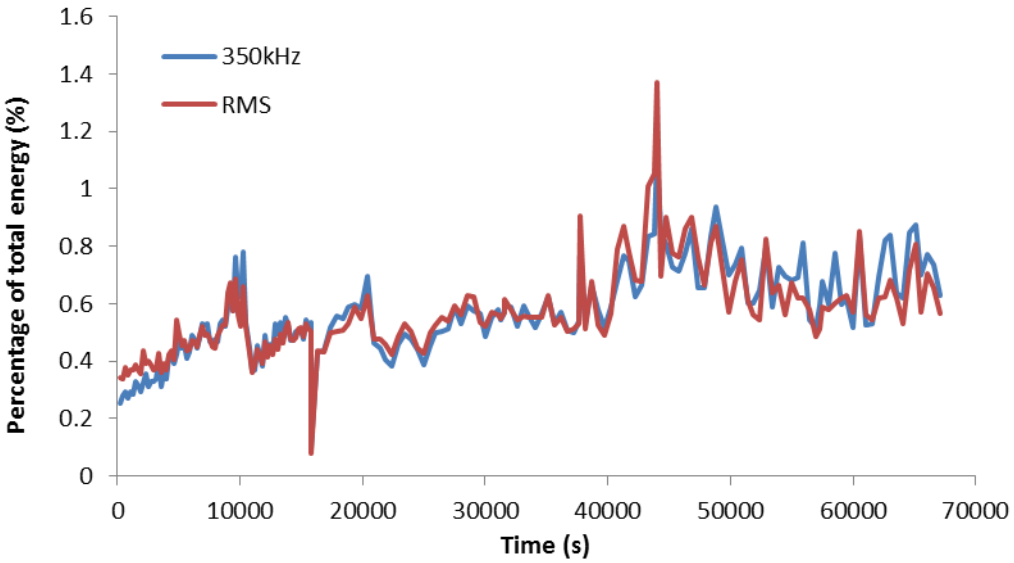


*Figure 5.25: Percentage of total energy contained in the 350kHz frequency band and RMS for each wavestream recorded*

It is apparent that, for the most part, the activity of the 350kHz frequency band matches the overall trends in the RMS of each wavestream. However, less of the overall energy of the 350kHz band occurs during the initial 6000 seconds of the test, before cracking is expected to have begun, and more of the overall energy occurs during the final 13,000 seconds of the test, when the crack growth rate would have been at its largest, and thus it is possible to say that the 350kHz band may be linked to crack growth and that tracking its progress may provide additional indication of the progression of cracking in the specimen.

### 5.3.5 Additive Hits Analysis

An Additive Hits Analysis, as described in Section 5.1, was conducted on the data. The proposal for the AHA technique is that it can be implemented in real-time, as the AE data is being recorded. However, as this facility was not available, it was conducted via post processing to provide a proof of concept. Unlike conventional wavestream recording, it is possible to know the number of hits contained within each additive hits data set during capture and so this can be plotted, Figure 5.26. The number of hits in each additive hits data set can be seen to increase as the test progresses, as would be expected to happen as damage develops in the specimen since crack growth acceleration has been previously linked with increasing rates of AE release. An advantage of viewing the data in this way is the ability to detect more clearly changes in the AE release rate. After an initial 'bedding in' period, in which the number of hits can be seen to fluctuate, the number of hits in each additive hits data set stabilises. At 7310 seconds, the number of hits begins to rise sharply and consistently, suggesting that a dramatic increase in crack growth rate occurred at this time.

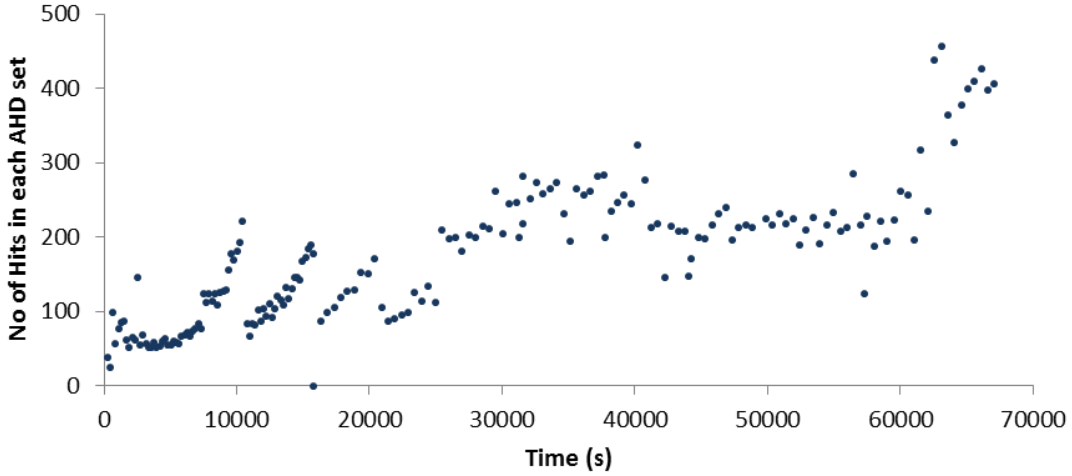


*Figure 5.26: Number of hits recorded in each AHD package*

The Also clearly visible in the graph at 10,561, 15,810 and 20,381 seconds are the periods of crack growth arrest due to the realignment of the roller. Figure 5.27 shows the RMS of each additive hits data set and indicates that larger RMS value additive hits data sets are observed towards the end of the test. Similar to the number of hit in each set,

the RMS also highlights a change in behaviour at 10,561, 15,810 and 20,381 seconds correlating to the points at which the roller was realigned.

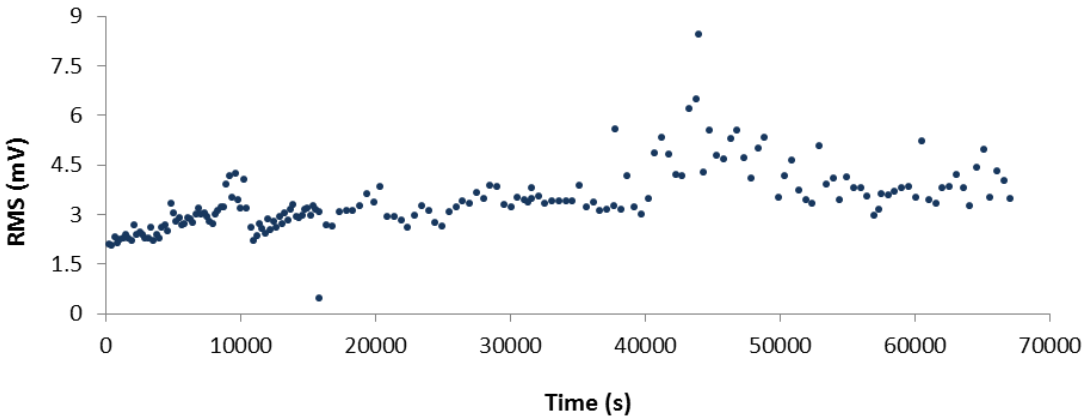


*Figure 5.27: RMS value of AHA data at each time step*

In order to allow for a coherent comparison between the results of the wavestream data and additive hits data the frequency spectra of two additive hits data sets were calculated from 458 and 47,800 seconds, Figure 5.28.

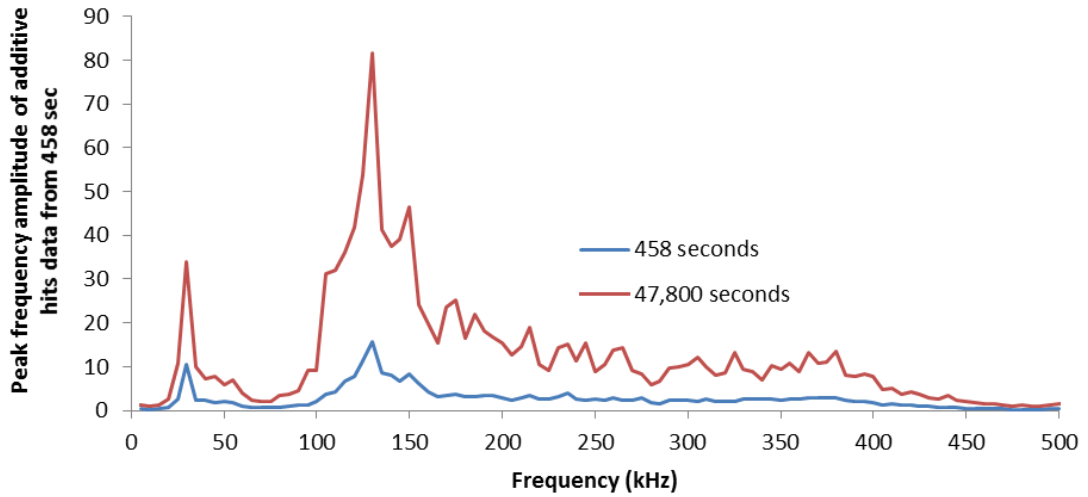


*Figure 5.28: Frequency spectra of additive hits data sets recorded at 458 seconds and 47,800 seconds*

Figure 5.28 shows that, unlike when the comparison was made between the wavestreams recorded a these times in Figure 5.24, the amplitude of the noise peak frequency at 30kHz is substantially lower in the additive hits data set recorded at 458 seconds than it is in the additive hits data set recorded at 47,800 seconds. This is because, unlike in conventional wavestreaming which records for the same length of time at each measurement regardless of whether or not there is any AE activity, the

additive hits data only consists of AE activity of sufficient amplitude and so the vast periods of noise between transient AE events are ignored and less noise is captured.

However, as with the conventional wavestraming results, Figure 5.29 shows that the 350Hz frequency band does not show any discernible trends when compared to the level of the RMS of each additive hits data set. The only noticeable difference between the activity of the 350kHz band and the RMS is during the final 13,000 seconds of the experiment where the 350 kHz band can be seen to exhibit a larger percentage of its total energy relative to the RMS.

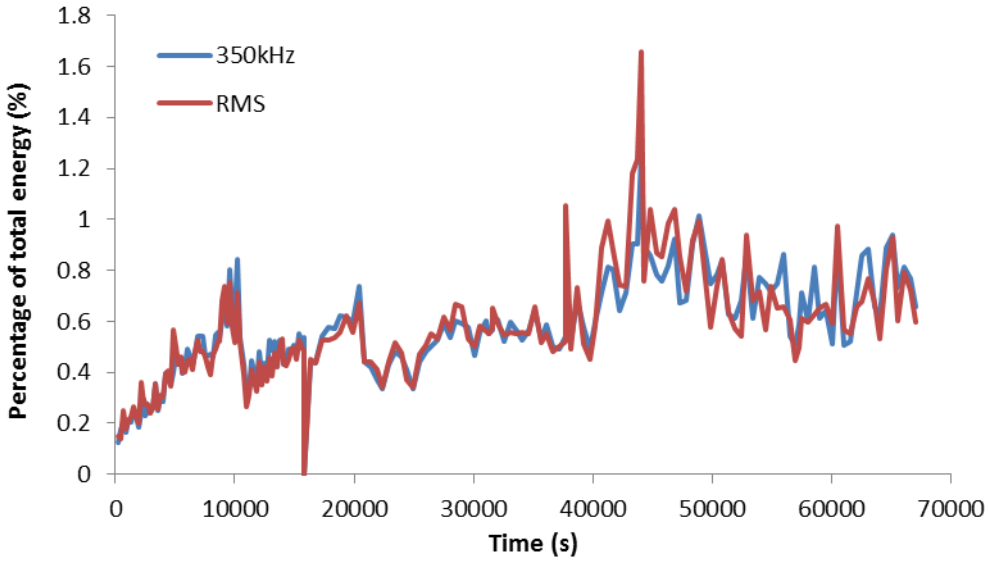


*Figure 5.29: Percentage of total energy contained in the 350kHz frequency band and RMS for each additive hits data set*

### 5.3.6 Comparison of Wavestream and Additive Hits Analysis Results

For ease of comparison of the frequency content recorded by each technique, a 3D plot of the binned frequency spectra of each can be seen in Figure 5.30. It can be seen that the two recording techniques produce very similar frequency spectra across the entire duration of the test. One notable difference is that the wavestream data consistently contains a lot more energy in the 30kHz frequency band than found in the AHA; a band previously identified as being noise. In some instances the peak amplitude of this 30kHz frequency band is actually larger than any other would skew analysis techniques which relied on monitoring or investigating the peak amplitude frequency band. The 350kHz

frequency band, which is believed to be associated with the cracking process, does not appear to be particularly prominent in the plots of either technique, at any stage of the test. However, this is understandable since, as observed in Figure 5.18 to Figure 5.22, when the frequency of an entire hit was examined, the frequencies due to the first arrival of the way were all but drowned out by the resonant frequency of the sensor and so it would be difficult to track subtle changes in its level of activity in comparison to the entire activity in a plot such as this.

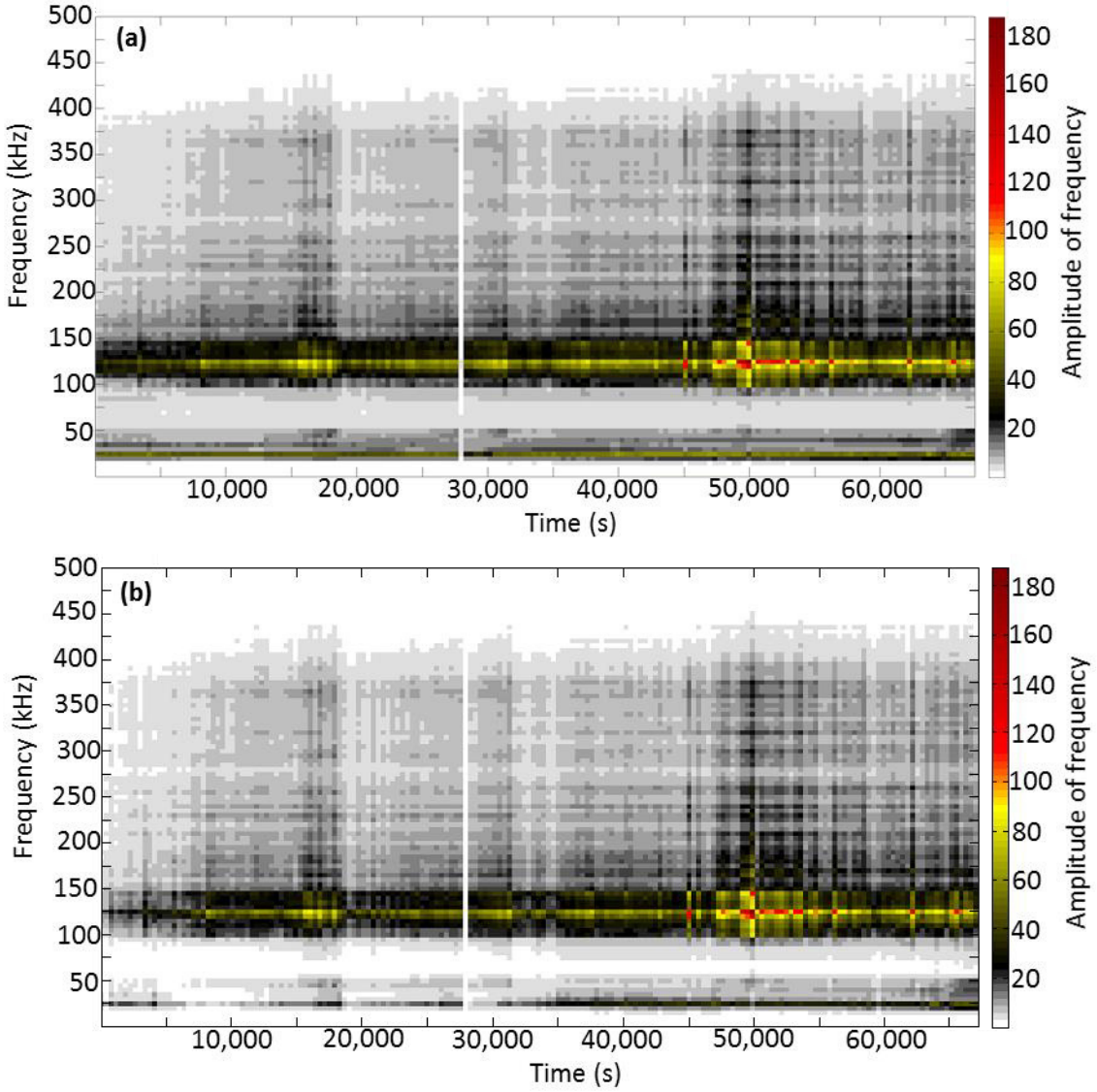


*Figure 5.30: Development of frequency spectrum with time for (a) conventionally recorded wavestream data (b) additive hits analysis*

The trends in the RMS vales of the additive hits data and conventional wavestreaming data are also very similar, as observed in Figure 5.31. The additive hits data has a consistently higher amplitude RMS due to the fact that there is less noise in each data set to dilute the amplitude.

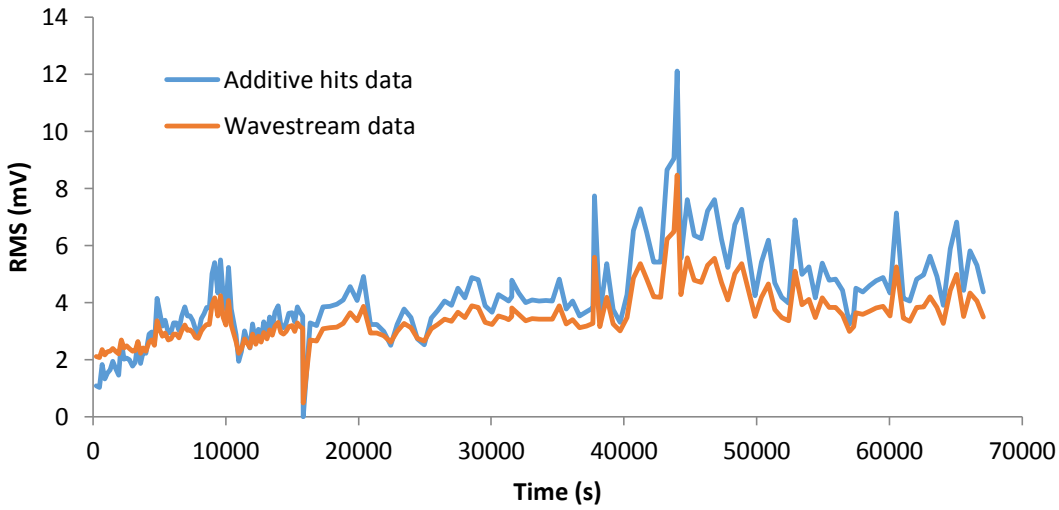


*Figure 5.31: Comparison of RMS values of conventional wavestreams and AHA data*

Finally, the average additive hits data set is 525,857 data points long, whereas each and every conventional wavestream is 3,000,306 data points long meaning that, on average, the additive hits data is just 17.5% of the length of the conventional wavestream. This reduction in data size would provide a saving on the amount of data storage needed and power required to transfer that data.

## 5.4 Conclusions

A pre-notched, rectangular cross-sectioned, aerospace grade steel bar was cantilevered and subjected to a 1Hz cyclic loading regime between 0.5 and 11 kN. The test lasted for 67,099 seconds during which time the specimen was monitored for damage by DIC and AE techniques. The DIC results predicted that the first significant increase in the crack growth rate occurred at approximately 7385 seconds, however the data has low time resolution and a significant degree of noise. Conventional AE analysis techniques, consisting of tracking the hit release rate, energy and amplitude, indicated the first large increase in crack growth rate at 7412 seconds. The rise in the rate of located AE events

around the notch region suggested that the first substantial increase in crack growth rate occurred at 7300 seconds, though this was also performed with a low time resolution. It was more difficult to discern changes to the crack growth rate during the beginning of the test from the wavestream results, however a plot of the RMS displayed a sharp rise at 8764 seconds which could be used as an indicator. Conversely, the ability to plot the number of hits in each additive hits data set allowed the increase in crack growth rate to be determined more easily for the Additive Hits Analysis, which identified the first significant increase in crack growth rate at a time of 7310 seconds, which matches more closely the results of the other techniques/monitoring methods.

Closer investigation of the times corresponding to when the roller was repositioned showed that the crack growth rate reduced after repositioning took place, at 10,561, 15,810 and 20,381 seconds. All AE analyses were able to distinguish these points of the test though the low time resolution and level of noise in the DIC recording meant that the period of reduced crack growth was indistinguishable.

A number of high amplitude hits located as originating from the notch tip region were analysed to identify the frequency components which could be associated to the cracking process; the 350kHz band was acknowledged. Subsequently, the cumulative energy of this frequency band was plotted for the duration of the test for both the wavestream and additive hits data in an attempt to track crack growth though the trends seen in these plots did not differ drastically from the simple RMS plots of each of the analysis techniques respectively.

For the most part, the results of the *Additive Hits Analysis* matched those of the wavestream analysis with regards to tracking the progression of damage in the specimen. However, the additive hits data sets were, on average, just 17.5% of the size of the wavestream data sets and recorded less noise recorded which resulted in less ambiguity and disruption in the frequency content plot. Furthermore, it was simpler to identify the onset of changes to the crack growth rate from the additive hits data than

from the wavestream data. Thus the AHA offers a number of improvements over conventional wavestreaming approaches whilst not compromising the effectiveness of the analysis.

# 6 Automated Corrected Measured Amplitude Ratio

Measured Amplitude Ratio (MAR) is a characterisation method which uses the relative amplitudes of the two Lamb wave modes (extensional, $S_o$, and flexural, $A_o$) in order to classify AE signals and is thus referred to as a modal analysis technique. Since it makes use of the Lamb wave modes, MAR is only applicable to structures that can support Lamb waves. Many aircraft are comprised, to a large degree, of plate-like structures which are capable of supporting Lamb waves, and thus MAR could prove to be a useful tool for monitoring damage occurring in aircraft.

An MAR analysis works on the basis that damage which causes an out-of-plane movement of the structure, for instance delamination, excites more energy in the flexural, $A_o$ mode and, conversely, damage producing an in-plane movement of the structure, such as matrix cracking, excites more energy in the extensional, $S_o$ mode (Gorman & Ziola 1991; Dzenis & Qian 2001; Zohari et al. 2013). Thus, calculating the amplitude ratio between the $S_o$ and $A_o$ modes using Equation 6-1 will reveal whether the signals are $S_o$ mode dominant (MAR>1) or $A_o$ mode dominant (MAR<1) and hence suggests the nature of the damage present, i.e. in-plane or out-of-plane respectively.

$$MAR = \frac{S_o\ Amplitude}{A_o\ Amplitude}$$

*Equation 6-1*

Using this approach previous studies have used the MAR to successfully classify signals by the orientation of their source mechanism in small composite specimens (Eaton et al. 2011; Eaton 2007; Gallego et al. 2014). However, it is understood that the attenuation of the $S_o$ and $A_o$ wave modes are dissimilar in carbon fibre composite (Sause et al. 2012; Eaton 2007) which is detrimental to the classification of damage using MAR on large-scale structures since the MAR of a single event will vary depending on the source to sensor propagation path. Furthermore, in the past, researchers characterising AE events using a modal analysis techniques such as MAR have had to manually determine the $S_o$ and $A_o$ mode amplitudes by inspecting the recorded waveforms (Gorman & Prosser

1991; Gorman & Ziola 1991; Prosser 1996; Surgeon & Wevers 1999; Pullin et al. 2005; Eaton 2007; Jong 2006). This is a time consuming process, even for short duration tests on small scale laboratory specimens, and so would be very impractical for an SHM system which is continuously monitoring large scale structures. Not to mention that the ideal SHM system would be autonomous, requiring minimal human input.

In this chapter a novel form of MAR analysis is proposed which not only corrects for the attenuation of both wave modes before making the MAR calculation, but also does so in an automated process.

## 6.1 Automated Corrected MAR

To overcome the issues that arise due to signal attenuation when attempting to characterise damage using MAR, Eaton (2007) developed a correction process which used the recorded amplitudes of each of the Lamb wave modes, and information about the propagation behaviour of AE in the specimen under question to estimate the amplitudes of the Lamb wave modes at their predicted point of origin. However, the approach required manual inspection of the waveforms collected to identify the amplitude of each Lamb wave mode and subsequently manual correction of those amplitudes. Furthermore, the correction process itself was performed in a manner which involved converting the units of amplitude from volts to decibels in order to perform the correction and then making the conversion back to volts to perform the MAR calculation. The *Automated Corrected MAR* technique presented in this chapter differs from the approach taken by Eaton (2007) in both the fact that it is automated, and also in the manner in which the correction process is performed.

### 6.1.1 Automated calculation of $S_o$ and $A_o$ mode amplitude

The amplitude calculation process of the *Automated Corrected MAR* technique requires the velocities and frequencies of each of the wave modes, within the material under inspection, to be known; thus, it is necessary to complete a propagation study if this information is not already known for the specimen under consideration. Assuming that

the propagation data is known, the automated calculation of the $S_o$ and $A_o$ mode amplitudes is carried out as followed;

1. The propagation path is calculated; or more specifically, the distance and angle that a recorded signal is predicted to have travelled before reaching the recording sensor is calculated. This is done by considering the problem in two dimensions and comparing the known location of the recording sensor with the calculated location of the AE and then using trigonometry, Equation 6-2 and Equation 6-3, to determine the distance and angle, Figure 6.1.

.

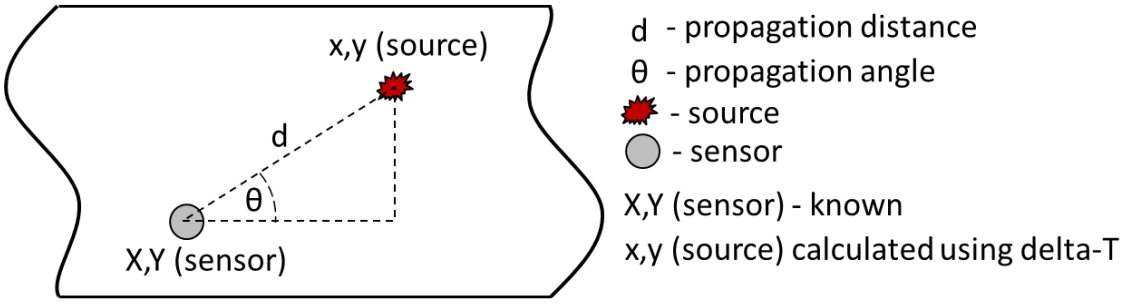


*Figure 6.1: Schematic showing the calculation of the propagation path*

$$d = \sqrt{(X-x)^2 + (Y-y)^2}$$

*Equation 6-2*

$$\theta = \tan^{-1}\left(\frac{(Y-y)}{(X-x)}\right)$$

*Equation 6-3*

2. The recorded waveform is then windowed to produce two wave segments, with each segment isolating either the $S_o$ or $A_o$ mode; an example of the windowing process is shown in
3. Figure 6.2 (b) and (d). The windowing process assumes that the threshold crossing method used by the AE acquisition set up is able to accurately identify the first arrival of the signal, and thus the $S_o$ mode is assumed to arrive at t=0 s. In order to account for triggering errors, and ensure that the entirety of the $S_o$

wave mode is isolated in the windowed segment, the $S_o$ mode window is set to begin 100μs before t=0 s. Using the known velocities of the two wave modes for the calculated propagation angle and distance, the difference in time of arrival between the $S_o$ and $A_o$ modes is calculated using Equation 6-4.

$$Difference\ in\ arrival\ time\ between\ S_o\ and\ A_o = \left(\left(\frac{d}{A_o velocity}\right) - \left(\frac{d}{S_o velocity}\right)\right)$$

*Equation 6-4*

The windowed segment that is to contain the $S_o$ mode is set to end at the time of the $A_o$ arrival (plus a number of sample points equal to the filter order since these will be lost during the filtering process). The windowed segment that is to contain the $A_o$ mode starts at the time calculated by Equation 6-4 and finishes 100μs later (plus the number of sample points that will be lost during the subsequent filtering process). The $A_o$ mode window is just 100μs long so that the effect of reflections is reduced.

4. The two windowed wave segments are then filtered using appropriate bandpass filters, to further isolate the $S_o$ and $A_o$ modes, as shown in
5. Figure 6.2 (c) and (e). The filters used to isolate each wave mode will be unique for each test specimen; wavelet transforms of the AE recorded during the propagation study can be used to determine the dominant frequencies over which each of the wave modes travel, and thus appropriate bandpass filters can be designed.
6. Once each of the wave modes has been isolated via filtering, the maximum amplitude of each is determined,
7. Figure 6.2 (c) and (e).

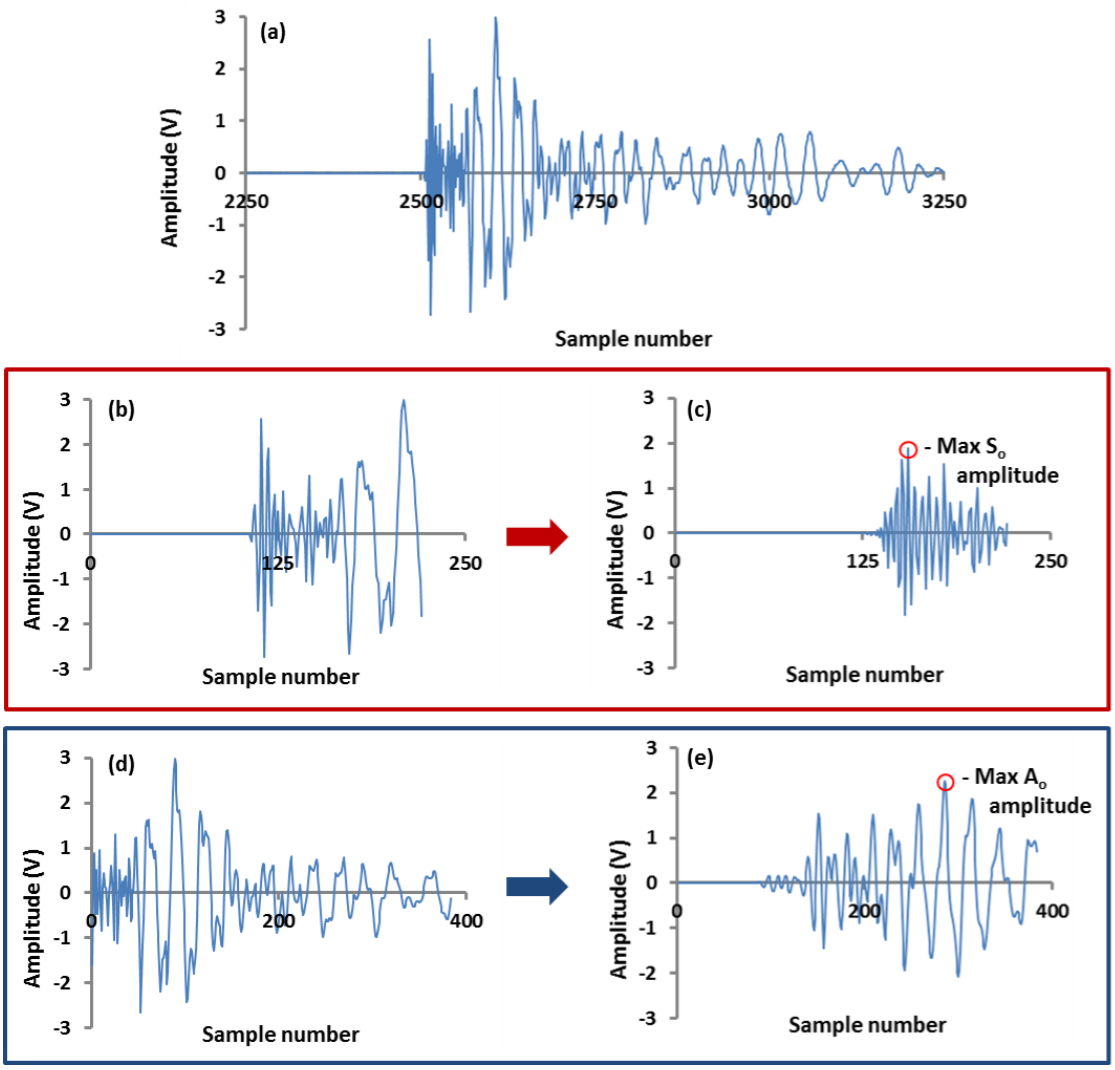


*Figure 6.2: (a) Original signal (b) $S_o$ mode windowed segment, extracted from original signal using time of flight information (c) $S_o$ mode obtained from windowed segment using filter (d) $A_o$ mode windowed segment, extracted from original signal using time of flight (e) $A_o$ mode calculated from windowed segment using filter*

### 6.1.2 Correction of $S_o$ and $A_o$ mode amplitudes and calculation of MAR

Once the amplitudes of each of the wave modes have been determined, they can be corrected for their attenuation over the propagation distance. The correction process requires knowledge of the attenuation behaviour of the wave modes and so this must also be calculated using an attenuation study if it is not already known.

The amplitude correction process comprises of comparing the maximum amplitude of a particular wave mode to the amplitude of that mode's attenuation curve for the same

propagation distance. The ratio of the two values is used to modify the equation for the attenuation curve for that wave mode. The modified equation for the attenuation curve is then assumed to be able to predict the amplitude of that wave mode at any propagation distance, for the particular event which caused the recorded AE, and thus the amplitude of that wave mode at the source can be calculated from the modified equation.

Figure 6.3 gives a pictorial example of this process for the correction of the $S_o$ wave mode. Figure 6.3 (a) shows the attenuation curve for the $S_o$ wave mode for a propagation angle of 10 degrees; Figure 6.3 (b) shows the amplitude of the $S_o$ wave mode of a single recorded AE hit, plotted alongside the original attenuation curve (the distance of the source to the sensor was calculated in Equation 6-2), and highlights the amplitude of the original attenuation curve at the same distance. The ratio of these two amplitude values can be used as a coefficient to modify the original attenuation curve and obtain a modified attenuation curve which is specific to the AE hit under investigation; this is shown as the red line in Figure 6.3 (c). The modified attenuation curve can then be used to calculate the amplitude of the $S_o$ mode at any propagation distance, i.e. the amplitude of the $S_o$ mode at the source can be calculated. This process can be carried out for both the $S_o$ and $A_o$ wave modes, in order to calculate the amplitude of each mode at the source of the AE event, and subsequently, these values can be used to calculate the MAR of that AE event using Equation 6-1.

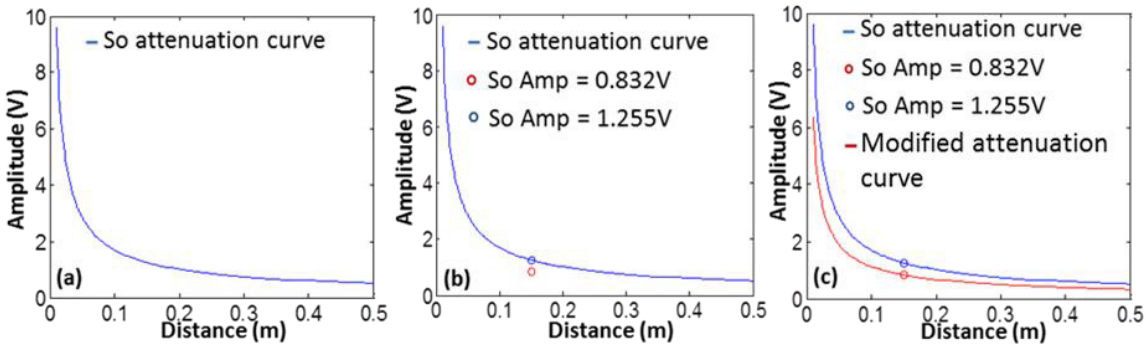


*Figure 6.3: (a) Attenuation curve of $S_o$ mode along $0^o$ (b) Amplitude of signal and attenuation curve, at the same distance, are compared (c) Corrected attenuation curve for this signal calculated*

## 6.2 Carbon Fibre Composite Buckling Test

In order to verify the effectiveness of this newly proposed *Automated Corrected MAR* technique in practice, it was applied to the results obtained from a buckling test conducted on a carbon fibre composite panel. The details of that experiment are provided in the following section.

The composite panel used for this investigation was an eight ply layup of Umeco MTM®44- 1 unidirectional carbon fibre composite with the configuration (0,90)4s. The panel's dimensions were 403x376mm with a thickness of 3.3mm. The panel was ultrasonically C-scanned in order to assess the manufacturing quality prior to testing; no signs of damage were observed.

### 6.2.1 Propagation study

As mentioned previously, the *Automated Corrected MAR* technique requires knowledge of the propagation behaviour of both Lamb wave modes prior to conducting the experiment and thus a propagation study was carried out on the carbon fibre composite panel. To evaluate the attenuation behaviour of the $S_0$ and $A_0$ propagation modes four wideband, MISTRAS Group Limited (MGL) WD sensors (100-1000kHz) were placed 70mm apart, in a line along the 0° material direction. They were held in place between magnets positioned on both surfaces of the panel and multipurpose, brown grease was used as the acoustic couplant. The sensors were connected to MGL pre-amplifiers, set to a gain of 40dB and with a frequency range of 20-1200kHz, and AE data was recorded using a MGL PCI2 acquisition system. Ten Hsu-Nielsen (H-N) sources were generated at a distance of 10mm behind the first sensor and the resultant signals were recorded for all four sensors. This process was repeated at 10° intervals up to 90 degrees, Figure 6.4.

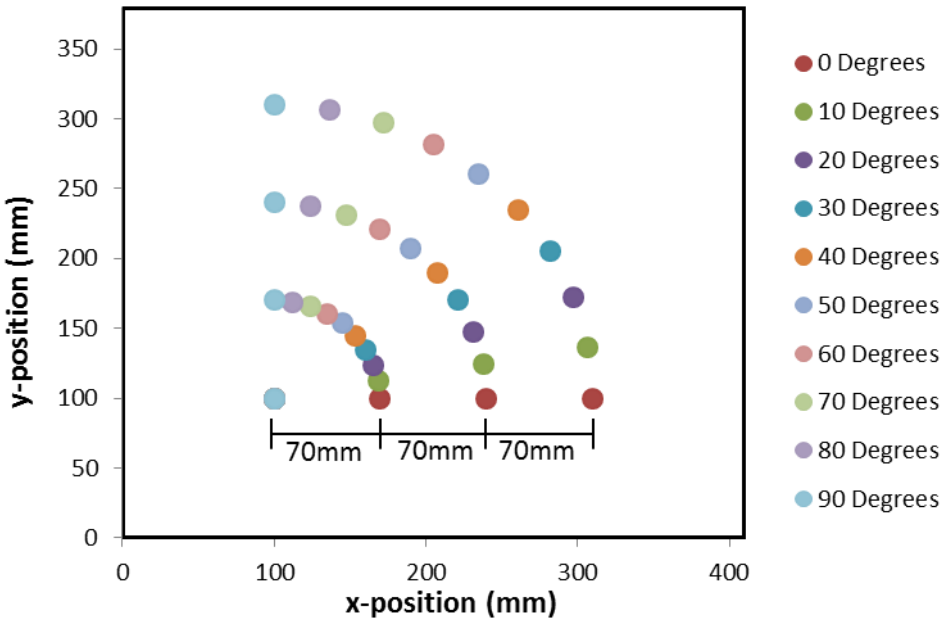


*Figure 6.4: Sensor positioning during propagation study*

Once this AE data was recorded it was manually inspected in order to calculate the velocity and attenuation of each mode with respect to angle. Figure 6.5 shows the results of the velocity study for all propagation angles and an example of the results of the attenuation study for one propagation angle.

As recommended by Vallen Systeme GmbH (2012), the dominant frequencies of $S_o$ and $A_o$ wave modes in the specimen were determined by examining the frequency content of AE data collected from the pencil lead breaks. As demonstrated by Hamstad et al (2002), this was done via the use of wavelet transforms, created using *AGU-Vallen Wavelet*. Figure 6.6 shows an example of one such wavelet transform, and how the frequencies of both Lamb wave modes were determined. Wavelet transforms were calculated for several waves, recorded at different distances and angles, until the range of dominant frequencies of each mode was determined. It was found that the dominant frequencies of the $S_o$ mode were between 150 and 500 kHz, and the dominant frequencies of the $A_o$ mode were between 10 and 150 kH,z which is in good agreement with other researchers in the field (Martínez-Jequier et al. 2015; Surgeon & Wevers 1999).

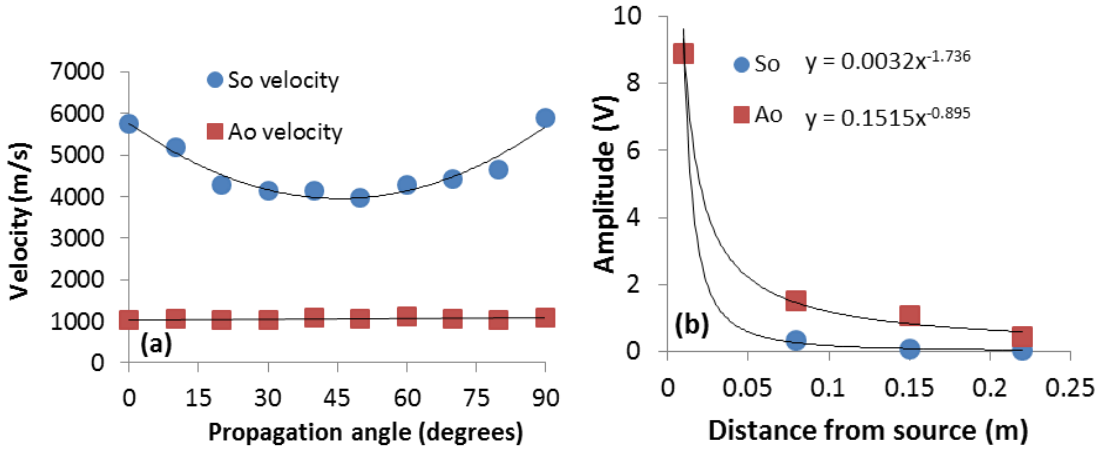


*Figure 6.5: (a) Velocity of both wave modes for each propagation angle tested (b) attenuation behaviour of both modes for 50$^o$ angle of propagation*

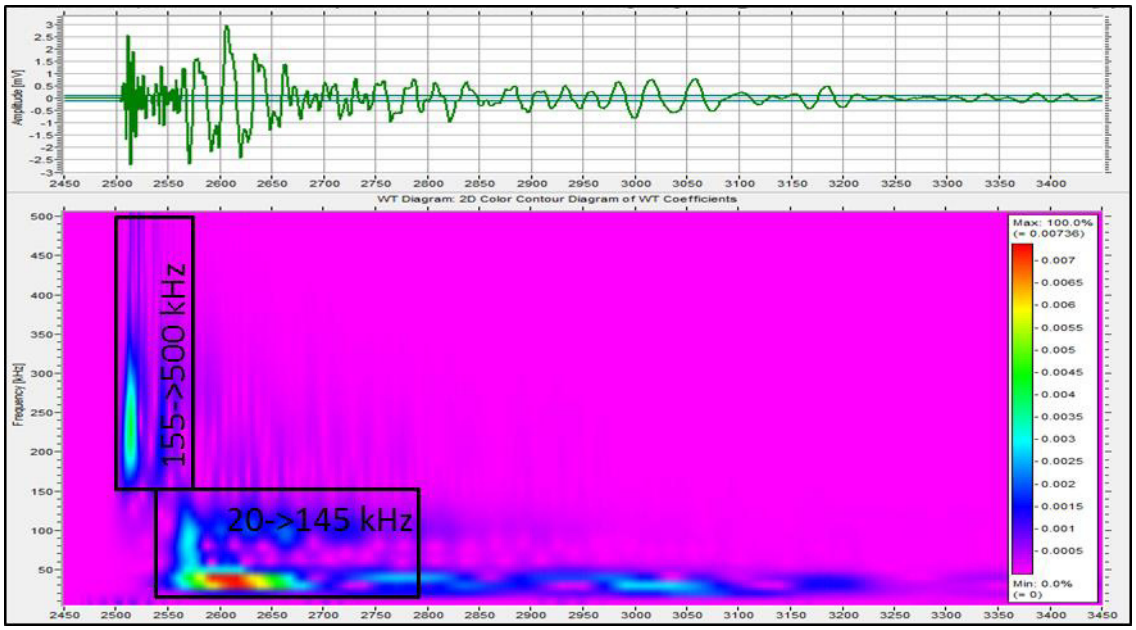


*Figure 6.6*: Wavelet transform of wave recorded at 8cm distance from the source along 0$^o$ angle

### 6.2.2 Buckling test procedure

The buckling test rig used for this experiment can be seen in Figure 6.7. The base and the left and right edges are prevented from moving in-plane whereas the top edge is free to move vertically downwards, thus allowing the plate to be compressed by applying a force to the top edge. Roller supports along the horizontal edges and sprung knife edges along the vertical sides provide simply supported boundary conditions on all four edges.

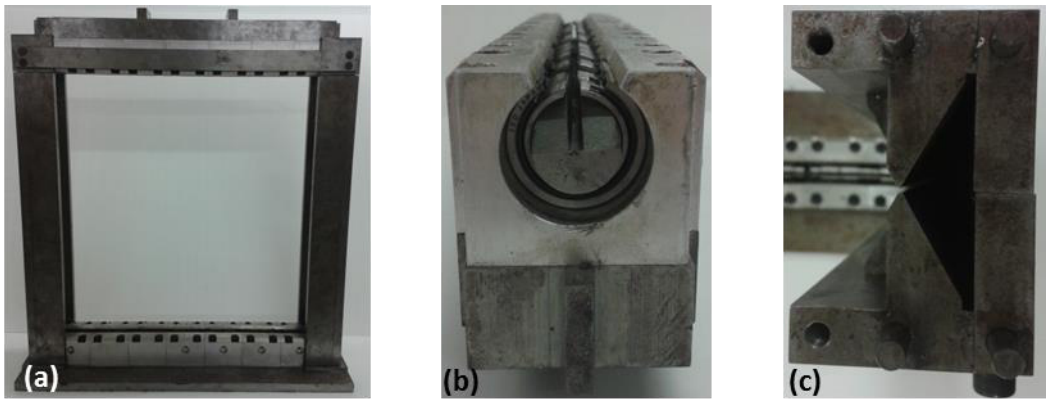


*Figure 6.7: (a) Buckling test rig (b) Horizontal roller supports (c) Vertical knife edge supports*

A speckle pattern was applied to one side of the specimen, using spray paint, to allow digital imaging correlation (DIC) monitoring to be implemented, Figure 6.8 (a). Three MGL WD sensors (100-1000kHz) and five MGL Nano-30 sensors (125-750kHz) were chosen to be used in the experiment; the wideband WDs were intended to extract information about the characteristics of the waveforms for the characterisation process, though due to their limited availability it was necessary to also use five Nano-30's to provide more time of arrival information and increase the accuracy of the location calculation. The eight sensors were adhered to the surface in the positions shown in Figure 6.8 (b) using Loctite® 595, a multi-purpose clear silicone sealer, which also acted as the acoustic couplant between the panel and the sensors. The same acquisition setup as that was used in the propagation study was adopted.

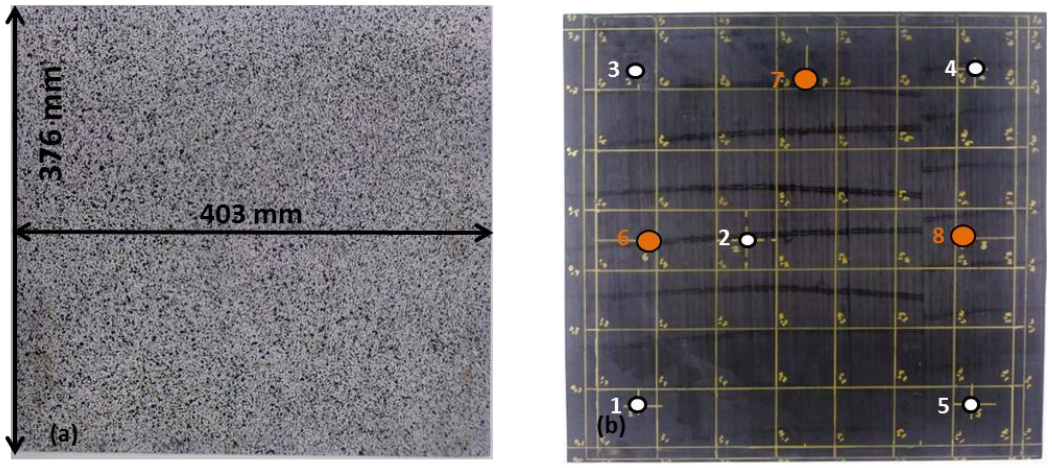


*Figure 6.8: Carbon fibre composite panel used for study (a) DIC prepared, speckled surface (b) delta-T mapping training grid and location of sensors*

The specimen was mounted into the rig and loaded in compression at a constant rate of 0.24 mm/min until failure occurred. AE data was recorded during this time and DIC images were captured manually approximately once every 1kN of increased loading.

### 6.2.3 Buckling test results

After failure, the specimen was removed from the test rig and inspected for damage; delamination was visible by eye in the upper left corner of the panel. The test specimen was C-scanned, using a 5MHz ultrasonic probe, to further assess the induced damage, as shown in Figure 6.9. A large area of high attenuation was observed in the top left corner; the four additional spots of high attenuation observed near the panel centre are caused by the panel's supports in the C-scan tank and so can be ignored.

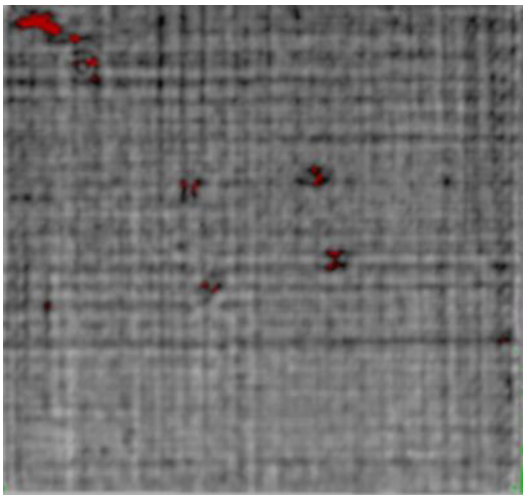

*Figure 6.9: C-scanned image after buckling*

The results of the DIC analysis revealed that the onset of buckling occurred at approximately 5kN. During post-buckling, the panel deformed with a constant stiffness until approximately 26kN at which point the structure's behaviour changed and the stiffness dropped, likely due to the onset of damage within the panel, Figure 6.10. Final material failure occurred at 44.61kN.

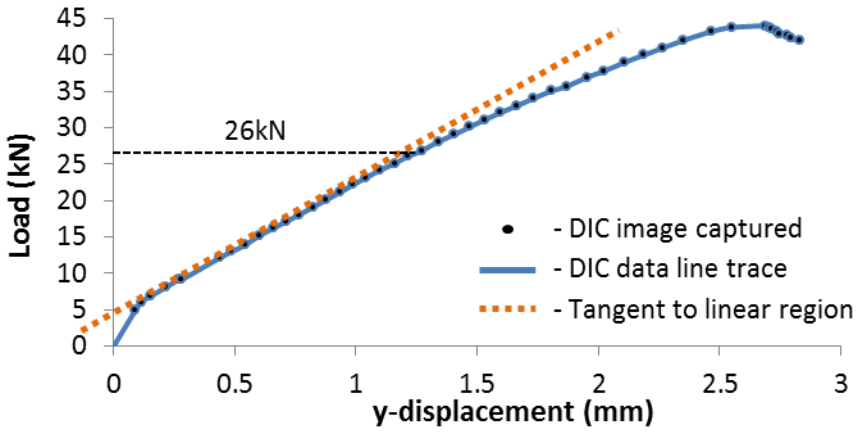


*Figure 6.10: DIC results showing stiffness change at approximately 26kN*

### 6.2.4 Characterisation of AE signals

To assist the characterisation process, only located signals were analysed. Signals were located using *delta-T mapping* since, as discovered in Chapter 4 and other studies (Eaton et al. 2012; Baxter et al. 2007), it provides increased accuracy over the conventional time-of-arrival (TOA) technique. For ease of interpretation, the *Automated Corrected MAR* analysis was conducted using only the data recorded by the WD sensor in position 6, Figure 6.8, because it was a wideband sensor equidistant from the two corners where the majority of the AE data was recorded.

The MAR values calculated for the recorded waves were analysed in terms of two groups, MAR>1 and MAR<1, to distinguish between in-plane and out-of-plane sources respectively. Once the data was categorised in this way the cumulative energy of each group was plotted, to show the evolution of their activity over the course of the test, alongside the load trace, Figure 6.11 . To demonstrate their relative levels of activity further, the cumulative number of events of each group was also plotted against time, alongside the load trace, Figure 6.12.

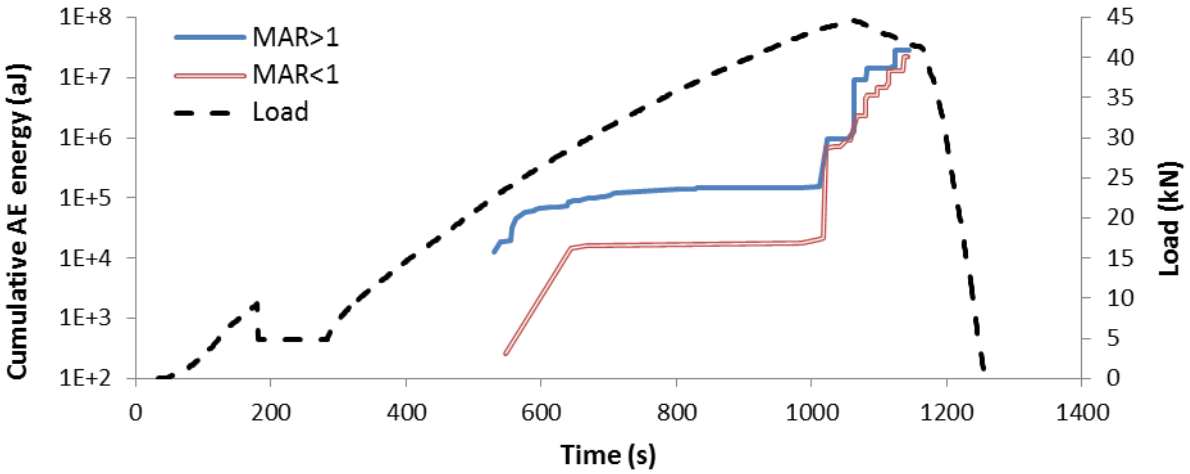


*Figure 6.11: Cumulate AE energy with load for both MAR classes*

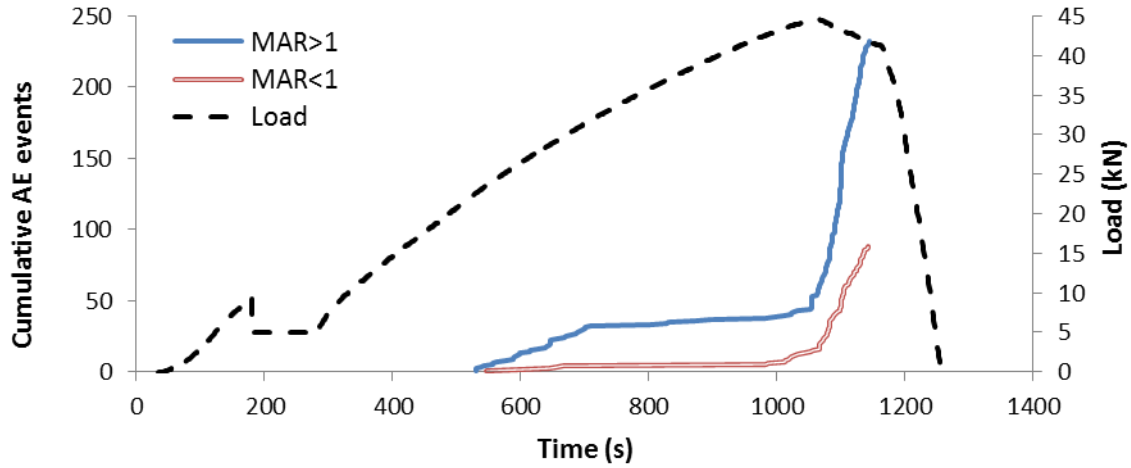


*Figure 6.12: Cumulate AE events with load for both MAR classes*

The drop in the load near the beginning of the test is due to the specimen settling into the test rig supports. MAR>1 signals have an earlier onset and higher overall level of activity compared with MAR<1 signals. There are two main periods during which MAR>1 signals are most active; firstly at approximately 580s, corresponding to the point at which the DIC analysis identified the panel's stiffness to change, at 26 kN, and secondly in the period shortly before and during final failure. MAR<1 signals only begin to appear to a significant degree in the later stages of loading, shortly before and during the final failure of the material. Although there is a very small number of MAR<1 signals before this the vast majority of MAR<1 signals occur in the later stages of loading. Despite the total number of MAR<1 signals being less than half the total number of MAR>1 signals, the

total energy of each class is comparable, thus the average energy of MAR<1 signals is higher than that of MAR>1 signals.

Based on the data from these plots, the test was divided into 4 time segments as follows:

- Segment 1 from 0s to 590s (from the beginning, to the appearance of the first located events);
- Segment 2 from 580 s to 700 s (up to the end of the first high-activity phase);
- Segment 3 from 1000 s to 1070 s (the onset of the second high activity phase and peak load);
- Segment 4 from 1060 s to the end of the test and final material failure;

Combining the classification of signals with the *delta-T mapping* location results allows the hits belonging to each class to be plotted spatially; this was done for each time segment in order to show the evolution of classified signals spatially over time, Figure 6.13. It can be seen that the first located signals originated from the bottom-left corner of the panel and have MAR>1. As the test progresses the number of MAR>1 signals remains very low and more MAR>1 signals arise in the bottom-left corner. At the onset of the second high activity phase the level of activity of both groups increases and MAR<1 signals begin to appear in larger quantities all along the left-hand-side of the panel; MAR>1 signals begin to originate from the top-left corner or the panel. After 1070 s most of the activity is observed in the top-left corner with both MAR>1 and MAR<1 signals occurring in large quantities until final failure. By the end of the test, large clusters of MAR>1 signals can be seen to have originated from the bottom-left, centre and top-left of the panel whereas the majority of MAR<1 signals originate from the top-left corner of the panel though a significant number can also be seen to originate from the centre.

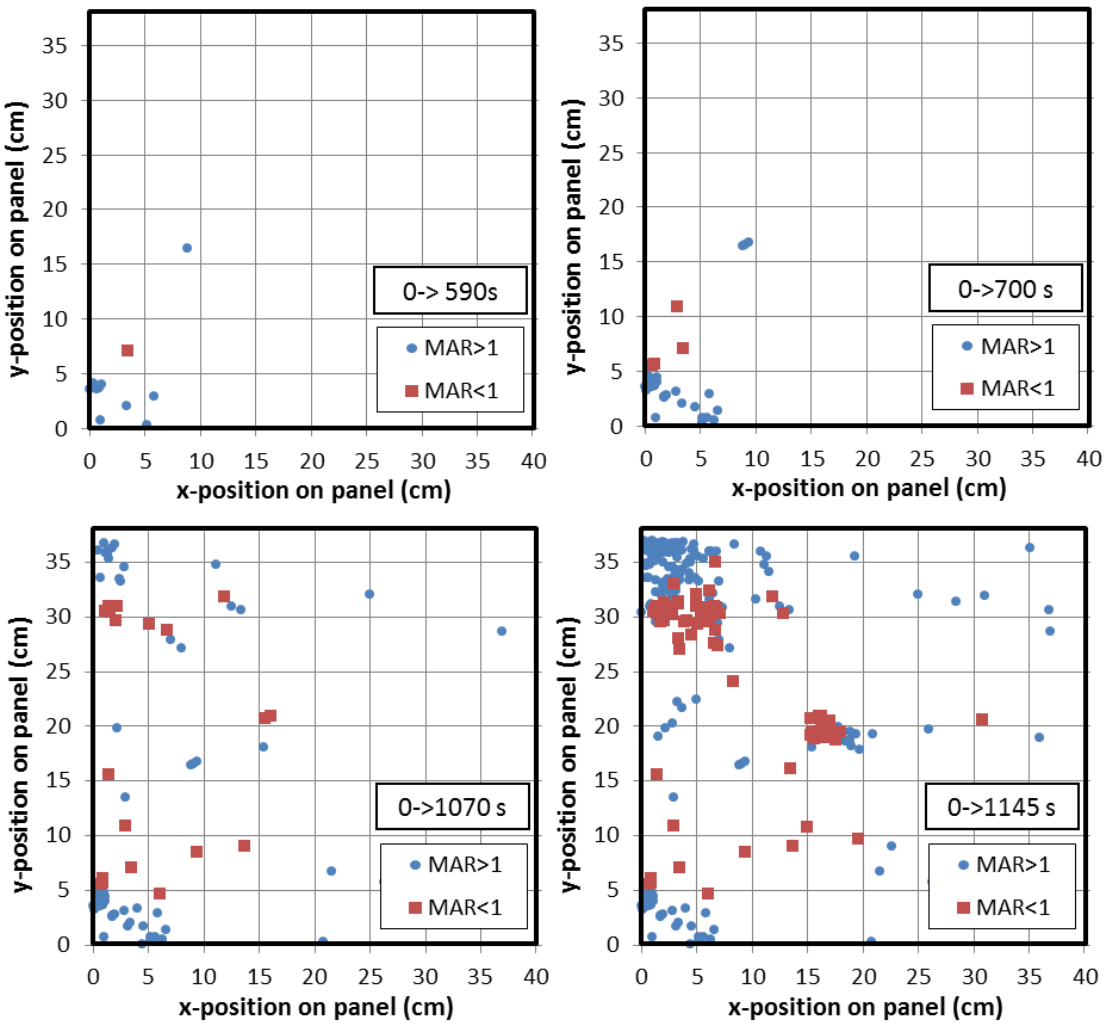


*Figure 6.13: Historical distribution of MAR>1 AND MAR<1 signals during test*

Unfortunately the *delta-T mapping* location method is not without fault and it is believed that a number of signals originating from the corners were mis-located as originating from the centre of the panel. This is believed to be the case since the highest curvature in the panel is observed in the corners, where it is restrained, and so the centre of the panel, which is the least strained region, is least likely to be damaged. This mis-location effect was also witnessed on a similar, previous study (Eaton 2007) and so signals located as originating from the centre of the panel will no longer be discussed.

### 6.2.5 Discussion

The existence of significant numbers of both MAR>1 and MAR<1 signals suggests that there are at least two different damage mechanisms occurring in the panel during the

experiment. MAR>1 signals are active from approximately 530s onwards and originate from both the top-left and bottom-left corners of the panel whereas MAR<1 signals are active from approximately 970s and originate predominantly from the top-left corner of the panel. MAR<1 signals are also more energetic than MAR>1 signals.

The C-scan inspection revealed an area of delamination at the top left corner of the panel, a common failure mode for CFRP subject to bending loads. This agrees with the result of the *Automated Corrected MAR* analysis since MAR<1 signals, indicative of delamination (Gorman & Ziola 1991; Dzenis & Qian 2001; Eaton 2007; Eaton et al. 2011), are predominantly located at the top-left corner of the panel. Delamination is often dominant in the final failure of composite materials and hence is only likely to be present in the final stages of testing, which also corresponds to the activity of MAR<1 signals observed. Thus it is believed that the *Automated Corrected MAR* analysis is successfully identifying delamination damage.

Given the allocation of MAR<1 signals to delamination it is likely that MAR>1 signals are originating from in-plane matrix damage. Matrix cracking is commonly the first damage mechanisms to occur in CFRPs under quasistatic loading conditions (M G R Sause et al. 2012; de Oliveira & Marques 2008; Dzenis & Qian 2001) and the MAR>1 signals are the first to appear in this test. They have a large amount of activity around 600s (26kN) where the stiffness of the specimen was observed to change. This reduction in stiffness could be attributed to the onset of matrix damage in the material, because the matrix stiffness has a large bearing on the compressive strength of composite materials (Soutis 1995; Fleck 1997). The second large jump in activity of MAR>1 signals is around 1060s, shortly before and during final material failure and during the onset of MAR<1 signals. In this instance it is likely that the curvature of the top-left of the panel, as a result of buckling and the specific restraints of the test rig, caused large enough strains for matrix cracking to take place. The build-up of this damage reduced the structural integrity of the corner until delamination occurred. This in turn caused the matrix structure to bear more of the load and crack further leading to more delamination; hence the large increase in activity

of both classes of signal during final material failure. The MAR>1 signals detected during final failure could also be connected to fibre failure as this typically occurs closer to the final failure of the composite, as the fibres begin to exceed their ultimate strain. However it is believed that fibre failure did not occur in this test to any distinguishable degree and that instead the large bending in the corners caused a tearing motion leading delamination to occur before the fibres could fail.

## 6.3 Conclusions

*Automated Corrected MAR* is a novel AE analysis technique which uses a combination of windowing and frequency filtering to isolate the $S_o$ and $A_o$ wave modes of collected AE waveforms before using the relative locations of the recording sensor and AE source, and an understanding of the propagation behaviour of each mode, to automatically predict their amplitudes at the source location. Due to the nature of Lamb waves which propagate in flat, plate like structures, a comparison of the $S_o$ and $A_o$ mode amplitudes is then used to give an indication as to the orientation of the source relative to the recording sensor and hence, and indication as to the type of damage present.

This chapter describes a buckling test which was carried out on a carbon fibre composite panel in order to investigate the ability of *Automated Corrected MAR* to characterise signals arising in the specimen. Under the applied loading the carbon fibre composite panel experienced a buckling failure, causing delamination to occur in the top-left corner of the specimen and matrix cracking to occur in both the top-left and bottom-left corners of the specimen. The presence of delamination was verified via the use of an ultrasonic C-scanner and the presence of matrix cracking was inferred from analysis of the relevant literature. The AE data collected was processed using *delta-T mapping* to obtain accurate locations for events occurring during the test. The waveforms collected were subsequently processed using the novel *Automated Corrected MAR* technique which identified a portion of the signals originating from the top-left corner of the specimen as having a low MAR, i.e. below one, with all other signals having a larger MAR. Due to the test set up, this result suggested that a number of the signals coming from the top-left

hand corner of the specimen, the corner which experienced delamination, were due to AE sources with energy in a predominantly out-of-plane direction, such as delamination. Thus the *Automated Corrected MAR* technique can be said to have been able to successful in distinguishing between in and out-of-plane signals arising in the experiment.

The work from this chapter has formed the basis of the following journal and conference publications;

J. McCrory, S. Kh. Al-Jumaili, D. Crivelli, M. R. Pearson, M. J. Eaton, C. A. Featherston, M. Guagliano, K. M. Holford and R Pullin. (2015) 'Damage classification in carbon fibre composites using acoustic emission: A comparison of three techniques'. Journal of Composites: Part B. Vol 68, pp 424–430.

S. Kh. Al-Jumaili, K. M. Holford, M. J. Eaton, J. McCrory, M. R. Pearson and R Pullin. (2014) 'Classification of acoustic emission data from buckling test of carbon fibre panel using unsupervised clustering techniques'. Structural Health Monitoring Vol 14 (3), pp. 241-251.

J. McCrory, S. Kh. Al-Jumaili, M. R. Pearson, M. J. Eaton, K. M. Holford and R Pullin. (2014) 'Automated Corrected MAR Calculation for Characterisation of AE Signals'. 31st European Conference on Acoustic Emission Testing, Dresden, Germany, 09/2014.

S. Kh. Al-Jumaili, M. J. Eaton, K. M. Holford, J. McCrory and R Pullin. (2014) 'Damage characterisation in composite materials under buckling test using acoustic emission waveform clustering technique', 53rd Annual Conference of The British Institute of Non-Destructive Testing, Manchester, UK; 09/2014.

D. Crivelli, M Guagliano, J. McCrory, S. Kh. Al-Jumaili, M. J. Eaton, M. R. Pearson, K. M. Holford and R Pullin. (2013) 'Classification of Acoustic Emission Data from Buckling Test of Carbon Fiber Panel using Neural Networks', 3rd European Aeronautics Science Network Workshop on Aerostructures, Politechnico di Milano; 10/2013.

# 7 Conclusions and Recommended Future Work

## 7.1 Conclusions

This thesis has explored the use of a number newly developed, advanced AE techniques for aerospace structures, with the intention of determining their applicability for use in an SHM system. The work has consisted of three main experimental studies which, between them, have demonstrated AE's ability to detect, locate and characterise signals occurring in the tested specimens. Each of the experimental studies was conducted on a different aerospace material and so the use of AE has been tested across a range of mediums.

The influence of the training grid's spatial resolution on the accuracy of the *delta-T mapping* technique was investigated. This was carried out by generating artificial, H-N sources on the surface of a large GLARE panel with complex geometric features, and locating these signals using both the TOA and *delta-T mapping* techniques. The key findings were:-

- *Delta-T mapping* was found to produce more accurate location results than the TOA technique across all of the training grid resolutions tested.
- TOA calculated the artificial signals to within 0.603cm of their true positions.
- Using training grids with resolutions of 1x1, 2x2, 3x3, 4x4, 5x5 and 7x7cm, *delta-T mapping* was capable of calculating the location of the artificial sources to within 0.331, 0.441, 0.421, 0.430, 0.489 and 0.430cm of their true positions respectively.
- The training grid with the finest spatial resolutions, 1x1cm, was found to produce the most accurate locations.
- There was a noticeable decrease in accuracy between the *delta-T mapping* results obtained using the 1x1cm and 2x2cm resolution training grids however there was very little difference between the accuracy of the *delta-T mapping* results obtained using the 2x2, 3x3, 4x4, 5x5 and 7x7cm resolution training grids.

- A velocity study was also carried out on the GLARE panel specimen which revealed that the $S_o$ Lamb wave mode velocity varied very little with propagation direction, and had an average velocity of 4836 m/s.

A novel form of data acquisition and analysis called an *Additive Hits Analysis* (AHA) was developed. The AHA was tested alongside conventional AE wavestreaming for comparison using the data collected from an aerospace grade 300M steel beam which was cyclically loaded until it failed under fatigue. The specimen was also monitored for crack growth using DIC. It was concluded that:-

- Each of the analysis techniques used; DIC, conventional AE feature analysis, *Additive Hits Analysis* and AE Wavestreaming, identified cracking to begin at 7,385, 7,412, 7,310 and 8,764 seconds respectively.
- By examining the frequency content of a number of high amplitude hits located with *delta-T mapping* as coming from the crack region, the 350kHz band was identified as being related to crack growth signals.
- Despite this, it was infeasible to track the progression of cracking by plotting the cumulative energy of the 350kHz frequency band with either AHA or conventional wavestreaming data due to the short duration of the 350kHz section of the signal being very small in duration compared with the rest of the signal.
- AHA and wavestreaming returned results which were consistent with one another, though the frequency spectra of the AHA data sets were less skewed by noise that those of the conventional wavestreaming data sets.
- On average the size of the AHA data sets was just 17.5% of the size of a conventional wavestream data set and thus AHA provided all the same data as conventional wavestreaming but at a fraction of the file size and with less ambiguity in the frequency spectra.
- DIC was found to be a useful tool for validating the AE testing.

A novel form of characterisation technique called *Automated Corrected MAR* was developed. Its effectiveness was examined using the results obtained from a compression test on a carbon fibre composite panel, which was also monitored using DIC during the test.

- Under the applied loading, the carbon fibre composite panel experience buckling failure and developed a sizable delamination in one of the corners.
- Ultrasonic C-scanning and DIC were found to be useful tools for validation of AE.
- A propagation study on the carbon fibre composite specimen revealed the $S_o$ Lamb wave mode velocity to have strong directional dependency, ranging from 5892 to 3965 m/s, and the $A_o$ Lamb wave mode to have a relatively consistent velocity in all directions, with an average of 1061 m/s.
- The attenuation behaviour of each Lamb wave mode was found to follow a power law approximation, with the $S_o$ mode attenuating faster that the $A_o$ mode.
- The travelling frequencies of the $S_o$ and $A_o$ Lamb wave modes were found to be 150->500 kHz and 20->150 kHz respectively.
- *Automated Corrected MAR* was able to successfully distinguish between in and out-of-plane signals

## 7.2 Recommendations for Future Work

This thesis has explored several advanced AE techniques and there is scope for additional work to improve and develop each of them further.

*Delta-T mapping* has proved its usefulness time and again throughout the studies contained in this thesis, however it is time consuming and laborious to implement in practice, especially on large scale specimens or structures. For it to be considered as a serious option outside small scale research environments, optimisation of the method in which the training grid data is collected should be considered. This might be achievable by reducing the number of grid points necessary and implementing a more versatile

interpolation calculation, or by utilising the AE sensors themselves to pulse and receive in order to gather the data.

The *Additive Hits Analysis* and *Automated Corrected MAR* techniques developed in this thesis would benefit from being implemented in real-time rather than being post-processed. This would be possible using software such as Vallen Group's *AEVisual*.

*Automated Corrected MAR* performed well in determining whether a signal originated from an in or out-of-plane source, however it is currently unable to distinguish between two difference source mechanisms which are both in or out-of-plane, such as matrix cracking and fibre fracture which are both considered to be in-plane sources. However, if the *Automated Corrected MAR* technique was expanded to simultaneously investigate other features of the AE wave, in a combined modal-feature based technique, then there is potential for it to have this capacity also. Furthermore, the automated windowing process was implemented in a sub optimum manner. If the code was developed to incorporate an AIC picker then a more accurate start point of the transient AE wave could be found.

Feature correction, such as the amplitude correction process incorporated in the *Automated Corrected MAR* technique, is likely going to form the cornerstone of AE characterisation techniques in the future. The vast majority of characterisation studies performed to date have been conducted on small scale laboratory specimens and many of the techniques would face difficulties in obtaining consistent characterisation of source mechanisms in large scale specimens, due to signal attenuation and propagation effects. Correcting AE features to account for propagation paths, attenuation and geometric effects is going to be a large area of research in the future and could be tackled in a number of ways, including computational modelling, collecting data using manually generated artificial sources or by collecting data via pulsing and receiving with AE sensors. The data collected could then be used to perform feature correction and feed into the AE characterisation process.

Looking further afield, many more tests should be conducted to compare AE with conventional NDT techniques so that more confidence in AE can be instilled in the wider engineering community. Eventually AE should be given the opportunity to operate in preliminary trials on working aircraft to gather real field data and determine its effectiveness.

# 8 References


Aboulafia, R., 2015. *World Military and Civil Aircraft Briefing*, Teal Group Corporation.

AeroStrategy, 2007. *Winds of change*, Available at: http://www.fac.org.uk/wp-content/uploads/2013/01/AeroStrategy_Civil-Aerospace-Commentary_March_2007.pdf.

AirBus, 2015. Eco-Efficiency. *AirBus A350 XWB Website*. Available at: http://www.a350xwb.com/eco-efficiency [Accessed July 2, 2015].

Airbus, 2015. Taking the Lead: the A350 XWB. Available at: https://www.airbusgroup.com/dam/assets/airbusgroup/int/en/investor-relations/documents/2006/untitled/further_pre_a350_xwb_launch_2006.pdf [Accessed July 20, 2015].

Akaike, H., 1974. Markovian Representation of Stochastic Processess and its Application to the Analysis of Autoregressive Moving Average Processes. *Annals of the Institute of Statistical Mathematics*, 26(1), pp.pp. 363–387.

Alam, S.Y., Saliba, J. & Loukili, A., 2014. Fracture examination in concrete through combined digital image correlation and acoustic emission techniques. *Construction and Building Materials*, 69, pp.232–242. Available at: http://dx.doi.org/10.1016/j.conbuildmat.2014.07.044.

Arnau, A., 2004. *Piezoelectric Transducers and Applications*, New York: Springer.

ASTM, 1984. *A standard guide for determining the reproducibility of acoustic emission sensor response.*

ASTM, 1991. *E 1316 - Standard Terminology for Nondestructive Examinations.*

ASTM, 1998. *E 650 - Standard Guide for Mounting Piezoelectric Acoustic Emission Sensors.*

ASTM, 1982. *E610 - Standard Definition of Terms Relating to Acoustic Emission.*

ASTM, 1986. *Standard Method for Primary Calibration of Acoustic Emission Senseors.*

ASTM, 2011. *Standard Practice for Acoustic Emission Examination of Fibreglass Reinforced Plastic Resin (FRP) Tanks/vessels*.

ASTM, 2012a. *Standard Practice for Acoustic Emission Examination of Welded Steel Sphere Pressure Vessels Using Thermal Pressurization*.

ASTM, 2012b. *Standard Practice for Acoustic Emission Monitoring During Continuous Welding*, Available at: http://www.astm.org/Standards/E749.htm.

ASTM, 2012c. *Standard Practice for Acoustic Emission Monitoring During Resistance Spot-Welding*, Available at: http://www.astm.org/Standards/E751.htm.

AVIONERS, 2014. Airbus A350 XWB To Finish Last Phase of Certification. Available at: http://www.avioners.net/2014/07/airbus-a350-xwb-to-finish-last-phase-of-certification.html/ [Accessed May 14, 2015].

Baxter, M., 2007. *Damage Assessment by Acoustic Emission ( AE ) During Landing Gear Fatigue Testing*. Cardiff University.

Baxter, M.G. et al., 2007. Delta T source location for acoustic emission. *Mechanical Systems and Signal Processing*, 21(3), pp.1512–1520. Available at: http://www.sciencedirect.com/science/article/pii/S0888327006001178.

Bhaumik, S.K., Sujata, M. & Venkataswamy, M.A., 2008. Fatigue failure of aircraft components. *Engineering Failure Analysis*, 15(6), pp.675–694. Available at: http://www.sciencedirect.com/science/article/pii/S1350630707001409.

Bhavikatti, S., Bhat, M. & Murthy, C., 2011. Fatigue Crack Growth Monitoring in Ti-6Al-4V Alloy using Acoustic Emission Technique and Digital Image Correlation. *Journal of Non-Destructive Evaluation*, 9(4).

Boyne, W.J., Bilstein, R.E. & Crouch, T.D., 2015. History of flight. *Encyclopedia Britannica Online*. Available at: http://www.britannica.com/technology/history-of-flight.

British Standards Institution, 2010. *Non-destructive testing. Terminology. Terms used in ultrasonic testing*.

Brooks, P., 1967. The Development of Air transport. *Journal of Transport Economics and Polocy*, 1(2), pp.168–169.

Brownlee, K. et al., 2014. *Owens Corning Records, 1938-Present*, Available at: https://www.utoledo.edu/library/canaday/findingaids1/MSS-222.pdf.

Carbon Fiber Australia, 2014. Carbon fiber unidirectional tape. Available at: http://www.carbonfiber.com.au/prod71.htm [Accessed August 10, 2015].

Carmi, R. et al., 2015. Acoustic Emission and Digital Image Correlation as Complementary Techniques for Laboratory and Field Research. In *Advances in Acoustic Emission Technology*. p. pp 605–622.

Cha, K.K., 2013. *Composite Materials: Science and Engineering* Third., New York: Springer.

Chen, Z. et al., 2015. A method to transfer speckle patterns for digital image correlation. *Measurement Science and Technology*, 26(9). Available at: http://stacks.iop.org/0957-0233/26/i=9/a=095201?key=crossref.431b61ff458d2aa3e968e203f797c04b.

Cintrón, R. & Saouma, V., 2008. *Strain Measurements with the Digital Image Correlation System Vic-2D*. University of Colorado.

Composite Materials, 2015. GLARE Fiber Metal Laminates -Composite. Available at: http://www.compositematerialz.com/2015/06/glare-fiber-metal-laminates-composite.html [Accessed August 12, 2015].

Correlated Solutions, 2013. Principle of Digital Image Correlation. Available at: http://www.correlatedsolutions.com/digital-image-correlation/ [Accessed June 1, 2015].

Cranfield University Air Transport Department, 2010. *Fuel and air transport*,

Crivelli, D., Guagliano, M. & Monici, A., 2014. Development of an artificial neural network processing technique for the analysis of damage evolution in pultruded composites with acoustic emission. *Composites Part B: Engineering*, 56, pp.948–959. Available at: http://www.scopus.com/inward/record.url?eid=2-s2.0-84885336087&partnerID=40&md5=1d512bae44bac1117afd6a9a8bbc732e.

Dantec Dynamics, 2013. Q-400 DIC - Digital Image Correlation System - Measurement of Shape, Displacement and Strain. Available at: http://www.dantecdynamics.com/q-400-dic [Accessed June 1, 2015].

Davies, A.W. & Holford, K.M., 1997. Health Monitoring of Steel Bridges Using Acoustic Emission. In K. S. Virdi et al., eds. *Structural Assesment: the role of large and full-scale testing*. E & FN SPON, pp. 452–459.

Dzenis, Y.A. & Qian, J., 2001. Analysis of microdamage evolution histories in composites. *International Journal of Solids and Structures*, 38(10–13), pp.1831–1854. Available at: http://www.sciencedirect.com/science/article/pii/S0020768300001384.

Eaton, M., Pearson, M. and Lee W., 2015. Accurate Damage Location in Complex Composite Structures and Industrial Environments using Acoustic Emission. In *Journal of Physics: Conference Series*. Available at: http://stacks.iop.org/1742-6596/628/i=1/a=012105?key=crossref.378cd7746ac8aab843ced8f769fb4024.

Eaton, M., 2007. *Acoustic Emission (AE) Monitoring of Buckling and Failure in Carbon Fibre Composite Structures*. Cardiff University.

Eaton, M., May, M., Featherston, C., 2011. Characterisation of damage in composite structures using acoustic emission. *Journal of Physics: Conference Series*, 305(1). Available at: http://www.scopus.com/inward/record.url?eid=2-s2.0-80052068825&partnerID=40&md5=5c6511ad084849193ec7a987a2478684.

Eaton, M.J. Pearson, M., Bryne, C., Pricket, P., Pullin, R., Holford, K., 2014. Ensuring Drill Quality in Composite Materials Using. In *16th European Conference on Composite Materials*. pp. 22–26.

Eaton, M.J., Fetherston, C.A. & Holford, K., 2008. Imperfection sensitivity in plates - An assessment using DIC. In *11th International Congress and Exhibition on Experimental and Applied Mechanics*. Orlando, pp. pp. 943–948.

Eaton, M.J., Pullin, R. & Holford, K.M., 2012. Acoustic emission source location in composite materials using Delta T Mapping. *Composites Part A: Applied Science and Manufacturing*, 43(6), pp.856–863. Available at: http://www.scopus.com/inward/record.url?eid=2-s2.0-84860181606&partnerID=40&md5=e2d23910c45bd2d492d8f26f4c0f6a97.

Elman, Z. & Muravin, B., 2011. Acoustic Emission Apparatus and Data Aquisition. Available at: http://www.slideshare.net/mboria/acoustic-emission-sensors-equipment [Accessed June 11, 2015].

Experimental Aircraft Info, 2015. Aluminum Alloys In Aviation. Available at: http://www.experimentalaircraft.info/articles/aircraft-aluminum.php [Accessed September 11, 2015].

Federal Aviation Administration, 2008. *Aviation Maintenance Technician Handbook - General*, Washington: U.S. Government Printing Office.

Federal Aviation Administration, 2012. *Aviation Maintenance Technician Handbook—Airframe*.

Ferrari, V. & Lucklum, R., 2008. Overview of Acoustic-Wave Microsensors. In *Piezoelectric Transducers and Applications*. p. 42.

Findlay, S.J. & Harrison, N.D., 2002. Why aircraft fail. *Materials Today*, 5(11), pp.18–25. Available at: http://dx.doi.org/10.1016/S1369-7021(02)01138-0.

Finlayson, R.D. et al., 2001. Health monitoring of aerospace structures with acoustic emission and acousto-ultrasonics. *Insight*, 43(3), pp.155–158. Available at: http://www.pacndt.com/downloads/Insight AEHums.pdf.

Fleck, N.A., 1997. Compressive Failure of Fibre Composites. *Advances in Applied Mechanics*, 33.

Fokker Aerostructures, 2015. Along the bond line: Groundbreaking aircraft structures. Available at: http://www.fokker.com/sites/default/files/media/Files/Brochures/Fokker_Glare.pdf [Accessed April 16, 2015].

Gallego, A. et al., 2014. Real-time time Algorithm to Classify AE Events of Lamb Waves in CFRP. In *31st Conference of the European Working Group on Acoustic Emission*.

Gorman, M.R. & Prosser, W.H., 1991. AE Source Orientation by Plate Wave Analysis. *Journal of Acoustic Emission*, 9(4), pp.283–288.

Gorman, M.R. & Ziola, S.M., 1991. Plate waves produced by transverse matrix cracking. *Ultrasonics*, 29(3), pp.245–251. Available at: http://www.scopus.com/inward/record.url?eid=2-s2.0-0026152889&partnerID=40&md5=ecca25b69fcb6c53e691078665058a30.

Grédiac, M., 2004. The use of full-field measurement methods in composite material characterization: Interest and limitations. *Composites Part A: Applied Science and Manufacturing*, 35(7-8), pp.751–761.

Grosse, C., 2002. Kaiser effect. Available at: http://www.ndt.net/ndtaz/content.php?id=476 [Accessed May 14, 2015].

Gudmundsson, S., 2014. *General Aviation Aircraft Design* First., Oxford, UK: Elsevier Ltd.

Gutkin, R. et al., 2011. On acoustic emission for failure investigation in CFRP: Pattern recognition and peak frequency analyses. *Mechanical Systems and Signal Processing*, 25(4), pp.1393–1407. Available at: http://dx.doi.org/10.1016/j.ymssp.2010.11.014.

Hagenbeek, M., 2005. *Characterisation of Fibre Metal Laminates under Thermo-mechanical Loadings*. Delft University.

Hale, J., 2008. *Boeing 787 From the Ground Up*.

Hamstad, M.A., O'Gallagher, A. & Gary, J., 2002. A WAVELET TRANSFORM APPLIED TO ACOUSTIC EMISSION SIGNALS: PART 1: SOURCE IDENTIFICATION. *Journal of Acoustic Emission*, 20. Available at: http://www.ndt.net/article/jae/papers/20-039.pdf.

Hansson, P. & Melin, S., 2004. Dislocation Modelling of Short Fatigue Crack Growth Through Alternating Slip. In *The 15th European Conference of Fracture*. Stockholm.

Harris, B., 2003. *Fatigue in Composites: Science and Technology of the Fatigue Response of Fibre-reinforced Plastics*, CRC Press.

Hasiotis, T., Badogiannis, E. & Tsouvalis, N.G., 2011. Application of ultrasonic C-scan techniques for tracing defects in laminated composite materials. *Strojniski Vestnik/Journal of Mechanical Engineering*, 57(3), pp.192–203.

Hellier, C.J., 2001. Chapter 10: Acoustic Emission Testing. In McGraw-Hill, ed. *Handbook of Nondestructive Evaluation*.

Herbst, C. & Splitthof, K., 2013. *Q-400*, Dantec Dynamics Technical Note.

Hintona, M.J. & Soden, P.D., 1998. Predicting Failure in Composite Laminates: The Background to the Exercise. *Composites Science and Technology*, 58.

Hirschel, E.H., Prem, H. & Madelung, G., 2004. *Aeronautical Research in Germany: From Lilienthal until Today* First Edit., Springer.

Hitchens, F., 2015. *Propeller Aerodynamics: The History, Aerodynamics & Operation of Aircraft Propellers*, Andrews UK Ltd.

Hocheng, H. & Tsao, C., 2007. Computerized Tomography and C-Scan for Measuring Drilling-Induced Delamination in Composite Material Using Twist Drill and Core Drill. *Key Engineering Materials*, 339, pp.16–20.

Holford, K. Eaton, M., Clarke, A., Pearson, M., Featherston, C., Pullin, R., 2013. Approaches to Acoustic Amission Monitoring With Applicability to Key Components in Wind Turbines. In *9th International Workshop on Structural Health Monitoring*.

Holford, K.M., Pullin, R., Evans, S. L., Eaton, M., Hensman, J., Worden, K., 2009. Acoustic emission for monitoring aircraft structures. In *Proceedings of the Institution of Mechanical Engineers, Part G: Journal of Aerospace Engineering 2009*. Available at: http://orca.cf.ac.uk/5429/.

Hsu, N.N. & Breckenridge, F.R., 1981. CHARACTERIZATION AND CALIBRATION OF ACOUSTIC EMISSION SENSORS. *Materials Evaluation*, 39(1), pp.60–68. Available at: http://www.scopus.com/inward/record.url?eid=2-s2.0-0019437172&partnerID=40&md5=0dea83106463e0a04fc499a0194e90d5.

IATA, 2013a. *2013 Annual Review*.

IATA, 2015. *FACT SHEET : CLIMATE CHANGE*.

IATA, 2013b. *Technology Roadmap*.

ICAO, 2010. *Environmental Report 2010*.

ICAO, 2013. *Environmental Report 2013*.

Industrial Talks, 2012. Why Titanium Is Used in the Aircraft Industry. Available at: https://industrialtalks.wordpress.com/2012/12/12/why-titanium-is-used-in-the-aircraft-industry/ [Accessed September 12, 2015].

IPCC, 2007. *Climate Change 2007 : Synthesis Report*, Available at: http://www.ipcc.ch/pdf/assessment-report/ar4/syr/ar4_syr.pdf.

IPCC, 2015. *Climate Change 2014 Synthesis Report*.

IPCC, 2014. *Climate Change 2014, Mitigation of Climate Change* O. Edenhofer, R. Pichs-Madruga, & Y. Sokona, eds., New York: Cambridge University Press. Available at: http://report.mitigation2014.org/spm/ipcc_wg3_ar5_summary-for-policymakers_approved.pdf.

Irwin, G.R., Paris, P.C. & Tada, H., 2000. *The Stress Analysis of Cracks Handbook* Third, ed., American Society of Mechanical Engineers.

Jakab, P.L., 1999. Wood to Metal: The Structural Origins of the Modern Airplane. *Journal of Aircraft*, 36(6), pp.914–918.

Jeong, H., 2001. Analysis of plate wave propagation in anisotropic laminates using a wavelet transform. *NDT and E International*, 34(3), pp.185–190. Available at: http://www.scopus.com/inward/record.url?eid=2-s2.0-0035313607&partnerID=40&md5=dbde6f240316f39c2ae0ddea2ae1e4cc.

Jones, R.M., 1999. *Mechanics Of Composite Materials* Second., Taylor & Francis.

Jong, H.-J., 2006. Transverse cracking in a cross-ply composite laminate - Detection in acoustic emission and source characterization. *Journal of Composite Materials*, 40(1), pp.37–69. Available at: http://www.scopus.com/inward/record.url?eid=2-s2.0-31044455094&partnerID=40&md5=70cfe655e02751b2e7ec15a406ff0242.

Kapadia, A., 2007. *Non-Destructive Testing of Composite Materials*, Available at: https://compositesuk.co.uk/system/files/documents/ndtofcomposites.pdf.

Kotsikos, G. et al., 1999. Use of acoustic emission to characterize corrosion fatigue damage accumulation in glass fiber reinforced polyester laminates. *Polymer Composites*, 20(5), pp.689–696.

Kurz, J.H., Grosse, C.U. & Reinhardt, H.W., 2005. Strategies for reliable automatic onset time picking of acoustic emissions and of ultrasound signals in concrete. *Ultrasonics*, 43(7), pp.538–546. Available at: http://www.scopus.com/inward/record.url?eid=2-s2.0-20144383158&partnerID=40&md5=de1d5db1ea3aa966b5c0aab4c762838c.

Kwon, H.J. Rogalsky, D., Kovalchick, C., Ravichandran, G., 2013. Application of digital image correlation method to Solid Mechanics. In *12th National Congress on Theoretical and Applied Mechanics*. Varna, Bulgaria.

Lee, J. & Soutis, C., 2007. A study on the compressive strength of thick carbon fibre-epoxy laminates. *Composites Science and Technology*, 67(10), pp.2015–2026.

Lopresto, 2009. Analysis of acoustic emission signals produced by different carbon fibre reinforced plastic. *Proceedings of 17th international conference on composites (ICCM).*

Maeda, N., 1985. A Method for Reading and Checking Phase Times in Auto-Processing System of Seismic Wave Data. *Zisin = Jishin*, 38(3), pp.pp. 365–379.

Malegori, G. & Ferrini, G., 2010. Tip-sample interactions on graphite studied using the wavelet transform. *Beilstein Journal of Nanotechnology*, 1, pp.pp. 172–181. Available at: http://www.beilstein-journals.org/bjnano/single/articleFullText.htm?publicId=2190-4286-1-21.

Man, J., Obrtlík, K. & Polák, J., 2009. Extrusions and intrusions in fatigued metals . Part 1. State of the art and history. *Philosophical Magazine*, 89(16), pp.pp. 1295–1336.

Marat-Mendes, R. & Freitas, M., 2011. Non Destructive Evaluation of Damage In Glassfibre Composites Using C-scanning Analysis. In A. J. M. Ferreira, ed. *16th International Conference on Composite Structures*. Porto.

Martínez-Jequier, J. Gallego, A., Suárez, E., Juanes, F. J., Valea, Á., 2015. Real-time damage mechanisms assessment in CFRP samples via acoustic emission Lamb wave modal analysis. *Composites Part B: Engineering*, 68, pp.317–326. Available at: http://linkinghub.elsevier.com/retrieve/pii/S1359836814003941.

Mascaro, B. Gibiat, V., Bernadou, M., Esquerre, Y., 2005. Acoustic Emission of the drilling of Carbon / Epoxy composites Experimental results HSS drill and HSS mill results. In *Forum Acusticum*. pp. 2823–2827.

McCrory, J.P. Al-jumaili, S. Kh., Crivelli, D., Pearson, M. R., Eaton, M. J., Featherston, C., Guagliano, M., Holford, K. M., Pullin, R., 2015. Damage classification in carbon fibre composites using acoustic emission : A comparison of three techniques. *Composites Part B*, 68(JANUARY), pp.424–430. Available at: http://dx.doi.org/10.1016/j.compositesb.2014.08.046.

Mehan, R.L. & Mullin, J. V, 1971. Analysis of composite failure mechanisms using acoustic emissions. *Journal of Composite Materials*, 5, pp.266–269. Available at: http://www.scopus.com/inward/record.url?eid=2-s2.0-0015050984&partnerID=40&md5=b45d1973259034b3066cc82495d1e6f6.

Miller, R.K., Findlay, R.D. & Carlos, M.F.., 2005. Acoustic Emission Testing. In E. V. K. H. and P. O. M. R. K. Miller, ed. *NDT handbook*. Columbus, pp. 122–146.

MISTRAS, 2013. F50α Sensor, Product Data Sheet.

MISTRAS, 2009. PCI-2 Product Bulletin. Available at: http://www.physicalacoustics.com/content/literature/multichannel_systems/PCI-2_Product_Bulletin.pdf [Accessed May 2, 2015].

MISTRAS, 2011a. R30S Sensor - Product Data Sheet. Available at: http://www.physicalacoustics.com/content/literature/sensors/Model_R30S.pdf.

MISTRAS, 2011b. *WD Sensor Product Data Sheet.*

De Moura, M.F.S., Gonçalves, J.P.M., Marques, A.T., de Castro, P.M.S.T., 2000. Prediction of compressive strength of carbon–epoxy laminates containing delamination by using a mixed-mode damage model. *Composite Structures*, 50(2), pp.151–157. Available at: http://linkinghub.elsevier.com/retrieve/pii/S026382230000091X.

Mraz, S., 2014. Basics of Aerospace Materials: Aluminum and Composites. *Machine Design*. Available at: http://machinedesign.com/materials/basics-aerospace-materials-aluminum-and-composites [Accessed September 10, 2015].

Muravin, B., 2009. Acoustic Emission Wave Propagation and Source Location. , p.Slide 8. Available at: http://www.slideshare.net/mboria/muravin-acoustic-emission-wave-propagation-and-source-location.

Nairn, J. a, 2000. Matrix Microcracking in Composites. *Comprehensive Composite Materials*, 2, pp.1–34.

NDT Resource Centre, Acoustic Emission Equipment. Available at: https://www.nde-ed.org/EducationResources/CommunityCollege/Other Methods/AE/AE_Equipment.php.

NDT Resource Centre, 2013. Fatigue Properties. Available at: https://www.nde-ed.org/EducationResources/CommunityCollege/Materials/Mechanical/Fatigue.htm [Accessed May 5, 2015].

Nesvijski, E. & Marasteanu, M., 2007. Wavelet Transform and Its Applications to Acoustic Emission Analysis of Asphalt Cold Cracking. *NDT.net*. Available at: http://www.ndt.net/search/docs.php3?id=4513 [Accessed March 29, 2016].

Nielson, A., 1980. *Acoustic Emission Source Based on Pencil Lead Breaking,* Danish Welding Institute.

Nivesrangsan, P., Steel, J. a. & Reuben, R.L., 2007. Source location of acoustic emission in diesel engines. *Mechanical Systems and Signal Processing*, 21(2), pp.1103–1114. Available at: http://linkinghub.elsevier.com/retrieve/pii/S0888327006000045.

De Oliveira, R. & Marques, A.T., 2008. Health monitoring of FRP using acoustic emission and artificial neural networks. *Computers and Structures*, 86(3-5), pp.367–373.

Ono, K., Jeng, J.S. & Yang, J.M., 1989. Fracture mechanism studies of a carbon fiber-peek composite by acoustic emission. In *Symposium on Acoustic Emission: Current Pratice and Future Directions*. ASTM, pp. 395–403.

Paris, P.C., Gomez, M.P. & Anderson, W.E., 1961. A rational analytic theory of fatigue. *The Trend in Engineering*, 13, pp.9–14.

Pearson, M.R., 2013. *Development of Lightweight Structural Health Monitoring Systems for Aerospace Applications*. Cardiff University.

Physical Acoustics Corporation, 2004. AEWin Software Users Manual. , p.Appendix 1.

Physical Acoustics Corporation, 2003. PCI-2 – PCI-BASED TWO-CHANNEL AE BOARD & SYSTEM. Available at: http://www.physicalacoustics.com/by-product/pci-2/ [Accessed May 2, 2015].

Polák, J., 2013. Persistent Slip Bands (PSBs). *Encyclopedia of Tribology*, pp.pp. 2510–2513.

Pollock, A.A., 1986. Classical Plate Theory in Practical AE Testing. In *Eighth International Acoustic Emission Symposium*. The Japanese Society for Nondestructive Testing, pp. 708–721.

Prosser, W.H., 1996. Advanced AE Techniques in Composite Materials Research. *Journal of Acoustic Emission*, 14(3-4), pp.S1–S11.

Prosser, W.H. & Madaras, E.I., 2011. *Development and Certification of Ultrasonic Background Noise Test (UBNT) System for use on the International Space Station (ISS)*, Available at: http://hdl.handle.net/2060/20110014267.

Pullin, R. Pearson, M.R., Eaton, M.J., Featherston, C.A., Holford, K.M., Clarke, A., 2013. Automated Damage Detection in Composite Components Using Acoustic Emission. *Key Engineering Materials*, 569-570, pp.80–87.

Pullin, R. Eaton, M.J., Hensman, J. J., Holford, K.M., Worden, K., Evans, S.Lewin., 2010. Validation of acoustic emission (AE) crack detection in aerospace grade steels using Digital Image Correlation (DIC). *Applied Mechanics and Materials*, 24-25, pp.pp. 221–226.

Pullin, R., Holford, K.M. & Baxter, M.G., 2005. Modal analysis of acoustic emission signals from artificial and fatigue crack sources in aerospace grade steel. In *Key Engineering Materials*. pp. 217–224. Available at: http://www.scopus.com/inward/record.url?eid=2-s2.0-33845936168&partnerID=tZOtx3y1.

Ramadan, K.S., Sameoto, D. & Evoy, S., 2014. A review of piezoelectric polymers as functional materials for electromechanical transducers. *Smart Materials and Structures*, 23(3). Available at: http://stacks.iop.org/0964-1726/23/i=3/a=033001?key=crossref.99caa5f3fa79d7c3462313d26f05a5a5.

Rindorf, H.J., 1981. Acoustic Emission Source Location in Theory and in Practice. In *Acoustic Emission Source Location*.

Ritchie, R.O., 1999. Mechanisms of fatigue-crack propagation in ductile and brittle solids. *International Journal of Fracture*, 100, pp.58–83.

Roach, D., 2007. Smart Aircraft Structures: a Future Necessity. *High Performance Composites*. Available at: http://www.compositesworld.com/articles/smart-aircraft-structures-a-future-necessity.

Roeseler, W.G., Sarh, B. & Kismarton, M.U., 2007. Composite Structures: The First 100 Years. In *16th International Conference on Composite Materials*.

Rolfe, S.T. & Barsom, J.M., 1977. *Fracture and Fatigue Conrol in Structures*, Prentice-Hall Inc.

Russell, D.A., 2011. Waves in a Dispersive Medium. Available at: http://www.acs.psu.edu/drussell/Demos/Dispersion/dispersion.html [Accessed June 9, 2015].

Sadeghi, G., Hosseini-Toudeshky, H. & Mohammadi, B., 2014. An investigation of matrix cracking damage evolution in composite laminates – Development of an advanced

numerical tool. *Composite Structures*, 108, pp.937–950. Available at: http://linkinghub.elsevier.com/retrieve/pii/S0263822313005205.

Sause, M.G.R. Gribov, A., Unwin, A. R., Horn, S., 2012. Pattern recognition approach to identify natural clusters of acoustic emission signals. *Pattern Recognition Letters*, 33(1), pp.17–23.

Sause, M.G.R. Müller, T., Horoschenkoff, A., Horn, S., 2012. Quantification of failure mechanisms in mode-I loading of fiber reinforced plastics utilizing acoustic emission analysis. *Composites Science and Technology*, 72(2), pp.167–174. Available at: http://www.scopus.com/inward/record.url?eid=2-s2.0-84855852662&partnerID=40&md5=f10c0e4925bc2a60ef6b36d472a59142.

Schmidt, H.-J. Schmidt-Brandecker, B., Tober, G., Aktiengesellschaft, D-B., 1998. Design of modern aircraft structure and the role of NDI. In *Proceedinge of the 7th European Conference on Non-Destructive Testing*. Copenhagen. Available at: http://www.ndt.net/article/ecndt98/aero/001/001.htm.

Scholey, J.J. Wisnom, M R., Friswell, M. I., Pavier, M., Aliha, M. R., Wilcox, P D., 2009. A Generic Technique for Acoustic Emission Source Location. *Journal of Acoustic Emission*, 27, pp.291–298.

Schreier, H., Orteu, J.-J. & Sutton, M.A., 2009. *Image correlation for shape, motion and deformation measurements: Basic concepts, theory and applications*, Available at: http://www.scopus.com/inward/record.url?eid=2-s2.0-84892194308&partnerID=40&md5=a7ed11ae2d27bdc02186514cff037265.

Sedlak, P. Hirose, Y., Khan, S A., Enoki, M., Sikula, J., 2008. New automatic localization technique of acoustic emission signals in thin metal plates. *Ultrasonics*, 49(2), pp.254–262. Available at: http://www.scopus.com/inward/record.url?eid=2-s2.0-56949087993&partnerID=40&md5=8ab1549f8336661a65af62dd459fde04.

Seyed Yaghoubi, A., Liu, Y. & Liaw, B., 2012. Stacking sequence and geometrical effects on low-velocity impact behaviors of GLARE 5 (3/2) fiber-metal laminates. *Journal of Thermoplastic Composite Materials*, 25(2), pp.223–247. Available at: http://www.scopus.com/inward/record.url?eid=2-s2.0-84857348241&partnerID=40&md5=e52dbe62e1e7c084d716320674dc4c4d.

Shyr, T.-W. & Pan, Y.-H., 2003. Impact resistance and damage characteristics of composite laminates. *Composite Structures*, 62(2), pp.193–203. Available at: http://linkinghub.elsevier.com/retrieve/pii/S0263822303001144.

De Silva, C., 2007. *Vibration Monitoring, Testing, and Instrumentation*, Boca Raton: CRC Press.

Sinke, J., 2003. Manufacturing of GLARE Parts and Structures. *Applied Composite Materials*, 10(4-5), pp.293–305. Available at: http://dx.doi.org/10.1023/A%3A1025589230710.

Sinke, J., 2009. Manufacturing Principles for Fiber Metal Laminates. In *International Conference on Composite Materials*.

Sinmazçelik, T., Avcu, E., Bora, M.Ö., Çoban, O., 2011. A review: Fibre metal laminates, background, bonding types and applied test methods. *Materials & Design*, 32(7), pp.3671–3685. Available at: http://linkinghub.elsevier.com/retrieve/pii/S0261306911001671.

Soutis, C., 1995. *Compressive Behaviour of Composites* R. Dolbey, ed., Rapra Technology Limited.

Srinivasa, V. Shivakumar, V., Nayaka, V., Jagadeeshaiaih, S., Seethram, M., Shenoy, R., Nafidi, A., 2010. Fracture morphology of carbon fiber reinforced plastic composite laminates. *Materials Research*, 13(3).

Stephens, R.W.B. & Pollock, A.A., 1971. Waveforms and Frequency Spectra of Acoustic Emissions. *The Journal of the Acoustical Society of America*, 50(3B), p.904.

Suresh, S., 2003. *Fatigue of Materials*, Cambridge: Cambridge University Press.

Surgeon, M. & Wevers, M., 1999. Modal analysis of acoustic emission signals from CFRP laminates. *NDT and E International*, 32(6), pp.311–322. Available at: http://www.scopus.com/inward/record.url?eid=2-s2.0-0033308297&partnerID=40&md5=1db7da13c86a8fde0413d15167152057.

The U.S. Council of Economic Advisers, 2014. *THE COST OF DELAYING ACTION TO STEM CLIMATE CHANGE*,

Theobald, P., 2012. Guide on Acoustic Emission Sensor Couplants. Available at: http://www.npl.co.uk/acoustics/ultrasonics/research/guide-on-acoustic-emission-sensor-couplants [Accessed May 12, 2015].

Tilley, R.J.D., 2004. *Understanding Solids: The Science of Materials*, Chichester: Wiley.

Torenbeek, E., 2013. *Advanced Aircraft Design: Conceptual Design, Analysis and Optimization or Subsonic Civil Airplanes*, Wiley.

Totten, G., 2008. Fatigue Crack Propagation. *Advanced Materials & Processes*, p.pp. 39.

Toyama, N., Kikushima, Y. & Takatsubo, J., 2002. Effect of delamination on lamb wave velocity in cross-ply laminates. *Journal of Materials Science Letters*, 21(24), pp.1891–1893. Available at: http://www.scopus.com/inward/record.url?eid=2-s2.0-0037116301&partnerID=40&md5=6820f32cf516bfe0276b502fd1b7fcef.

Valentin, D., Bonniau, P. & Bunsell, A.R., 1983. Failure mechanism discrimination in carbon fibre-reinforced epoxy composites. *Composites*, 14(4), pp.345–351. Available at: http://www.scopus.com/inward/record.url?eid=2-s2.0-0020833420&partnerID=40&md5=6759cf44faa90bd8879e98ed3616b0ec.

Vallen, H., 2002. AE Testing Fundamentals, Equipment, Applications. *The e-Journal of Nondestructive Testing*, 7(9).

Vallen Systems, 2012. *Acoustic Emission Sensors - Specification*,

Vishay Precision Group, 2015. Introduction to Photoelasticity. Available at: http://www.vishaypg.com/micro-measurements/photo-stress-plus/category/introduction/?subCategory=introduction [Accessed April 11, 2015].

W. H. Prosser S. Kellas, B. T. Smith, J. McKeon, and A. Friedm, K.E.J., 1995. Advanced, Waveform Based Acoustic Emission Detection of Matrix Cracking in Composites. *Materials Evaluation*, 53(9), pp.1052–1058.

Wang, W. Mottershead, J. E., Siebert, T., Pipino, A., 2012. Full-field modal identification using image moment descriptors. In *International Conference on Noise and Vibration Engineering 2012, ISMA 2012, including USD 2012: International Conference on Uncertainty in Structure Dynamics*. pp. 2133–2143. Available at: http://www.scopus.com/inward/record.url?eid=2-s2.0-84906334584&partnerID=40&md5=8e4a56f4ed74ea209facfc25cd014c1f.

Wood, W.A., 1958. Formation of Fatigue Cracks. *Philosophical Magazine*, pp.pp. 692–699.

Yashiro, S. & Ogi, K., 2009. Fracture behavior in CFRP cross-ply laminates with initially cut fibers. *Composites: Part A*, 40, pp.938–947.

Yoneyama, S. & Murasawa, G., 2008. Digital Image Correlation. *Encyclopedia of Life Support Systems (EOLSS)*.

Ziola, S.M. & Gorman, M.R., 1991. Source location in thin plates using cross-correlation. *Journal of the Acoustical Society of America*, 90(5), pp.2551–2556. Available at: http://www.scopus.com/inward/record.url?eid=2-s2.0-0025718664&partnerID=40&md5=6c413a94df0bef62b594b1228084f03d.

Zohari, M.H., Epaarachchi, J.A. & Lau, K.T., 2013. Modal Acoustic Emission investigation for progressive failure monitoring in thin composite plates under tensile test. *Key Engineering Materials*, 558, pp.65–75. Available at: http://www.scopus.com/inward/record.url?eid=2-s2.0-84880422871&partnerID=40&md5=89b85376705566dabee65308e039aed7.

# 9 Appendices

## 9.1 Appendix A – AE Sensor Manufacturer's Product Data Sheets

MISTRAS
A World of NDT Solutions | Products & Systems Division

PHYSICAL ACOUSTICS CORPORATION

PRODUCT DATA SHEET

### Nano30 Sensor

Medium Frequency Resonant Miniature Sensor

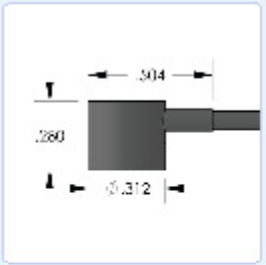


#### DESCRIPTION AND FEATURES

The Nano-30 miniature AE sensor has a resonant response at 300Khz and a good frequency response over the range of 125 – 750 kHz. Its size makes the sensor an ideal candidate for applications where small size is important. The sensor features a small, 1 meter, integral coax cable, which exits from the side of the sensor with a BNC connector on the end.

#### APPLICATIONS

The sensor can be used in any application requiring a small, mid-band frequency response. It can easily be mounted using epoxy and can be mounted in small and tight spaces.

#### OPERATING SPECIFICATIONS

*Dynamic*

| | |
|---|---|
| Peak Sensitivity, Ref V/(m/s) | 62 dB |
| Peak Sensitivity, Ref V/µbar | -72 dB |
| Operating Frequency Range | 125-750 KHz |
| Resonant Frequency, Ref V/(m/s) | 140 KHz |
| Resonant Frequency, Ref V/µbar | 300 KHz |
| Directionality | +/- 1.5 dB |

*Environmental*

| | |
|---|---|
| Temperature Range | -65 to 177ºC |
| Shock Limit | 500 g |
| Completely enclosed crystal for RFI/EMI immunity | |

*Physical*

| | |
|---|---|
| Dimensions | 0.3"OD X 0.3"H |
| | 8 mm OD X 8 mm H |
| Weight | 2 grams (8 with cable & connector) |
| Case Material | Stainless steel |
| Face Material | Ceramic |
| Connector | BNC |
| Connector Locations | Side |

#### ORDERING INFORMATION AND ACCESSORIES

| | |
|---|---|
| Nano30 | Nano30 |
| Cable (specify cable length in meters) | 1 m |
| Preamplifier | 0/2/4, 2/4/6 |
| Amplifier Subsystems | AE2A, AE5A |
| Preamp to System Cable (specify length in 'm') | 1234-X |

*Sensors include*

NIST Calibration Certificate & Warranty

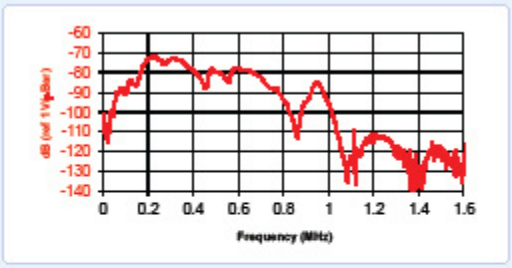



WORLDWIDE HEADQUARTERS:
195 Clarksville Rd •
Princeton Jct, NJ 08550 • USA
T: +1.609.716.4000 • F: +1.609.716.0706
E-MAIL: sales.systems@mistrasgroup.com

| | | | | | |
|---|---|---|---|---|---|
| CANADA | T: +1.403.556.1350 | HOLLAND | T: +31.010.245.0325 | RUSSIA | T: +7495.789.4549 |
| CHINA | T: +86.10.5877.3631 | INDIA | T: +91.22.2586.2444 | SCANDINAVIA | T: +46(0)31.252040 |
| FRANCE | T: +331.498.26040 | JAPAN | T: +81.33.498.3570 | S. AMERICA | T: +55.11.3082.5111 |
| GERMANY | T: +49.040 2000.4025 | MALAYSIA | T: +60.9.517.3788 | UK | T: +44(0)1954.231.612 |
| GREECE | T: +30.210.2846.801-4 | MIDDLE EAST | T: +973.17.729.356 | | |


 #2100-11-157-01 www.mistrasgroup.com

MISTRAS
A World of NDT Solutions | Products & Systems Division

PHYSICAL ACOUSTICS CORPORATION

PRODUCT DATA SHEET

# WD Sensor

## Wideband Differential Sensor

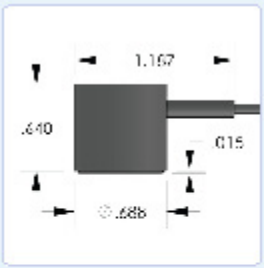


### DESCRIPTION AND FEATURES

WD is a true differential wideband sensor with a very high sensitivity and bandwidth. It has a very good frequency response over the range of 100 – 900 kHz. Differential sensors differ from their general purpose counterparts by employing two sensing elements with opposite polarization directions. The two signal leads feed into a differential pre-amplifier which eliminates common-mode noise resulting in a lower noise output from the pre-amplifier. Noise improvements to the tune of 2 dB can be achieved using differential sensors over a single ended sensor. This sensor features a rugged steel construction with an integrated twin axial cable exiting on the side.

### APPLICATIONS

This sensor is well suited for structural health monitoring of large structures like storage tanks, pipelines etc. This sensor is an ideal candidate for applications requiring high bandwidth for frequency analysis of the AE signals for noise discrimination and source identification. Wideband sensors are particularly well suited for research applications where a high fidelity AE response is required. It can be easily mounted using epoxy.

### OPERATING SPECIFICATIONS

*Dynamic*

| | |
|---|---|
| Peak Sensitivity, Ref V/(m/s) | 56 dB |
| Peak Sensitivity, Ref V/µbar | -61 dB |
| Operating Frequency Range | 125-1000 kHz |
| Resonant Frequency, Ref V/(m/s) | 125 kHz |
| Resonant Frequency, Ref V/µbar | 450 kHz |
| Directionality | +/-1.5 dB |

*Environmental*

| | |
|---|---|
| Temperature Range | -65 to 177°C |
| Shock Limit | 500 g |
| Completely enclosed crystal for RFI/EMI immunity | |

*Physical*

| | |
|---|---|
| Dimensions | 0.7"OD X 0.65"H<br>17.8 mm OD X 16.5 mm H |
| Weight | 20 grams |
| Case Material | Stainless Steel |
| Face Material | Ceramic |
| Connector | BNC |
| Connector Locations | Side |

### ORDERING INFORMATION AND ACCESSORIES

| | |
|---|---|
| WD | WD |
| Cable (specify length in "-XX" m at end of PN) | 1 m |
| Magnetic Hold-Down | MHSTD |
| Pre-Amplifier | 0/2/4, 2/4/6 |
| Preamp to System Cable (specify length in 'm') | 1234-X |
| Amplifier Subsystems | AE2A or AE5A |

*Sensors include*

NIST Calibration Certificate & Warranty

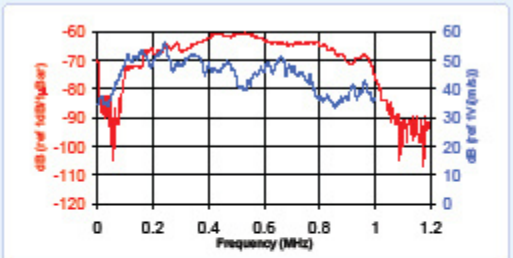



**WORLDWIDE HEADQUARTERS:**
195 Clarksville Rd •
Princeton Jct, NJ 08550 • USA
T: +1.609.716.4000 • F: +1.609.716.0706
E-MAIL: sales.systems@mistrasgroup.com

| | | | | | |
|---|---|---|---|---|---|
| CANADA | T: +1.403.556.1350 | HOLLAND | T: +31.010.245.0325 | RUSSIA | T: +7495.789.4549 |
| CHINA | T: +86.10.5877.3631 | INDIA | T: +91.22.2586.2444 | SCANDINAVIA | T: +46(0)31.252040 |
| FRANCE | T: +331.498.26040 | JAPAN | T: +81.33.498.3570 | S. AMERICA | T: +55.11.3082.5111 |
| GERMANY | T: +49.040 2000.4025 | MALAYSIA | T: +60.9.517.3788 | UK | T: +44(0)1954.231.612 |
| GREECE | T: +30.210.2846.801-4 | MIDDLE EAST | T: +973.17.729.356 | | |


 #2100-11-133-01

www.mistrasgroup.com